2016

Lifetime performance prediction of reinforced concrete structures in multi-threat areas

Zhen Cui
Iowa State University

Lifetime performance prediction of reinforced concrete structures in multi-threat areas

by

Zhen Cui

A dissertation submitted to the graduate faculty

in partial fulfillment of the requirements for the degree of

DOCTOR OF PHILOSOPHY

Major: Civil Engineering (Structural Engineering)

Program of Study Committee:
Azadeh Alipour, Major Professor
Behrouz Shafei-Pamsari
An Chen
Kejin Wang
Ming-Chen Hsu

Iowa State University
Ames, Iowa

2017

DEDICATION

This disseration is dedicated to those who love me and light my life, those who guide me and encourage me and those who become the meaning of my life. For those who are part of my life but might no longer be able to shed light on hope for me, this is my gift of love.

TABLE OF CONTENTS

LIST OF FIGURES

LIST OF TABLES

ACKNOWLEDGEMENTS

I would like to thank my major professor, Dr. Azadeh Alipour, for the guidance throughout my research and the insightful comments in the development of this dissertation. I would also like to express my thanks to my committee members, Dr. Behrouz Shafei-Pamsari, Dr. An Chen, Dr. Kejin Wang, and Dr. Ming-Chen Hsu for their advice and help. Finally, I would like to thank my family and friends for the emotional support throughout my graduate studies.

ABSTRACT

Reinforced concrete (RC) structures are usually subjected to various natural hazards and environmental stressors during their lifetime. Over the time, structures are continuously aging and rapidly deteriorating in their lifecycle, becoming increasingly vulnerable to catastrophic failures after natural or manmade hazards. Corrosion of steel reinforcement has been identified as one of the major causes of deterioration in reinforced concrete structures. Chloride ingress is the dominant mechanism for initiation of deterioration in coastal regions or areas with high exposure to deicing salts. The chloride-induced crack initiation stage in deterioration process, which defines the end of functional service life for corroded RC structures has been investigated in this study. Crack initiation is governed by the expansion of corrosion products. It was found that crack initiation time is significantly affected by rate of corrosion, thickness of interfacial transmission zone (ITZ), composition of corrosion products, and mechanism of corrosion. Other factors which can also influence crack initiation time are the structure's geometrical parameters such as concrete cover depth, rebar diameter and spacing, and concrete tensile strength. Different reinforced concrete structural components have been simulated using nonlinear 3-D finite element (FE) models in order to study their lifetime performance under corrosion. The developed FE models are validated with the available experimental tests. All of the corrosion effects on structural behavior of RC structures, such as reduction of steel cross sectional area, change of steel and concrete properties, as well as deterioration of bond have been implemented into the 3-D FE models. The structural performance of corroded RC beams is obtained through FE analysis. The results show that corrosion influences the strength and ductility of a structure at ultimate condition, and may also cause excessive cracking and deflection, which leads to serviceability failure.

Moreover, a large number of RC structures that suffer from corrosion mechanisms are located in high seismic risk areas, which leads to the necessity of investigating the combined effects of corrosion and earthquake in order to provide a more reliable prediction for the lifetime performance of RC structures in both corrosive and high seismic risk areas. Therefore, a comprehensive FE framework has been developed to study the structural response of RC columns under earthquake hazards while they are constantly exposed to chloride attack. This framework is capable of including all of the degrading effects due to chloride-induced corrosion and has been validated by a previous set of experimental test results. The extent of structural degradation has been updated as a function of time. Equivalent static analysis and nonlinear time history analysis have been conducted to evaluate the seismic performance of corroded columns at multiple time periods as well as under various hazard levels. The region, type and extent of damage have been identified. Full details of hysteretic loops, frequency variation, and cover crack propagation patterns have been obtained from the FE analysis. Furthermore, this study has also considered multiple seismic events occurring during the lifetime of RC structures. Detailed FE models that are able to transfer residual damage from previous earthquake to the next earthquake have been proposed. The extent of damage after each earthquake has been quantified. The result of this study shows that the corrosion can dramatically reduce the strength and stiffness of the column. Under severe earthquake, extensive corrosion may result in a brittle failure of the column without the development of concrete cracks. When a critical section of the column experiences a much higher corrosion risk, the seismic performance can be greatly compromised. Such columns could perform much worse than a column undergoing a consistent corrosion rate at a much older age, thus engineers must be alerted to draw special attention to those columns to prevent catastrophic failure during

seismic events. The outcome of this research will provide more reliable predictions for the lifetime performance of RC structures, thus help engineers and inspectors improve their designs, identify necessary test regions and define comprehensive inspection plans, while optimizing the rehabilitation strategies for RC structures under multi-threat areas.

CHAPTER 1. INTRODUCTION AND MOTIVATION

Civil infrastructure systems such as highway transportation networks are tied up, directly or indirectly, with every country's economy in a major way. The state of nation's civil infrastructure has also significant impacts on the safety and quality of living. Among various infrastructure components, the highway bridges play a key role in a transportation network and huge money is spent every year to ensure their functionality. Over the time, highway bridges are aging, rapidly deteriorating, and becoming increasingly vulnerable to the catastrophic failure during probable natural or man-made hazards. The deterioration of infrastructure has been of great concern in the United States in recent years. According to the ASCE Report Card for America's infrastructure (2013), one out of four bridges in the U.S. are categorized as "structurally deficient" or "functionally obsolete" requiring significant cost in maintenance, rehabilitation and replacement. According to the National Bridge Inventory data (2011), there are more than 600,000 bridges in U.S. The most common material used in bridges is reinforced concrete (RC) forming 41.6% of the bridge population. The second most common type is steel bridges with 30.4% and prestressed concrete bridges rank third with 23.6%. It is evident that more than half of the bridges constructed in the U.S. are concrete bridges with an increasing trend over the next decade. On the other hand, the average age of the bridges in the U.S. is 42 years while they are designed for a service life of 75 years. The large number of deficient bridges highlights the need for a better understanding of the effect of aggressive environments on their lifetime performance.

One of the main causes of deterioration of concrete structures is the corrosion of the reinforcement. In coastal regions with airborne sea salt particles or in areas with harsh winters

and high exposure to deicing salts, chloride-induced corrosion is the dominant mechanism of deterioration. In general, there are three stages in the deterioration process of reinforced concrete structures due to chloride-induced corrosion. The first stage is corrosion initiation, governed by the intrusion of chloride ions. During this stage, the chloride ions penetrate into concrete. When the concentration of chloride reaches a threshold value, the reinforcing steel becomes depassivated and corrosion initiates, indicating the end of the first stage. The second stage is crack initiation, controlled by the expansion of corrosion products. After corrosion initiates, steel is consumed and corrosion products (rust) are formed at the interface zone between concrete and steel due to chemical reactions. Rust is a porous material with less strength and larger volume compared to the original steel consumed in the process, thus will gradually fill the porous area around the steel and then pressurize the surrounding concrete, leading to the initiation of concrete cracks and decrement of the bond between concrete and steel, which indicates the end of the second stage. In addition, some research shows that corrosion process not only reduce the cross sectional area of steel, but also decrease material strength of both concrete and steel. The third stage is crack propagation in concrete. The volume expansion of rust leads to crack propagation and finally spalling of concrete cover marking the service failure of the structure. In some cases this service failure is also associated with extreme capacity loss and limit state failure of the structure. Among the three stages, the first stage normally takes the longest time. It can take many years for chloride ions to initiate the corrosion process, depending on the influencing factors, such as water-to-cement ratio of concrete, thickness and quality of concrete cover, ambient temperature and relative humidity. The second stage is shorter than the first one, and also depends on many parameters, such as properties of concrete, composition of corrosion products, corrosion morphology and corrosion

rate. This stage defines the end of functional service life where repair or replacement is required for the corroded RC structures. The third stage is normally the shortest stage among the three. Because the depth of concrete cover is usually 50mm, once cracks are formed around the reinforcement, it will quickly propagate to the surface. Since the chloride-induced corrosion will significantly affect the serviceability and durability of RC structures, it is of great importance to understand the adverse effects of corrosion in reinforcement on structural behavior of reinforced concrete structures. The main features of corrosion effects include reduction of steel cross sectional area both in longitudinal and transverse reinforcement, reduction of strength and ductility in reinforcement, change in properties of concrete both in compression and tension, and deterioration of bond and its dependence on the corrosion level of reinforcement. The lifetime performance of corroded concrete structures can be assessed by the finite element modeling approach. A finite element model which is capable of capturing all the corrosion effects discussed above is in great demand. By investigating the corrosion process and its effect on the structural behavior of RC structures, this study aims to provide an explicit approach to predict the time to crack initiation, as well as a detailed finite element framework to predict the lifetime performance of corroded RC structures.

Moreover, since earthquakes are one of the major natural hazards that impact civil structures, leading to enormous economic loss, and a large number of RC structures that suffer from corrosion mechanisms are located in high seismic risk areas, it is essential to study the structural response of RC structures under both corrosion and earthquake. The goal of this study is to provide a detailed and comprehensive framework that is capable of implementing the time-dependent structural degradation due to chloride-induced corrosion and capturing the response details including damage extent to give a more accurate and reliable prediction for

the lifetime performance of RC structures in multi-threat regions, so that the outcome of this research will help engineers improve their designs, help inspectors identify necessary test regions and define comprehensive test plans, as well as help decision makers optimize rehabilitation strategies under multi-threat scenarios.

Corrosion-induced concrete cover cracking and its initiation time are studied in the second chapter. This chapter starts with a critical review of the analytical and numerical models to predict crack initiation time under both uniform and pitting corrosion, followed by a parametric study on the effect of different parameters on the crack initiation time. Three dimensional (3-D) nonlinear finite element models have been proposed to conduct a sensitivity analysis on the effect of different parameters on the pattern of crack propagation throughout concrete cover for both uniform and pitting corrosion.

Chapter 3 studies the nonlinear model of bond between steel and concrete, and the model of bond deterioration under different corrosion levels of reinforcement. 3-D nonlinear finite element models which are capable of capturing all the main features of corrosion effects have been developed to investigate the lifetime structural performance of corroded RC beams.

Chapter 4 investigates the structural response of reinforced concrete highway bridge columns under earthquake hazards while they are continuously subjected to chloride-induced corrosion. The proposed FE models have been validated by a previous set of experimental test results. The extent of structural degradation has been calculated over the entire life of the bridge. Nonlinear pushover and time history analysis have been conducted to investigate the seismic performance of corroded RC columns at various time during their lifecycle.

Chapter 5 focuses on the development of the framework that is able to evaluate the life cycle performance of RC bridge columns that are subjected to multiple seismic events at

different time periods while they are constantly subjected to chloride attack. A series of earthquake case scenarios have been developed to investigate the structural behavior when the column experiences two earthquake events at different time periods during its lifetime. The extent of damage has been successfully quantified through FE analysis.

Chapter 6 summarizes the findings of this study and the major contributions of the research.

CHAPTER 2. CONCRETE COVER CRACKING AND SERVICE LIFE PREDICTION OF REINFORCED CONCRETE STRUCTURES IN CORROSIVE ENVIRONMENTS

A paper accepted by the journal of *Construction and Building Materials*

Zhen Cui, Alice Alipour

2.1 Abstract

Crack initiation of concrete cover due to corrosion defines the end of functional service life where repair or replacement is required for corroded reinforced concrete (RC) structures. This study provides a comprehensive and critical analysis for the analytical and numerical models of corrosion-induced cover crack initiation for both uniform and non-uniform corrosion. The efficiency and applicability of the existing models have been analyzed. Recommendations on how to select proper models to estimate crack initiation time have been provided. Moreover, parametric studies are conducted to investigate the effects of different factors on crack initiation time and crack propagation patterns using three dimensional nonlinear finite element (FE) models. The results show that the type of corrosion products, thickness of interfacial transition zone and rate of corrosion are the parameters that affect crack initiation time the most significantly. The developed FE models are able to study crack initiation and propagation for both uniform and non-uniform corrosion, as well as quantify the extent of concrete damage due to cracks. The FE results show that crack patterns under uniform and non-uniform corrosion differ. Under uniform corrosion, the major crack occurs vertically in the cover. But under non-uniform corrosion, the two major cracks form diagonally at the location of the pit in the cover. The vertical crack appears later and then becomes the third major crack. The results also show that non-uniform corrosion causes high concentrated pressure at the pits

which would lead to earlier cover cracking. Assuming uniform corrosion may result in unconservative service life estimation. The outcome of the research provides a reliable approach to predict corrosion-induced cover crack initiation and propagation for RC structures.

Keywords: corrosion, concrete cover cracking, finite element analysis, uniform and non-uniform corrosion

2.2 Introduction

The deterioration of infrastructure has been of great concern globally in the recent decades, as the infrastructure is aging, rapidly deteriorating, and becoming increasingly vulnerable to catastrophic failures during probable natural or man-made hazards. One of the main causes of deterioration of concrete structures is the corrosion of reinforcement (Cairns et al. 2005, Val and Chernin 2009, Apostolopoulos et al. 2013). In coastal regions with airborne sea salt particles or areas with harsh winters and high exposure to deicing salts, chloride-induced reinforcement corrosion is the dominant mechanism of deterioration. In general, there are three stages in the deterioration process of reinforced concrete (RC) structures due to chloride-induced corrosion. The first stage is corrosion initiation, governed by the intrusion of chloride ions. The alkaline environment of concrete surrounding reinforcing steel results in the formation of a passive film at the steel surface, which can protect the steel from corrosion. When chloride ions penetrate into the concrete and their concentration reach a threshold value, the PH value changes and the protective film on the reinforcing steel becomes depassivated and corrosion initiates. This is the end of the first stage. The second stage is crack initiation, controlled by the expansion of corrosion products. After corrosion initiates, steel is consumed and corrosion products (rust) are formed at the interface zone between concrete and steel due to chemical reactions with the presence of both moisture and oxygen. Rust is a porous material with less strength and larger volume compared to the original steel consumed in the process, thus will gradually fill the porous area around the steel and then pressurize the surrounding concrete, leading to initiation of concrete cracks when the tensile stress exceeds the tensile strength of surrounding concrete and decrement of the bond between concrete and steel, which indicate the end of the second stage. The third stage is crack propagation in concrete. The

volume expansion of rust leads to crack propagation and eventually spalling of concrete cover marking the service failure of structures. In some cases this service failure is also associated with extreme capacity loss and limit state failure of structures. Among the three stages, the first stage normally takes the longest time. It can take many years for the corrosion process to initiate, depending on the influencing parameters. The second stage defines the end of functional service life where repair or replacement is required for corroded RC structures. The third stage is the shortest stage among the three. Because the depth of concrete cover is usually 50mm, once cracks are formed around the reinforcement, it will quickly propagate to the surface. Since crack initiation of concrete cover caused by corrosion is a critical point in evaluating the service life of corroded RC structures, it is very important to be able to predict crack initiation time with sufficient accuracy.

Extensive research has been conducted on corrosion initiation subjected to various exposure conditions (Shafei et al. 2012 and 2013, Shafei and Alipour 2015a and b), as well as capacity assessment, cyclic response and fragility analysis under different levels of corrosion (Alipour 2010, Alipour et al. 2011, 2012 and 2013, Hanjari et al. 2011, Alipour and Shafei 2014, Cui and Alipour 2014, Kashani et al. 2016a and b, Ni Choine et al. 2016, Rao et al. 2017a). Experimental tests have been conducted to investigate corrosion-induced crack initiation (Andrade at al. 1993, Liu and Weyers 1998, Mangat and Elgarf 1999, Torres-Acosta and Sagues 2004, EI Maaddawy et al. 2005, Mullard and Stewart 2011, Lu et al. 2011, Cornelli et al 2013, Michel et al. 2014), as well as many models have been proposed to predict the crack initiation (Bazant 1979, Molina et al. 1993, Liu and Weyers 1998, EI Maaddawy and Soudki 2007, Chernin and Val 2011, Lu et al 2011). Most of the models have been developed and calibrated based on limited test data, thus it is hard to identify the efficiency of those models,

causing problems when selecting the proper model to estimate the corrosion-induced crack initiation. There are a few articles that reviewed some models available in the literature (Reale and O'Connor 2012, Jamali et al. 2013), however, the articles were more focused on summarizing the previous models and commenting on the models without developing any new methodology to further investigate crack initiation. The models being reviewed do not include the recently proposed crack initiation models and are for uniform corrosion only. Numerical models have also been proposed in the literature (Molina et al. 1993, Chen and Mahadevan 2008, Chernin and Val 2011, Chen and Leung 2015). Some of these models are used for crack propagation and some of them are used for parametric study of the factors affecting crack initiation. However, no numerical models studied both crack propagation and influencing parameters on crack initiation. Moreover, most of the numerical methods are focused on one type of corrosion only, either uniform or non-uniform. This paper aims to provide a critical and comprehensive analysis for the accuracy and applicability of the existing models predicting crack initiation time in the literature for both uniform and non-uniform corrosion, furthermore, to develop an explicit and reliable finite element (FE) approach to investigate crack initiation and propagation for the two types of corrosion. Moreover, based on the developed FE models, parametric studies are conducted in order to assess the effects of different parameters on corrosion-induced concrete cover cracking, as well as the crack propagation patterns for uniform and non-uniform corrosion.

To study the corrosion-induced concrete cover cracking, the following sections will be presented in this paper: i) a critical review for the major analytical models of crack initiation in the literature for both uniform and non-uniform corrosion, ii) an overview and comparison of existing numerical models for both types of corrosion, iii) the development of proposed FE

models for both types of corrosion and the validation, iv) parametric study of factors that affect crack initiation, v) parametric study for crack propagation under uniform corrosion, and vi) crack propagation of non-uniform corrosion. The outcome of this study will provide a solid approach for reliable assessment of the effects of corrosion-induced cracking on the performance of RC structures in the absence of field observations or experimental data.

2.3 Corrosion-induced concrete cover cracking models

A large number of models have been proposed to predict the time to crack initiation, which can be generally divided into three categories: empirical models (Andrade et al. 1993, Rodriguez et al. 1996, Torres-Acosta and Sagues 2004), analytical models (Bazant 1979, Liu and Weyers 1998, EI Maaddawy and Soudki 2007, Yuan and Ji 2009, Chernin et al. 2010, Lu et al 2011, Reale and O'Connor 2012) and numerical models (Molina et al. 1993, Ožbolt et al. 2012, Du et al. 2014, Chen and Leung 2015). The empirical models are normally based on regression analysis of the experimental data and involve simple mathematical equations and the determination of controlling parameters. Analytical models are mainly based on cracking mechanics, involving more parameters and mechanistic considerations.

This section gives a critical overview of existing analytical models of cover cracking, discusses the characteristics of each model, and provides recommendations for applying proper models to estimate the time to crack initiation. In the literature, there are two common types of analytical models to predict the time to crack initiation: the thick-walled uniform cylinder model (TWUC) and the thick-walled double cylinder model (TWDC) (Figure 2-1). The TWUC model assumes the concrete as a single layer, the thickness of which is equal to the thinnest concrete cover. The TWDC model divides the concrete into two parts: a cracked inner cylinder and an un-cracked outer cylinder.

Previous research suggests that not the whole corrosion products contribute to the expansive pressure on the concrete. In fact, some diffuse into the voids and pores of the concrete medium. It has been reported that there is an interfacial transition zone (ITZ) around the steel bar (Al Khalaf and Page 1979, Liu and Weyers 1998, Michel et al. 2011). The corrosion products only exert expansive pressure on the surrounding concrete after this interfacial transition zone is filled. Therefore, the crack initiation time can be treated as the time required for corrosion products to fill the interfacial transition zone and then apply internal pressure to the surrounding concrete until the first crack appears (Figure 2-2). The next stage – crack propagation is the time when additional tensile stress builds up, resulting in cracks appearing on the concrete cover and propagation of cracks that results in spalling. Depending on the service design requirements, a crack width of 1.0 to 3.0mm would mark the service failure of the concrete member (Vu et al. 2005, Washington State Bridge Inspection Manual 2015).

Bazant (1979) was the first to use a TWUC model to predict the time to cover cracking, considering concrete around a steel bar as a thick-walled cylinder subjected to an expansive pressure created by the formation of corrosion products. The stress in the cylinder wall is calculated based on plane strain linear elasticity theory. In this model, the concrete is presented as a homogenous linear elastic material. The rust expansion is modeled by a uniform increase in the diameter of the hole around the steel bar. It is assumed that the rate of rust production is constant. This model has been used extensively in the literature to estimate crack initiation time. Later on, comparisons were made with experimental data and it was shown that the model underestimated the time to crack initiation (Liu and Weyers 1998, Chernin and Val 2011). This

mostly attributes to the fact that this model ignores the ITZ around the rebar and all of the corrosion products contribute immediately to the expansive pressure.

To overcome this issue, Liu and Weyers (1998) modified this model by including the ITZ around the rebar in their calculations. They conducted a series of corrosion experiments on 44 concrete slabs over five years and updated the model based on their observations. In this model, corrosion products first fill the ITZ during the free expansion period and after this zone is filled, the internal pressure is exerted on the surrounding concrete. The concrete around the steel bar is homogeneous elastic and considered as a thick-walled cylinder. It is assumed that the rate of rust production decreases with time, since the diffusion distance of ionic iron increases as the rust layer becomes thicker. The introduction of the ITZ divides the critical amount of corrosion products into two parts: the amount of corrosion products required to fill the ITZ around the interface between steel and concrete, and the amount of corrosion products generating tensile stress to cause concrete cracking. Similar to Bazant's model, the stress required to cause the cracking of concrete cover is equal to the tensile strength of concrete, except that the diameter d is replaced by $d+2\delta$ to reflect the inclusion of the ITZ (δ is the thickness of the ITZ).

In another study, EI Maaddawy and Soudki (2007) noted that assuming a reverse relationship between rust production and time underestimates the steel mass loss and thus overestimates the crack initiation time. To address this issue, they updated the previous model with the consideration of a constant rate of rust production. They merged both of the two above approaches, using the thick wall uniform cylinder model with an ITZ around a steel bar, but keeping the constant rate of rust production.

A more recent study by Wong et al. (2010) reported that most cracks near the interface between concrete and steel were completely filled with corrosion products, and cracks further away are partially filled or had surfaces lined with corrosion products. Therefore, when developing the corrosion-induced concrete cracking models, the effect of a fraction of corrosion products penetrating into these radial cracks on cover cracking time needs to be taken into account. Lu et al. (2011) developed a mathematical model taking into consideration the penetration of rust into open cracks to predict time to cracking for both accelerated and long term natural corrosion. To develop this model, they assumed that concrete is an isotropic linear elastic material which is treated as a thick-walled cylinder around the steel (similar to the previous model). The corrosion process is considered uniform resulting in a uniform radial expansive pressure. The ITZ around the steel-concrete interface is taken into account and during the progress of crack front, some corrosion products diffuse into radial corrosion cracks. In this model, the required amount of corrosion products at the onset of full cracking of concrete cover is calculated with two distinct components: i) the amount of corrosion products required for full cover cracking without taking into consideration corrosion products penetrating into corrosion cracks. In this case, the corresponding radius loss of steel and time are $\Delta d_{st1}/2$ and t_1, respectively. ii) the amount of corrosion products accumulated in the radial cracks during the progress of crack front. The corresponding radius loss of steel and time are $\Delta d_{st2}/2$and t_2, respectively. Therefore, the total time since corrosion initiation to cover cracking is t_1+t_2.

When developing the crack initiation models, some researchers assume that the mechanical properties of rust is similar to those of steel, making the elastic modulus of steel and rust much larger than that of concrete, thus the deformations of steel and rust could be

neglected (Liu and Weyers 1998, EI Maaddawy and Soudki 2007). While other researchers assume that the mechanical properties of rust are approximately equal to those of liquid water (Molina et al 1993). Lu et al. (2011) analyzed the influence of mechanical properties of rust on the critical steel loss percentage that causes cover cracking and showed that the critical percentage is constant when the modulus of rust is greater than 1GPa. Since it is widely accepted that the modulus of rust is greater than 1GPa, the deformation of rust is neglected in their model.

The thick-walled double cylinder (TWDC) model considers the concrete cylinder to be partitioned into two parts: a cracked inner cylinder and an un-cracked outer cylinder (Figure 2-1b). Li et al. (2006) modeled the cracked concrete in the inner cylinder as an anisotropy material but only reducing the elastic modulus in the tangential direction. Pantazopoulou and Papoulia (2011) considered the tangential stiffness of the inner cylinder concrete changed gradually but without giving a clear analytical solution. Based on the two TWDC models, Chernin et al. (2010) resolved their problems and proposed their TWDC model assuming that the concrete in the inner cylinder is orthotropic inhomogeneous linear elastic and the concrete in the outer cylinder is isotropic linear elastic. They claim that the critical radial pressure that causes cover cracking, p_{cr}, is overestimated in TWUC models due to the assumption that the concrete in tension is perfectly plastic. This results in not considering the reduction of radial tensile stress after the development of partial radial cracks. They also account for part of corrosion products penetrating into concrete pores and microcracks before full cover cracking by introducing an equivalent thickness. The results of this study shows that the amount of corrosion products penetrating into concrete pores before full cover cracking may be higher than the ones assumed in previous models such as Liu and Weyers (1998). However, compared

to TWDC models, the TWDC model is more complicated, requiring more computational efforts. The advantage of accounting for part of corrosion products penetrating into concrete pores and microcracks can also be achieved by using the TWUC model developed by Lu et al (2011).

In order to compare different predictive models, the time to crack initiation is calculated using three selected analytical models for five experimental tests. The predicted crack initiation time is then compared with the observed crack initiation time from experiments. The results are summarized in Table 2-1. The data in typed in italic shows the calculated crack initiation time compared with their own experimental result. It can be seen from this table that the predicted time using the model developed by Lu et al. (2011) shows a relatively good agreement with the experimental results except the experiment by Liu and Weyers (1998). This may be due to the reason that the model of Lu et al. (2011) is developed for accelerated corrosions, but the experiments of Liu and Weyers (1998) are under long-term corrosion conditions, which may also explain the reason for the discrepancy between the observed time and the predicted time from EI Maaddawy and Soudki (2007) for the experiments of Liu and Weyers (1998). The accuracy of the predicted time may be also related to the geometry of the specimens in the test from which the model is developed, such as the rebar arrangement in the test specimen. For example, it can be seen that the predicted time for the experiment of Vu et al. (2005) calculated from the model by Liu and Weyers (1998) is more accurate compared with the ones from the other models. This may be because both the experiments of Vu et al. (2005) and Liu and Weyers (1998) are using test specimens that have five embedded rebars, whereas the experiments of Andrade et al. (1993) and Lu et al. (2011) are only involving a

single rebar in concrete and the experiment of EI Maaddawy and Soudki (2007) involves two rebars embedded in concrete.

It can be concluded from above that there is no such model that can predict the crack initiation for all types of structural members and environmental conditions. The predictive models are developed based on the results from particular experimental tests and normally provide more reasonable results for the situation that is similar to the test conditions. For other conditions, the model might give inconsistent results. Furthermore, the value of the predicted time is highly dependent on the value of the input parameters, such as properties of concrete, diameter of reinforcement, depth of concrete cover, thickness of interfacial transition zone, as well as the volumetric ratio of the rust. The volumetric ratio and the density of the rust vary with the types of corrosion products, which depend on the environmental conditions. The thickness of ITZ varies with the environment and a reliable method to measure the ITZ thickness has been lacking (Michel et al. 2011). Such factors introduce significant uncertainties into the prediction of crack initiation time, which result in large scatter in predictions of the crack initiation time.

Most of the analytical models have assumed uniform expansion of corrosion products, which are only applicable to uniform corrosion. However, for chloride-induced corrosion in natural environment, corrosion products are more likely to form locally and tend to accumulate at the steel-concrete interface facing the concrete surface and more probably leads to pitting corrosion (Cao et al. 2013, Cao and Cheung 2014). This will result in higher concentrated pressure on the side facing concrete cover causing faster corrosion progress, and requires a more precise simulation of the non-uniform corrosion-induced cover cracking. Experimental studies have been conducted to investigate pitting corrosion. Kashani et al. (2013) conducted

pitting pattern analysis using a stochastic approach. Apostolopoulos et al. (2013) stuided the pit depths and areas for both bare and embedded steel bars. In order to investigate the distribution of rust and corroded steel, Yuan and Ji (2009) conducted corrosion tests for reinforcement embedded in concrete under artificial climatic environments. It is found that most of corrosion products distributed on the half circumference of the steel bar that faces the concrete cover (Figure 2-3a). Very few corrosion products are found at another half which was away from the concrete cover. The shape of rust distribution can be defined as a half elliptical curve. The distribution of corroded steel is proportional to the thickness distribution of corrosion products due to the expansive nature of corrosion products. Based on this test result, the distribution of rust for side located steel bar before crack initiates can be described using the following expression (in polar coordinates, Figure 2-3b) (Du et al. 2014):

$$\Delta r_\theta = \begin{cases} \frac{(R+\Delta r_{min})(R+\Delta r_{max})}{\sqrt{(R+\Delta r_{min})^2 sin^2\theta + (R+\Delta r_{max})^2 cos^2\theta}} - R & 0 \le \theta \le 180° \\ \Delta r_{min} & 180° \le \theta \le 360° \end{cases} \quad (2\text{-}1)$$

where R is the original radius of the steel, Δr_θ is the radius increase at angle θ, Δr_{max} is the maximum radius increase and Δr_{min} is the minimum radius increase. It is obvious that the radius increase $\Delta r_\theta = \Delta r_{max}$ when $\theta = 90^0$, i.e., nearest to the concrete cover, and $\Delta r_\theta = \Delta r_{min}$ for the side away from the concrete cover. The radio of $\Delta r_{max}/\Delta r_{min}$ determines the shape of the half ellipse curve. For uniform corrosion, $\Delta r_{max}/\Delta r_{min}$ is equal to one.

Since the steel loss of the rebar is proportional to the distribution of the rust layer, based on the analytical model developed by Malumbela et al. (2011), the critical maximum radius increase at crack initiation can be calculated as

$$\Delta r_{crmax} = \frac{(\lambda-1)R\Delta r_{st2} - 2\delta(2R+\delta)}{R+\delta} \quad (2\text{-}2)$$

where Δr_{st2} is the critical maximum radius loss of steel at crack initiation and λ is the volumetric ratio, i.e., the ratio of the volume of corrosion products to that of the consumed steel. This equation is only valid when the ITZ is fully filled or when the numerator of the equation is positive.

Another analytical model for non-uniform corrosion-induced cover cracking is developed by Xia et al. (2012). The model utilizes the complex variable method of Muskhelishvili, which is capable of providing the stresses in concrete surrounding the steel bar at the typical locations: in the middle (side located bar) and at the corner (corner bar). The stresses for the corner bar are calculated from the superposition of stress states of two middle bars. The sides that the two middle bars are close to, respectively, are perpendicular to each other.

Most of the analytical models for non-uniform corrosion are developed in recent years and were based on experimental tests. The majority of them all agree that the rust distribution can be modeled as a half elliptical curve. However, the analytical models are normally developed in two dimensions. Due to the spatiality of pitting corrosion distribution, to obtain an accurate prediction for crack initiation and propagation, it is essential to study cover cracking under non-uniform corrosion in three dimensions. Only a few experimental and numerical studies have considered that, which will be discussed in Section 2.4.

2.4 Existing numerical models

Finite element modeling allows the flexibility of geometric complexities as well as material properties and can provide predictions of corrosion-induced cover cracking, thus can give an alternative way to investigate crack initiation and propagation besides experimental tests, reducing costs of the tests.

A number of numerical models using a finite element (FE) approach have been proposed in the literature to predict corrosion-induced concrete cover cracking (Dagher and Kulendran 1992, Molina et al. 1993, Yokozeki at al. 1997, Toongoenthong and Maekawa 2005, Zhou et al. 2005, Chen and Mahadevan 2008, Val et al. 2009, Ožbolt et al. 2012, Du et al. 2013, Cao 2014, Chen and Leung 2015) (see Table 2-2). The rust accumulated effect is normally modeled by uniform or non-uniform internal pressure, uniform or non-uniform radial displacements or thermal analogy. Most of these studies use two dimensional (2D) models (Dagher and Kulendran 1992, Molina et al. 1993, Yokozeki at al. 1997, Toongoenthong and Maekawa 2005, Zhou et al. 2005, Val et al. 2009, Du at al. 2013, Chen and Leung 2015), with a few using three dimensional (3D) models (Chen and Mahadevan 2008, Ožbolt et al. 2012, Hanjari et al. 2013, Coronelli et al. 2013, Cao 2014). The focus of some studies are to model concrete cracking around one steel bar (Molina et al. 1993, Chen and Mahadevan 2008, Michel et al. 2014 and 2016, Chen and Leung 2015) while other studies model cover cracking around multiple steel bars embedded in concrete (Dagher and Kulendran 1992, Yokozeki at al. 1997, Toongoenthong and Maekawa 2005, Zhou et al. 2005, Val et al. 2009, Ožbolt et al. 2012, Du at al. 2013). A few non-FE numerical models such as 2D mesoscale models considering heterogeneous nature of concrete have been developed in the literature as well (Šavija et al. 2013, Du et al. 2014).

Molina et al. (1993) was one of the few to model the effect of rust production by applying a thermal load on the interface between steel and concrete. In this study, steel and rust are considered as one material with properties changing linearly with time from steel properties to rust properties. The FE results compared to their own experimental results shows some agreement between FE and test results. The discrepancy is attributed to the neglecting of

rust penetration into concrete pores and cracks. Another study by Yokozeki at al. (1997) also assumed linear reduction of Young's modulus of steel with time after corrosion initiation. They estimated the rate of rust production based on water content, cement type, concrete cover and compressive strength. Assuming rust production rate is constant, the critical amount of corrosion products to cause concrete cracking are calculated based on regression analysis of multiple FE results. The results from the regression equation are then compared with experimental results in the literature, showing a relatively good agreement. Zhou et al. (2005) simulated corrosion-induced concrete cracking by imposing a uniform radial displacement around the surface of the steel bar. The damaged plasticity model, which uses isotropic damaged elasticity in combination with isotropic tensile and compressive plasticity (ABAQUS 2012) is selected to model concrete. In another study, Toongoenthong and Maekawa (2005) developed a 2D FE model which considers the diffusion of corrosion products into concrete cracks and obtain a better agreement between FE and experimental results. Their model utilizes joint interface elements to model the interfacial zone between steel and surrounding concrete. In the normal direction, the interface elements have large stiffness in the closure mode and small stiffness in the opening mode. In the transverse direction, these elements have zero stiffness. The study by Chen and Mahadevan (2008) developed a 3D FE model in ANSYS to investigate the corrosion-induced concrete cracking. Only the concrete around the steel is modeled in their simulation. The rust expansion is characterized by a time-varying radial displacement boundary condition. The smeared crack approach is adopted to model the cracking. Hanjari et al. (2013) proposed nonlinear 3D FE models using the program DIANA to study crack patterns and structural effects under high levels of reinforcement corrosion. The applied corrosion model considered the flow of rust through concrete cracks. Solid pyramid

elements were used for both concrete and reinforcement. Concrete material was modeled by smeared rotating crack model. Michel et al. (2014) modeled the corrosion-induced crack explicitly with a 2D FE model in TNO DIANA. The concrete, steel, corrosion layer and crack interface were all modeled. Crack widths were then obtained by FE analysis.

It is noted that most of the numerical models use the 2D plain strain assumption and some of the models are developed without validation against experimental tests. Moreover, most of studies have assumed a uniform corrosion process and are based on the results obtained from accelerated corrosion tests using electrical current in laboratories. However, chloride-induced corrosion in natural environment leads to pitting corrosion. In recent years, numerous effects have been made to develop numerical models for cover cracking under non-uniform corrosion.

Du et al. (2014) developed a 2D numerical model to explore the cracking behavior of concrete cover under non-uniform corrosion by applying a radial displacement with a half ellipse shape on the hole in the concrete. The ratio of maximum to minimum displacement is taken as 20-30. The model involves concrete material only, and the concrete is modeled as a heterogeneous material on the meso-scale. The FE model proposed by Du et al. (2006) simulates rust expansion by applying a nearly elliptically distributed radial displacement for non-uniform corrosion in addition to a uniform radial displacement for uniform corrosion. The ratio of maximum to minimum displacement applied to the hole is a constant, which is equal to five. Jang and Oh (2010) proposed a 2D FE model to study the cracking pressure with different pitting factors under non-uniform corrosion. The rust expansion is simulated by applying a non-uniform radial pressure on the concrete hole. The distribution of pressure varies according to the value of the pitting factor (α_p=1, 2, 4 and 8). The 2D model developed by

Chen and Leung (2013) includes concrete, steel bar as well as rust. The non-uniform cover cracking is simulated by the discrete crack model. The interaction between concrete and rust is modeled by interface elements with cohesion and a friction coefficient. Most of numerical models for non-uniform corrosion are developed in two dimensions only. Very few numerical studies consider three dimensional pit shapes, such as Hingorani et al. (2013) and Li et al. (2014), but focus on non-uniform corrosion effect on the properties of corroded steel. However, due to the spatial nature of pit distribution, it is necessary to model the cover cracking under non-uniform in three dimensions in order to attain a more accurate prediction. In this study, a 3D FE model is developed and is capable of considering the spatial distribution of corrosion pits. The details of the FE models will be discussed in the next section.

Currently, there are three ways to model the effect of rust expansion: radial pressure, radial displacement and thermal analogy. For modeling uniform corrosion, uniform expansion of rust leads to uniform stresses or displacements only for the symmetric structures with symmetric boundary conditions. For the cases with asymmetric boundary conditions, such as the steel bar at the corner, the radial pressure or displacement caused by rust expansion is not uniform. Hence applying a uniform stress or displacement will lead to erroneous results. Chernin and Val (2011) developed 2D FE models to estimate the critical increase in the diameter of a corner bar in a fragment of a RC slab using the three approaches. The results show that applying radial pressure or displacement will significantly overestimate the critical increase in the diameter that induces cover cracking. In addition, with the application of radial pressure or displacement method, steel is not included in the model. This will not allow the consideration of the interaction between steel and concrete. And also, when the steel is not simulated, the model is only correct under no external loading. With the thermal analogy

method, which utilizes the increase of temperature to expand the steel volume to simulate the radial expansion, the boundary condition issue will be overcome. Moreover, since the steel is also modeled, the simulation will be capable of considering the steel-concrete interaction that may affect the crack initiation and propagation, as well as considering the cracking under loading conditions. Therefore, the equivalent thermal analogy is adopted in this study to model the rust expansion.

2.5 The proposed finite element model and its validation

Finite element models are proposed in this paper in order to predict the time from corrosion initiation to crack initiation. In order to validate the FE models, the results in this paper will be compared to the experimental results. Andrade et al. (1993) conducted a series of the experimental tests on small RC beams which were corroded by an impressed current, in order to study the crack initiation time. The specimen in the test are 150mm×150mm×380mm concrete cubes. A 16mm single rebar is embedded in each cube with a cover depth of 20mm. The tensile strength of concrete is 3.55MPa. The time from corrosion initiation to the first visible crack according to the experiment is 96 hours. A three dimensional FE model has been developed in ABAQUS (69) (Figure 2-4a). The damaged plasticity model is used for concrete elements in the model. The damaged plasticity model takes into consideration the degradation of the elastic stiffness induced by plastic straining both in tension and compression. It assumes that the two main failure mechanisms are tensile cracking and compressive crushing. The steel is modeled as a linear elastic material with a Young's modulus of 200GPa and a Poisson's ratio of 0.33. The steel and concrete are assumed to be perfectly bonded. The expansive nature of corrosion products is modeled by thermal analogy. The increase of the rebar diameter due to formation of rust products can be calculated as follows:

$$\Delta d = \alpha T d \tag{2-3}$$

where d is the original diameter of the steel bar, T is temperature, and α is the thermal expansion coefficient of steel, taken as 1.17×10^{-5}m/(m·K). In the FE model, the increase of temperature in the steel is achieved by defining a temperature field in the rebar. The temperature in the steel increases linearly with time causing the increase of the rebar diameter.

After applying the thermal expansion, the crack initiation time has been calculated to be 81 hours, a little bit shorter than the experimental results (96 hours). The reason for the discrepancy between the FE result and the test result can be that the critical time in the test is the time to the first visible crack, which according to the test, is about 50μm in width appearing on the surface of the concrete, but the critical time based on FE analysis is the time when the maximum principle tensile stress exceeds the tensile strength of concrete in the first element, which is near the steel-concrete interface. The tensile strength corresponds to the start of micro-cracking in concrete. The formation of micro-cracks is represented macroscopically with a softening stress-strain behavior beyond the tensile strength. Therefore, it is earlier than the time to the first visible crack in the experimental test where it is detected on the surface of the concrete.

Cracks occur in the direction which is perpendicular to the maximum principal strain. Figure 2-4b shows the crack pattern in terms of maximum principle strains. It can be seen from this figure that the main crack occurs in the vertical direction in the top cover of concrete, and the secondary cracks are in the direction of 135 and -135 degrees with respect to the vertical axis. This result matches the result from the model by Andrade et al. (1993).

The experimental test on RC beams by Dong et al. (2011) is selected to validate the applicability of our FE models in cases with multiple embedded bars. In their study, a

240mm×200mm×130mm concrete specimen with three 16mm reinforcement was tested in accelerated conditions. The spacing between the reinforcement is 60mm. The concrete cover depth is 32mm. The material properties of concrete are f_t=1.92MPa, f_c'=31MPa, E_c=26200MPa and v=0.18. The FE model of the test specimen is shown in Figure 2-5a. The same assumptions as the previous case are used to model the concrete, steel and their interface, as well as the rust expansion mechanism. The crack pattern is shown in Figure 2-5b. It can be seen that the crack pattern obtained from the FE model is similar to the one obtained from the experimental test (Figure 2-5c). This validated FE model is selected for further parametric studies in the next two sections.

For non-uniform corrosion, corrosion pits can be irregular, conical, spheroidal, cylindrical, or a transitional shape. For reinforcement subjected to chloride attack, spheroidal pits are the major pit shape (Xu and Qian 2013). Therefore, the pit shape in both transverse and longitudinal directions is considered as a half elliptical shape. And the three dimensional pit is modeled as a half ellipsoid characterized by its semi-axes: pit length, width and depth. Some research shows that the surface diameter of a natural pit of a metal is often equal to or smaller than the pit depth (Codaro et al. 2002). Zhang et al. (2011) assumes the rust distribution as a half elliptical curve in both radial and longitudinal directions based on plenty of their inspections (Figure 2-6).

The number of numerical models considering three dimensional pit shapes is very limited. In this study, a three dimensional finite element model is developed to investigate the effect of non-uniform corrosion on cracking behavior of concrete cover. The dimension of the FE model is the same as the one shown in Figure 2-4a. The damaged plasticity model is adopted for concrete elements. The expansive behavior of corrosion products is simulated by thermal

analogy. It is assumed that the three dimensional rust has a shape similar to a hollow elliptic cylinder. In the plane of steel cross section, the rust have a half elliptical shape on the side facing concrete cover and a half circular shape on the other side. In the longitudinal direction, within the length of each pit, it is assumed that the distribution of rust is uniform instead of elliptical just for simplicity. It is assumed that there are four pits along the length of reinforcement and the pits are distributed evenly in the longitudinal direction. In order to achieve the half elliptical rust expansion on the side facing concrete cover at the pit (θ from 0° to 180°), a different thermal coefficient is assigned to each direction of the FE element at the pit for θ from 0° to 90° (Figure 2-7). Each color in Figure 2-7 standards for a different value of thermal coefficient, α. α is increasing when θ changes from 0° to 90° and decreasing when θ changes from 90° to 180°. The value of the thermal coefficient in each direction is calculated based on Equation 2-1. For θ ranges from 180° to 360°, the rust distribution at the pit follows a circular shape. Thus a constant thermal coefficient is used for θ from 180° to 360°. For the rest of the steel where there is no pit, a zero value of the thermal coefficient is used. The results will be shown in Section 2.8.

2.6 Parametric study

One of the main goals of the study is to recommend geometrical and material characteristics that increase the time to crack initiation as well as crack propagation to concrete surface. For this purpose, a series of parameters have been studied. For parameter such as rust type, ITZ thickness and corrosion rate, analytical models are used to conduct the parametric studies due to the limitation of the macro-scale numerical models. For parameter such as cover depth, rebar diameter and concrete properties, FE modeling are used to conduct the parametric studies.

2.6.1 Type of corrosion products

A mixture of different oxides or hydroxides is produced during corrosion process (Table 2-3). The composition of corrosion products varies depending on the environment. Corrosion products accumulated at the interface between concrete and steel normally appear uniform, but sometimes a layered structure of light and darker bands can be observed. These layers may result from different levels of oxidation depending on the availability of oxygen (Wong et al. 2010). Bazant (1979) considered only the contribution of $Fe(OH)_3$ to the volume expansion (γ=0.523), while Liu and Weyers (1998) assumed a combination of $Fe(OH)_3$ and $Fe(OH)_2$ (γ varies from 0.523 to 0.622), with an average value of 0.57, and EI Maaddawy and Soudki (2007) considered $Fe(OH)_2$ as the only corrosion product (γ=0.622). Some investigations (Vu et al. 2005, Marcotte and Hansson 2007) showed that the equivalent volumetric ratio λ was typically between 2 and 3. Some researchers (Yokozeki et al. 1997, Chernin et al. 2010) estimated the ratio λ was around 3.0. As the value 3.0 is close to the volumetric ratio of Geothite (α-FeOOH), Lu et al. (2011) concluded that Geothite was the main component in the corrosion products. The most recent study by Moreno et al. 2015 confirmed the presence of goethite (α-FeOOH), akaganeite (β-FeOOH) and lepidocrocite (γ-FeOOH) by investigating an actual structure in a marine environment that is exposed to long-term natural corrosion. Both goethite and lepidocrocite are found in highly corroded reigions.

The expansive pressure is expected to vary depending on the composition of the corrosion products. Therefore, the value of λ has a crucial effect on the accuracy of time to crack initiation model. Figure 2-8a shows the effect of the volumetric ratio λ on crack initiation time using different analytical models. It can be seen that the increase of λ will reduce the crack initiation time based on the model by Lu et al. (2011). This trend agrees with the regression

equations developed by Yokozeki et al. (1997) for calculating the critical time to concrete cracking. In the models developed by Liu and Weyer (1998) and EI Maaddawy and Soudki (2007), the crack initiation time also decreases with the increase in λ from 1 to 2, but when λ is in the range of 2-3, which is believed to be the realistic value for most situations, the models by Liu and Weyer (1998) and EI Maaddawy and Soudki (2007) result in an increase in crack initiation time as λ increases. The reason is that the crack initiation time in both of the models by Liu and Weyer (1998) and EI Maaddawy and Soudki (2007) is determined in terms of molecular weight ratio γ and change monotonically with γ, while the crack initiation time in the models by Yokozeki et al. (1997) and Lu et al. (2011) is determined in terms of volumetric ratio λ and change monotonically with λ. When λ is ranging from 4 to 6.15, all of the analytical models result in similar crack initiation time.

2.6.2 Thickness of interfacial transition zone

Liu and Weyers (1998) included the penetration of chloride ions into ITZ in calculation of crack initiation time. It was hypothesized in this study that the corrosion products first filled up the porous area around the rebar and then the excess material started to exert pressure to the surrounding concrete. The same approach was adopted by EI Maaddawy and Soudki (2007). Liu and Weyers (1998) assumed the thickness of ITZ, δ, was equal to 12.5μm, while EI Maaddawy and Soudki (2007) believed that 10-20μm was the typically range of δ. Petre-Lazar and Gérard (2000) stated that δ varied from 2 to 8μm depending on the degree of hydration and water-to-cement ratio. A more recent study by Michel et al. (2011) reported that the value of δ was between 90 and 180μm under an accelerated corrosion condition with a very high current density of 250μA/cm^2. In another study by Chernin et al. (2010), it was demonstrated that the estimated values of the ITZ thickness were larger than 20μm in many cases. They also

found that there was a strong linear relationship between the ITZ thickness and time to cover cracking, which indicates that corrosion products continuously penetrate into concrete pores and microcracks before concrete cover is fully cracked, not only until the ITZ is filled. In the TWDC model that they developed, an equivalent thickness is used to represent the amount of corrosion products that penetrate into concrete pores and cracks before full cover cracking.

Although a common approach is to idealize the ITZ with a cylinder gap around the steel rebar, this method has been questioned recently. For instance, Jamali et al. (2013) mentions that there is no distinct border between the ITZ and steel or the surrounding concrete. This is due to the fact that the concrete is a porous material, so where to delineate the border between the ITZ and the concrete is difficult. Furthermore, the porosity around the steel bar may differ at different locations. For example, the concrete near the top side of the reinforcement is denser than that on the bottom side, and finally the rate of filling pores with rust material is highly dependent on the corrosion rate, transport phenomena and pore solution chemistry.

It is understood that the thickness of ITZ is difficult to validly assess, but nevertheless the chosen value significantly influences the predicted value of time to cover cracking. The relationship between crack initiation time and ITZ thickness has been plotted in Figure 2-8b based on different analytical models. It is shown that the crack initiation time increases dramatically as the thickness of ITZ increases, particularly when using the model developed by Liu and Weyers (1998).

2.6.3 Corrosion rate

Many factors that can influence corrosion rate, i_{corr}, such as temperature, moisture, availability of oxygen, alkalinity of pore water, electrical resistivity of concrete and composition of steel

(Jamali et al. 2013). Most of these factors vary significantly depending on environmental conditions. It has been reported that the crack initiation time is inversely proportional to the corrosion rate. This is due to the fact that the corrosion process may slow down over the time as the surface of the remaining steel is no more accessible for electrochemical reaction due to the formation of corrosion product layers around the steel.

In the studies related to corrosion-induced cracking, mostly accelerated conditions are implemented. The current density of accelerated corrosion tests is typically 100μA/cm^2 or above, which is much higher than the rate of natural corrosion. Figures 2-8c and d show the effect of corrosion rate, i_{corr}, on the crack initiation time using three different analytical models. It can be seen that all the models result in similar crack initiation time. Figure 8c shows the effect of i_{corr} on crack initiation time for a corrosion rate up to 100μA/cm^2, which is a typical value for accelerated corrosion. Figure 2-8d shows the effect of i_{corr} on crack initiation time on a smaller scale, with a corrosion rate from 1 to 10μA/cm^2, which is the normal range of corrosion rate for natural corrosion. Although the high corrosion rate may affect the accuracy of the prediction models, all models agree on the point that the crack initiation time decreases dramatically with the increase in corrosion rate.

2.6.4 Cover depth

Concrete cover depth is a geometrical property that strongly affects the crack initiation time, thus is included as a parameter in most of the empirical or analytical models. As the cover depth increases, the crack initiation time increases (Lu et al. 2011). Figure 2-9a presents the crack initiation time with respect to concrete cover depth for the concrete specimen with multiple bars introduced in Section 2.5 (Figure 2-5a). These results are obtained from FE analysis and are in good agreement with previous observations on the effect of concrete cover,

which is due to the increase in critical pressure required to crack concrete and in the amount of corrosion products diffusing into concrete voids. Furthermore, the increase of the concrete cover increases the time for chloride to reach the surface of the steel and decreases the oxygen in the corrosion process which decreases corrosion rate. Therefore, increasing the cover depth can effectively increase the crack initiation time, consequently, is a direct approach to enhance the structural durability.

2.6.5 Diameter of reinforcement

The diameter of the steel bar, *d*, has an influence on the total amount of corrosion products and thus the crack formation process. In addition, it affects the thickness of the ITZ, which is one of the parameters in the predictive model. The larger value of the diameter *d*, the larger volume of the ITZ it implies. Most of the experimental tests shows that the crack initiation time decreases with the increase of the rebar diameter (Mullard and Stewart 2011, Al-Harthy et al. 2011). Empirical models such as Rodriguez et al. (1996), Alonso et al. (1998) show a similar trend, although a few models shows the opposite (Morinaga 1988, Liu and Weyers 1998).

The ratio of cover depth to rebar diameter, *c*/*d*, can also be used to jointly examine the effect of cover thickness, *c,* and rebar diameter, *d,* on crack initiation time. Figure 2-9b shows the effect of *c*/*d* on crack initiation time based on the FE analysis for the concrete specimen with multiple bars (Figure 2-5a). The range of the *c*/*d* ratio satisfies the ACI code (80). It can be seen that the crack initiation time increases as *c*/*d* increases. It is clear that for the RC members with the same cover thickness, choosing a smaller rebar will result in longer crack initiation time.

The distance between the rebars, *s*, can also affect the crack initiation time (Bazant 1979). The pattern of crack propagation and cover spalling depends on the arrangement of

rebars in the concrete member. Most of the analytical models in the literature do not include this parameter, except for the model developed by Bazant (1979). The ratio of rebar spacing to diameter, *s*/*d*, can be used to assess the effect of rebar spacing, *s*, and rebar diameter, *d,* on crack initiation time. Figure 2-9c is plotted based on the FE analysis. The range of the *s*/*d* ratio satisfies the ACI code (2011). It can be seen that the crack initiation time increases with the increase in *s*/*d*. For the concrete members with the same rebar diameter, increasing the distance between the reinforcement will result in the increase in crack initiation time.

2.6.6 Properties of concrete – Tensile strength, elastic modulus and creep

Effects of concrete tensile strength on crack initiation time has been studied by many researchers, however, there is not an agreement to be achieved. Some experiments show that crack initiation time decreases with the increase of concrete strength, i.e. concrete quality (Rodriguez et al. 1996, Alonso et al. 1998, Vu et al. 2005, Al-Harthy et al. 2011). A recent experimental test by Mullard and Stewart (2011) found that crack propagation rate increases with a higher concrete strength. When the compressive strength of concrete increases by 70%, the crack propagation rate increases by 50%. The observation that cracking occurs slowly in low quality concrete (i.e. with lower strength) is most likely due to the high porosity in low strength concrete. The high porosity will allow a longer time for corrosion products to penetrate into concrete pores and voids before causing any pressure on the surrounding concrete and thus delaying crack initiation time. Although after these pores are filled, cracking would occur faster due to the weaker microstructure of low quality concrete, the time that it takes to fill out the ITZ compensate for the faster crack formation. However, corrosion initiation time is likely to reduce with the use of low quality concrete due to its high porosity making chloride more easily ingress into the concrete. When considering the whole deterioration process, corrosion

initiation time is more dominant, since it is normally the longest among three stages of deterioration process.

A group of other experimental tests shows that concrete quality has no effect on crack initiation (Williamson and Clark 2000, Torres-Acosta and Sagues 2004). Some other research shows crack initiation time increases slightly with the increase of concrete strength (Yokozeki et al. 1997, Zhou et al. 2005). Most of the analytical and numerical models suggest that an increase of tensile strength leads to an increase in crack initiation time (Bazant 1979, Liu and Weyers 1998, El Maaddawy and Soudki 2007, Lu et al. 2011), if keeping other variables constant.

According to the analytical models proposed by Liu and Weyers (1998), El Maaddawy and Soudki (2007) and Lu et al. (2011), the crack initiation time increases with the increase of $f_t/E_{eff}=(1+\varphi_{cr})f_t/E_c$ (f_t is the tensile strength of concrete and E_{eff} is the effective elastic modulus of concrete, calculated by the elastic modulus of concrete, E_c, divided by one plus the creep coefficient, φ_{cr}). Since enhancing concrete tensile strength, f_t, will simultaneously increase the elastic modulus E_c, instead of considering f_t alone, the ratio of f'_t/E_{eff} should be taken into account. Tensile strength of concrete is often estimated from compressive strength of concrete, f'_c. According to ACI, the average splitting tensile strength of concrete is approximately equal to $6.7\sqrt{f'_c}$ (psi) which is $0.56\sqrt{f'_c}$ (MPa) for nornalweight concrete. Modulus of elasticity, E_c, is taken as $57000\sqrt{f'_c}$ (psi) which is $4733\sqrt{f'_c}$ (MPa) for normalweight concrete. It can be seen that both f_t and E_c are expressed as a function of $\sqrt{f'_c}$. The effect of concrete tensile strength will cancel out in the analytical models by Liu and Weyers (1998), El Maaddawy and Soudki (2007) or Lu et al. (2011), if ACI equations are applied. Since different design codes may have different recommended values for f_t and E_c, the calculation may result in inconsistent results.

For example, the effect of tensile strength will also cancel out when CSA (1994) equations (f_t=0.94$\sqrt{f_c'}$ (MPa), E_c= 4500$\sqrt{f_c'}$ (MPa)) are adopted. But if Eurocode 2 (2004) equations are applied, the ratio of f'_t/E_{eff} is increasing as concrete strength increases, which results in the increase in crack initiation time. Therefore, it can be concluded that in the above analytical models, the effect of concrete tensile strength on crack initiation depends on how the concrete tensile strength and elastic modulus are estimated prior to the calculation of crack initiation time.

It is noted that the value of creep coefficient significantly affects the crack initiation time in most of the analytical models and the crack initiation time increases linearly with the creep coefficient φ_{cr}. Creep is mainly influenced by loading time and rate, concrete compressive strength, concrete age, cement and aggregate type, as well as ambient relative humidity. It increases gradually with time after two to five years until it reaches its final value, depending on concrete strength and other factors. Thus, for the same concrete, neglecting the effect of change in creep coefficient can be small if corrosion cracks occur in a couple of years after the structure is built. For concrete with different strengths, high strength concrete shows less creep than low strength concrete (Nilson et al. 2004). The creep coefficient for concrete with strength of 21MPa is 3.1, compared to the creep coefficient of 2.0 for concrete with strength of 55MPa. However, most of the studies comment on analytical models assuming a constant creep coefficient for different compressive strengths, which may lead to inconsistent results for the effect of tensile strength on crack initiation. In addition, whether corrosion affects concrete creep has not yet been researched.

Figure 2-9d shows the effect of concrete tensile strength on crack initiation time from the FE analysis for the concrete specimen with multiple bars. The crack initiation time

increases slowly with the tensile strength, which would generally agree with those analytical models. This is due to the fact that the f_t/E_{eff} ratio of concrete is defined to increases with the concrete strength.

2.6.7 Corrosion mechanism

Reinforcing steel embedded in concrete is normally subjected to two different types of corrosion mechanisms: uniform corrosion and pitting corrosion. Uniform corrosion is commonly inherent to carbonation-induced corrosion. For chloride-induced corrosion in natural environment, pitting pattern is usually the dominant mechanism. In this case, corrosion products tend to accumulate at the steel-concrete interface facing the concrete surface (Cao and Cheung 2014), due to the fact that the chloride ions diffuse into the concrete medium through the surface of the member and reach the face of the steel closer to the surface first. All the studies through experimental, analytical or numerical approaches agree that the crack pattern of non-uniform corrosion is different from that of uniform corrosion. Compared to uniform corrosion, non-uniform corrosion causes higher concentrated pressure on the side facing concrete cover and leads to earlier cover cracking. The assumption of uniform corrosion may result in unconservative estimation for the service life of structures. Parametric study indicates that cover cracking time for non-uniform corrosion decreases with the bar diameter and increases with the cover thickness and concrete strength (Jang and Oh 2010, Du et al. 2014). The crack initiation occurs earlier for the bars located on the corners compared to those on the sides as the intrusion of chloride could happen from two directions in the former case.

Research has shown that the corrosion mechanism changes as chloride-induced corrosion proceeds. According to the experimental results under natural corrosion environment from Zhang et al. (2010), pitting corrosion is the dominant corrosion mechanism at crack

initiation and the beginning of crack propagation. General corrosion progresses very slowly at this stage and cracks are always short and narrow. At the later stage of crack propagation, general corrosion develops rapidly and gradually becomes the dominant mechanism, although some deeper pitting still exists. At this stage, the longitudinal cracks interconnect and grow wider.

2.7 Parametric study for crack propagation

The FE models developed in Section 2.5 (Figure 2-5a) are used to conduct a sensitivity analysis on the effect of different parameters on the crack propagation pattern throughout concrete cover. Figures 2-10(a) - (e) shows the effect of variation in concrete cover depth on the crack pattern through the concrete cover. Each row presents a specific cover depth (20, 30, 40, 50 and 60mm) and since the rebar diameter has been kept similar for all cases, each row represents the c/d of 1.250, 1.875, 2.500, 3.125 and 3.750, respectively. As mentioned earlier, the rust expansion is applied through the application of temperature increase to the steel rebar. The change in temperature has been applied equally to all the rebars. The results are shown at 81 (Column 1), 96 (Column 2) and 131 (Column 3) hours, respectively.

It can be seen from the figures that the cracks propagate in the concrete cover along two side bars, but not fully propagate along the middle bar. This can be explained by the mechanism that the internal radial stress caused by rust expansion acts on the concrete around the three bars. Two of the three bars are at free ends, which means there is no external force to counteract the expansive force. Therefore, it is easier for corrosion cracks to propagate along two side bars. Conversely, for the middle bar, the expansive stresses of two side bars act on the concrete surrounding the middle bar as compressive stresses, thus the tensile stress in

concrete around the middle bar reduces. As a result, it is more difficult for corrosion cracks to occur along the middle bar.

It can also be seen that the cracks become more severe when the concrete cover decreases, as stated in Section 2.6.4. Moreover, it is noted that the crack propagation patterns vary with different cover depths. For the cover depth of 20mm, the cracks appear initially in the vertical direction below the two side bars (see Figure 2-10a1), followed by the formation of horizontal cracks between the bars (Figure 2-10a2). The spalling of concrete cover then occurs due to the severe vertical cracks below two side bars. And the diagonal cracks along two side bars also propagate towards the side surfaces of concrete (see Figure 2-10a3). For the cover depth of 30mm, cracks occur initially in the horizontal direction between the bars (Figure 2-10b1), followed by the slight inclined cracks below two side bars propagating through the bottom concrete cover (Figures 2-10b2 and 2-10b3). Two major diagonal cracks (45 and 135 degrees to the y axis, respectively) along each side bar also develop and propagate towards the side surface (see Figure 2-10b3). When the cover depth increases to 40mm, the cracks initiate horizontally between the reinforcing bars (see Figure 2-10c1). Then, the two diagonal cracks along each side bar occur 45 and 135 degrees to the y axis, respectively (Figures 2-10c2 and 2-9c3). It can be seen from Figure 2-10c3 that the bottom surface cracks are much less severe, compared to the one with 20mm cover depth, proving that increasing the cover depth can efficiently slow down the cracking of concrete cover. The most severe cracks in concrete with the cover depth of 40mm are the 135 degree diagonal cracks along the two side bars. With the further increase of cover depth to 50mm, the cracks first occur horizontally between the reinforcing bars (Figure 2-10d1), then occur diagonally (45 and 135 degrees to the y axis, respectively) along each side bar (Figure 2-10d2). It is shown in Figure 2-10d3 that the 135

degree diagonal cracks along the two side bars towards the bottom are more severe than the 45 degree diagonal cracks along side bars towards the top. For the cover depth of 60mm at the bottom, the cracks also initiates horizontally between the bars (see Figure 2-10e1), followed by the two diagonal cracks (45 and 135 degrees to the y axis, respectively) along each side bar (see Figure 2-10e2). As shown in Figure 2-10e3, a horizontal crack along each side bar develops later propagating though the side covers of concrete. This is because the depth of the side concrete cover is 52mm, which is smaller than the depth of the bottom cover 60mm. Among all the above FE results, it can be seen that the horizontal cracks between bars occurs first, except for the one with 20mm cover depth. This is due to the fact that half of the clear spacing between bars for all cases is 22mm, which is smaller than the cover depths of 30-60mm. The crack occurs between bars first for cases with 30-60mm covers. For the one with the cover of 20mm, since the cover depth is smaller than half of the clear spacing, the crack first occurs vertically in the cover instead of propagating horizontally between the bars. It should be noted that although increasing cover depth can effectively slow down crack propagation process in concrete cover, there should be an optimum cover depth for a structural member, such as for a column, since a high cover depth will result in a weaker core eventually.

Figure 2-11 shows the crack patterns for different cover depth to bar diameter ratios c/d, for the same time period of 131 hours. It is shown that with the decease of c/d ratio, the cracks become more severe, proving that the increase of c/d ratio can delay the cracking of concrete cover, as stated in Section 2.6.5.When c/d is 3.5 (d=10mm), as shown in Figure 2-11a, the cracks are mild. The major cracks are the horizontal cracks between bars and the diagonal cracks along two side bars (45 and 135 degrees to the y axis, respectively). When c/d is 2.8 (d=12mm) (Figure 2-11b), the 135 degree diagonal cracks tend to become vertical cracks

below the two side bars and the horizontal cracks between bars becomes moderate. When c/d reduces to 2.0 (d=16mm), the cracks between bars in the horizontal direction tend to be more severe, so do the vertical cracks below the side bars (Figure 2-11c). As c/d further decreases to 1.2 (d=24mm), it is obvious that the crack pattern includes the severe horizontal cracks between bars, the two severe vertical cracks below side bars and the 45 degree diagonal cracks along side bars (Figure 2-11d). With the c/d of 0.8 (d=30mm), the horizontal cracks between bars become more severe. The vertical cracks below side bars become more severe as well, resulting in the spalling of concrete cover (Figure 2-11e).

In order to quantify the severity of damage that concrete cracks cause on the corroded structures, the number of cracked elements on the bottom or side surfaces of the FE models are recorded, as well as the total number of cracked elements in the entire concrete block. In the concrete damaged plasticity model, isotropic damage elasticity combined with isotropic tensile plasticity is utilized to represent the inelastic behavior of concrete in tension. The tensile damage (d_t) accounts for the degradation of the elastic stiffness induced by plastic straining in tension. A higher tensile damage corresponds to a lower tensile stress. If concrete is still in the elastic range, the tensile damage is equal to zero. Based on the stress-strain relationship of concrete in tension shown in Figure 2-12a, the tensile stress of concrete can be divided into three stages: 54-100%, 9-54%, 0-9% of tensile strength, corresponding to three stages of tensile damage, d_t, in concrete: moderate ($0<d_t<0.7$), severe ($0.7 \leq d_t \leq 0.95$) and most severe ($0.95<dt<1$) damage (Figure 2-12b). A cracked element in the following discussion refers to an element of which both the maximum principle plastic strain and the tensile equivalent plastic strain (ABAQUS 2012) are greater than zero, which equivalently means $d_t>0$. The percentages of total number of cracked concrete elements in the entire concrete model with a

cover depth of 20mm, 30mm, 40mm, 50mm and 60mm, are 33.8%, 32.9%, 32.0%, 30.2% and 27.4%, respectively (Figures 2-10a3-e3). The rebar diameter (16mm) and the time period (131h) are kept the same for all cases. The drop of the cracked element percentage with the increase of cover depth indicates that cracks are more severe in a structure with a smaller cover depth and propagate more slowly in a structure with larger concrete cover depth.

Figure 2-13a shows the percentages of the numbers of cracked elements that fall within the three stages of tensile damage to the number of total cracked elements for a cover depth of 20-60mm, demonstrating that the extent of damage severity varies with the depth of concrete cover. With the cover depth of 20mm, the number of cracked elements with most severe damage takes up 43.2% of the total cracked elements. As the cover depth is increasing, this percentage is decreasing. With the cover depth of 60mm, the percentage of most severely damaged elements reduces to 27.2%. The elements with moderate damage and severe damage for the model with the 20mm concrete cover are 40.4% and 16.4%, respectively. These numbers increase to 43.8% and 29.1% for the one with the 60mm cover depth. For those with a cover depth of 30-50mm, although the numbers of elements with moderate and severe damage do not change linearly with the cover depth, the sum of the two increases as cover depth increases. The severity of tensile damage, i.e., the magnitude of d_t, shows the stress status of the concrete, thus indicates the severity of cracks. An element with the most severe damage (d_t >0.95), only retains less than 9% of original tensile strength, f_t, which can be neglected. This suggests the element experiences the most severe crack. When the cover depth decreases from 60mm to 20mm, the percentage of elements with d_t >0.95 in cracked elements rises from 27.2% to 43.2%. This clearly shows the structure with a smaller cover depth experiences more severe cracks.

The numbers of cracked elements at both bottom and side surfaces for different cover depths, and the time when cracking reaches those surfaces are also recorded for the cases shown in Figures 2-10a3-e3. It can be known from the FE analysis, with the cover depth of 20, 30 and 40mm, a crack occurs below each of the two side reinforcements on the bottom surface. There is no crack at both side surfaces. With the cover depth of 50mm, cracks occur at both bottom and side surfaces. And with the cover depth of 60mm, cracks only occur horizontally at side surfaces. For the models with cover depths of 20-50mm, the same mesh size and element number (360 elements in total) are used at the bottom surface. There are 53, 32, 26 and 18 cracked elements at the bottom surface, respectively, with the cover depth of 20, 30, 40 and 50mm. With the cover depth of 50 and 60mm, 20 and 10 elements crack at each side surface, respectively. The thicker concrete cover is, the less cracked elements are at the surface, which indicates cracks are more severe in the model with a thinner cover. For the case with 60mm cover depth, instead of bottom cracks, a horizontal crack at each side bar propagates toward the side cover. This is because the side cover (52mm) is thinner than the bottom cover (60mm). The time when cracking reaches bottom surfaces is 76, 83, 90 and 97 hours, respectively, for the cover depth of 20, 30, 40 and 50mm. This linear increase shows increasing cover depth delays concrete cover cracking.

For the cases with different rebar diameters (Figure 2-11), the numbers of cracked concrete elements in the entire concrete block, as well as at bottom or side surfaces are recorded. The number of total cracked concrete elements in entire concrete model takes up to 28.0%, 29.4%, 32.6%, 36.3% and 39.0%, respectively, for the model with a rebar diameter of 10mm, 12mm, 16mm, 24mm and 30mm at the same time period (131h). The percentage of cracked elements increases as the rebar diameter increases, showing that a structure with larger

diameters of reinforcement experiences more severe cracks. Figure 2-13b shows the variation of d_t in cracked elements in each of the three ranges with different rebar diameters. It can be seen that the percentage of elements with the most severe damage in cracked elements rises from 19.7% to 47.6% when the rebar diameter increases from 10mm to 30mm. The percentage of elements with moderate damage in cracked elements drops from 59.2% to 32.8% and the percentage of elements with severe damage does not vary significantly when the rebar diameter changes from 10mm to 30mm. This also proves that the severity of cracks increases with the increase of rebar diameter.

To investigate the effect of concrete tensile strength, f_t, on crack initiation and propagation, same model as shown in Figure 5a but with different concrete tensile strengths of 1.92MPa, 2.5MPa, 3MPa, 3.5MPa and 4MPa are studied. The total number of cracked elements, as well as the number of cracked elements at the bottom or side surfaces is recorded from the FE analysis. The total number of cracked elements in the entire concrete block at the same time period (131h) with the five different tensile strengths are 32.6%, 29.1%, 27.4%, 24.1% and 23.1%, respectively. The percentage of crack elements reduces with tensile strength of concrete, indicating that crack propagates slower in high quality concrete. This is due to the reason that the f_t/E_{eff} ratio of concrete is defined to increases with the concrete strength in the FE simulations. The result is consistent with the results from analytical models which define the concrete in a similar way. Figure 2-13c shows the percentage change of d_t in cracked elements in each range with different tensile strengths. It can be shown that the percentage of elements with the most severe damage in total cracked elements increases from 32.0% to 44.8% when tensile strength increases from 1.92MPa to 4MPa. The percentage of elements with moderate damage reduces from 46.5% to 32.5% and the percentage of elements with severe

damage does not change significantly. Although with a higher tensile strength, the total number of cracked elements is smaller, the percentage of most severely damaged elements to the total cracked elements is higher, showing that crack propagates slowly with high tensile strength, but once the element cracks, the cracks are more severe. This is because concrete with a higher tensile strength is more brittle compared to the one with a lower tensile strength.

2.8 Crack patterns of non-uniform corrosion

To study the effect of non-uniform corrosion on the cracking of concrete cover, 3D FE models has been developed and described in the end of Section 2.5. The shape of the rust is assumed to be a hollow elliptic cylinder. There are four pits facing concrete cover distributed evenly along the length of the reinforcement. The extent of non-uniformness of rust expansion at the pit is determined by $\Delta r_{max}/\Delta r_{min}$, the ratio of the maximum to minimum radius increase (Equation 1). Figure 2-14 shows the crack patterns for non-uniform corrosion at the pit with the ratio of $\Delta r_{max}/\Delta r_{min}$ equal to 4, comparing to the crack patterns for uniform corrosion. Since thermal analogy is used to model rust expansion, the extent of radial expansion (i.e. diameter increase) caused by the increasing amount of corrosion products can be represented by the increase of temperature (Equation 3). The crack patterns under three different temperature increase (ΔT): 59K, 119K and 300K, are shown in Figure 2-14 to show the progress of crack propagation as rust is expanding. It can be seen that the crack pattern of the non-uniform corrosion is different from that of the uniform corrosion. Under uniform corrosion, the major crack occurs vertically in the cover. The secondary cracks that occurs later are in the direction of 135 and -135 degrees with respect to the vertical axis (Figures 2-14b, d and f). This pattern was also observed in Section 2.5 (Figure 2-4b). However, under non-uniform corrosion, the major cracks firstly form at 45 and -45 degrees with respect to the vertical axis at the location

of the pit (Figure 2-14a). The vertical crack appears later and then becomes a major crack after the two diagonal cracks (Figure 2-14c). The two cracks in the direction of 135 and -135 degrees are minor cracks compared to the three major cracks (Figure 2-14e). The FE results show that when considering non-uniform corrosion in three dimensions, the crack on the top surface is a longitudinal crack along the length of reinforcement, which is similar to the case of uniform corrosion. However, the cracks are more severe at the location of the four pits. The percentage of the crack elements to the total elements on the top surface is 9.2% for non-uniform corrosion, compared to 8.7% for uniform corrosion (Figures 2-14e and f).

The FE results for non-uniform corrosion with different extents of non-uniformness (the ratio of $\Delta r_{max}/\Delta r_{min}$ equal to 4, 8 and 32) are presented in Figures 2-15 and 2-16. Figure 2-15 shows the crack patterns under non-uniform corrosion at the pit which is 233mm away from the end with comparison to that under uniform corrosion. Figure 2-16 shows the crack patterns under non-uniform corrosion at the end which is not at the location of pits. Comparing Figures 2-15 and 2-16, it can be known that the crack patterns of non-uniform corrosion at the pits and away from the pits are very different. There are three major cracks in the cover at the pits. However, at the locations which are far away from the pits, the cracks are much less severe (Figure 2-16). There is only one major vertical crack with $\Delta r_{max}/\Delta r_{min}=32$. When $\Delta r_{max}/\Delta r_{min}=4$ and 8, only the elements in a thin layer of mesh around the steel on the side facing the cover show a sign of cracking. Comparing the crack patterns of non-uniform corrosion under the same temperature increase with different $\Delta r_{max}/\Delta r_{min}$ ratios in Figure 2-15, it can be seen that the crack pattern does not change obviously with the $\Delta r_{max}/\Delta r_{min}$ ratio. But the cracks become much more severe with a higher $\Delta r_{max}/\Delta r_{min}$ ratio. Moreover, the crack initiation time is significantly reduced when $\Delta r_{max}/\Delta r_{min}$ is greater. The crack initiates at a temperature increase

of 43.8K for the case with $\Delta r_{max}/\Delta r_{min}$=4, and initiates at a temperature increase of 23.9K when $\Delta r_{max}/\Delta r_{min}$=8. Thus the crack initiates 46% earlier when the $\Delta r_{max}/\Delta r_{min}$ ratio is doubled. With a $\Delta r_{max}/\Delta r_{min}$ ratio of 32, the crack initiates at a temperature increase of 6.0K, which is 75% earlier than the case with $\Delta r_{max}/\Delta r_{min}$=8. At crack initiation, the amount of steel mass loss, i.e. the corrosion level is decreasing when $\Delta r_{max}/\Delta r_{min}$ is higher. The percentage of steel loss required to cause cracking is 0.34%, 0.33% and 0.31% for $\Delta r_{max}/\Delta r_{min}$=4, 8, and 32, respectively. This indicates that the more concentrated non-uniform corrosion is, the earlier the cracking starts and the more dangerous the corrosion is. It should be noted that the crack initiates at a temperature increase of 41.1K for uniform corrosion, which means the concrete cracks a little earlier than the non-uniform case with $\Delta r_{max}/\Delta r_{min}$=4 (43.8K) but much later than the case with $\Delta r_{max}/\Delta r_{min}$=8 (23.9K). This is because the non-uinform corrosion is considered in three dimensions and it is assumed that there are only four pits in the longitudinal direction. The crack initiation time depends on the amount and spatial distribution of the pits. Therefore, studying non-uniform corrosion in two dimensions may not give an accurate prediction for crack initiation of concrete cover.

2.9 Conclusions

This study provides a critical and comprehensive analysis for the analytical and numerical models of corrosion-induced crack initiation of concrete cover for both uniform and non-uniform corrosion. The previous research conducted in the literature has been summarized. After carefully examining the accuracy and applicability of the existing models, recommendations have been made on how to select the proper models to estimate crack initiation time.

Parametric studies have been conducted to investigate the effect of influencing parameters on crack initiation time. It can be concluded that the influencing parameters that affect crack initiation time the most significantly from high to low are the rate of corrosion, thickness of interfacial transition zone and type of corrosion products. The results show that crack initiation time decrease with the corrosion rate but increases with the thickness of ITZ. Recent studies found that goethite, akaganeite and lepidocrocite were the main component of corrosion products. The results of parametric studies also show that concrete cover depth and rebar diameter affects crack initiation time as well. Crack initiation time increases with the c/d and s/d ratios. The FE results show that crack initiation time increases almost linearly with concrete cover depth. Increasing the cover depth is an effective approach to enhance the structural durability. Properties of concrete, such as tensile strength, elastic modulus and creep, as well as corrosion morphology also affect crack initiation time.

Three dimensional nonlinear finite element models have been developed to study crack initiation time and its influencing parameters as well as crack propagation patterns. The FE models have been validated against experimental test data. Thermal analogy has been selected to simulate the rust expansion caused by corrosion. The proposed models are able to quantify the extent of damage due to concrete cracks by using the damage plasticity model. The damage extent caused by cracking have been quantified and categorized under different case scenarios, such as cover depths from 20 to 60mm, rebar diameters from 10 to 30mm and concrete tensile strength from 1.92 to 4MPa. The percentages of cracked concrete elements with a cover depth of 20mm, 30mm, 40mm, 50mm and 60mm, are 33.8%, 32.9%, 32.0%, 30.2% and 27.4%, respectively, with the same time and rebar diameter.

Cover crack initiation and crack patterns under uniform and non-uniform corrosion are studied through developing FE models for the two types of corrosion respectively. Parametric studies have been conducted for crack propagation patterns under uniform corrosion. In the case of non-uniform corrosion, a new approach that includes multiple 3D pits distributed along the length of the steel reinforcement have been developed. The rust is assumed to be a hollow elliptic cylinder with a half elliptical shape on the side facing concrete cover and a half circular shape on the other side. Different thermal coefficients are assigned to each direction facing concrete cover at the pit. The results show the comparison of crack patterns under uniform and non-uniform corrosion. Under uniform corrosion, the major crack occurs vertically in the cover. But under non-uniform corrosion, the major cracks form at 45 and -45 degrees with respect to the vertical axis at the location of the pit. The vertical crack appears later and then becomes the third major crack.

Under non-uniform corrosion, the results also include the difference of crack patterns with different extents of non-uniformness (the ratio of $\Delta r_{max}/\Delta r_{min}$ equal to 4, 8 and 32). The results show that the crack pattern does not change very obviously with the $\Delta r_{max}/\Delta r_{min}$ ratio. But the cracks become much more severe with a higher $\Delta r_{max}/\Delta r_{min}$ ratio. Moreover, the crack initiation time is significantly reduced when $\Delta r_{max}/\Delta r_{min}$ is greater. The amount of steel mass loss to cause crack initiation is decreased when $\Delta r_{max}/\Delta r_{min}$ is higher. The highly non-inform corrosion could cause very earlier cover cracking and should be paid attention to. For non-uniform corrosion, the results show the crack patterns both at the location of the pit and away from the pit. The patterns at the pits and away from the pits can be different. Under the studied case, three major cracks are observed at the pits in the cover, but only one major vertical crack or no major cracks (depends on the $\Delta r_{max}/\Delta r_{min}$ ratio) are observed at the location that is far

away from the pits. It can be concluded that in the case of non-uniform corrosion, higher concentrated pressure is produced at the concrete-steel interface that faces the concrete cover at the pits thus would lead to earlier cracking of concrete cover. The assumption of uniform corrosion may result in unconservative estimation for the service life of RC structures particularly under chloride-induced corrosion in natural environment.

The outcome of this research offers a reliable approach to predict corrosion-induced crack initiation and propagation in concrete cover for RC structures, thus will provide infrastructure owners as well as government agencies with more reliable predictions for the service life of RC structures in corrosive environment, as well as help inspectors and engineers optimize field test plans and rehabilitation strategies for RC structures.

2.10 References

ABAQUS (2012). ABAQUS 6.12 Documentation, Dassault Systèmes Simulia Corp.

Alipour, A., and Shafei, B. (2014). Structural vulnerability measures for assessment of deteriorating bridges in seismic prone areas. *Maintenance and Safety of Aging Infrastructure*, edited by Dan Frangopol and Yiannis Tsompanakis, Chapter 3, CRC Press.

Alipour, A. (2010). Life-cycle performance assessment of highway bridges under multi-hazard conditions and environmental stressors. Ph.D. Dissertation, Department of Civil and Environmental Engineering, University of California, Irvine, CA.

Alipour, A., Shafei, B., and Shinozuka, M. (2011). Performance evaluation of deteriorating highway bridges located in high seismic areas. *Journal of Bridge Engineering*; 16(5): 597-611.

Alipour, A., Shafei, B., and Shinozuka, M. (2012). A multi-hazard framework for optimum life-cycle cost design of reinforced concrete bridges. *Structural Seismic Design Optimization and Earthquake Engineering*, Chapter 4, 76-104.

Alipour, A., Shafei, B., and Shinozuka, M. (2013). Capacity loss evaluation of reinforced concrete bridges located in extreme chloride-laden environments. *Journal of Structure and Infrastructure Engineering*; 9(1): 8-27.

Al Khalaf, M. N. and Page, C. L. (1979). Steel/mortar interfaces: Microstructural features and mode of failure. *Cement and Concrete Research*; 9(2): 197-207.

Al-Harthy, A. S., Stewart, M.G. and Mullard, J. (2011). Concrete cover cracking caused by steel reinforcement corrosion. *Magazine of Concrete Research*; 63(9): 655-667.

Alonso, C., Andrade, C., Rodriguez, J. and Diez, J. M. (1998). Factors controlling cracking of concrete affected by reinforcement corrosion. *Materials and Structures*; 31: 435-441.

American Concrete Institute Committee 318 (2011). Building Code Requirements for Structural Concrete (ACI 318-11) and Commentary.

Andrade, C., Alonso, C. and Molina, F.J. (1993). Cover cracking as a function of rebar corrosion: Part 1 - experimental test. *Materials and Structure*; 26: 453-464.

Apostolopoulos, C. A., Demis, S. and Papadakis, V. G. (2013). Chloride-induced corrosion of steel reinforcement - Mechanical performance and pit depth analysis. *Construction and Building Materials*; 38: 139-146.

Bazant, Z.P. (1979). Physical model for steel corrosion in concrete sea structures – application. *Journal of the Structural Division*; 105(6): 1155-1166.

BN EN 1992, Eurocode 2: Design of concrete structures. Part 1-1 – General rules and rules for buildings, 2004.

Cairns, J., Plizzari, G. A., Du, Y., Law, D. W., and Franzoni, C. (2005). Mechanical properties of corrosion-damaged reinforcement. *ACI Material Journal*; 102 (4): 256-264.

Canadian Standards Association (CSA) (1994). A23.3-94. Design of concrete structures. Canadian Standards Association, Rexadle, ON, Canada.

Cao, C., Cheung, Moe M. S. and Chan, B. (2013). Modeling of interaction between corrosion-induced concrete cover crack and steel corrosion rate. *Corrosion Science*; 69: 97-109.

Cao, C. and Cheung, Moe M. S. (2014). Non-uniform rust expansion for chloride-induced pitting corrosion in RC structures. *Construction and Building Materials*; 51: 75-81.

Cao, C. (2014). 3D simulation of localized steel corrosion in chloride contaminated reinforced concrete. *Construction and Building Materials*; 72: 434-443.

Chen, D. and Mahadevan, S. (2008). Chloride-induced reinforcement corrosion and concrete cracking simulation. *Cement and Concrete Composites*; 30(3): 227-238.

Chen, E. and Leung, C. (2013). Numerical modelling of non-uniform steel corrosion development and its mechanical influences on reinforced concrete structures. *In Proceeding of VIII International Conference on Fracture Mechanics of Concrete and Concrete Structures*, FraMCos-8.

Chen, E. and Leung, C. (2015). Finite element modeling of concrete cover cracking due to non-uniform steel corrosion. *Engineering Fracture Mechanics*; 134: 61-78.

Chernin, L. and Val, D.V. (2011). Prediction of corrosion-induced cover cracking in reinforced concrete structures. *Construction and Building Materials*; 25(4): 1854-1869.

Chernin, L., Val, D.V. and Volokh K.Y. (2010). Analytical modelling of concrete cover cracking caused by corrosion of reinforcement. *Journal of Materials and Structures*; 43(4):543-556.

Codaro, E. N., Nakazato, R. Z., Horovistiz, A. L., Ribeiro, L. M. F., Ribeiro, R.B. and Hein, L.R.O. (2002). An image processing method for morphology characterization and pitting corrosion evaluation. *Materials Science and Engineering: A*; 334(1-2): 298-306.

Coronelli, D., Hanjari, K. Z. and Lundgren, K. (2013). Severely corroded RC with cover cracking. *Journal of Structural Engineering*; 139(2): 221-232.

Cui, Z., and Alipour, A. (2014). A detailed finite-element approach for performance assessment of corroded reinforced concrete beams. *ASCE Structures Congress*, Boston, Massachusetts, April 3-5.

Dagher, H.J. and Kulendran, S. (1992). Finite element modeling of corrosion damage in concrete structures. *ACI Structural Journal*; 89(6):699-708.

Dong, W., Murakami, Y., Oshita, H., Suzuki, S. and Tsutsumi, T. (2011). Influence of bond stirrup spacing and anchorage performance on residual strength of corroded RC beams. *Journal of Advanced Concrete Technology*; 9(3):261-275.

Du, Y. G., Chan A.H.C., Clark, L.A., Wang, X.T., Gurkalo, F. and Bartos, S. (2013). Finite element analysis of cracking and delamination of concrete beam due to steel corrosion. *Engineering Structures*; 56: 8-21.

Du, Y.G., Chan, A.H.C and Clark, L.A. (2006). Finite element analysis of the effects of radial expansion of corroded reinforcement. *Computers and Structures*; 84(13-14): 917-929.

Du, X. L., Jin, Liu and Zhang, R. B. (2014). Modeling the cracking of cover concrete due to non-uniform corrosion of reinforcement. *Corrosion Science*; 89: 189-202.

El Maaddawy, T., Soudki, K. and Topper, T. (2005). Long-term performance of corrosion-damaged reinforced concrete beams. *ACI Structural Journal*; 102(5): 649-656.

El Maaddawy, T. and Soudki, K. (2007). A model for prediction of time from corrosion initiation to corrosion cracking. *Journal of Cement and Concrete Composites*; 29(3): 168-175.

Hanjari, K. Z., Kettil, P. and Lundgren, K. (2011). Analysis of mechanical behavior of corroded reinforced concrete structures. *ACI Structural Journal*; 108(5): 532-541.

Hanjari, K. Z., Lundgren, K., Plos, M. and Coronelli, D. (2013). Three-dimensional modelling of structural effects of corroding steel reinforcement in concrete. *Structure and Infrastructure Engineering*; 9(7): 702-718.

Hingorani, R., Perez, F., Sanchez, J., Fullea, J., Andrade, C. and Tanner, P. (2013). Loss of ductility and strength of reinforcing steel due to pitting corrosion. *In Proceedings of*

VIII International Conference on Fracture Mechanics of Concrete and Concrete Structures, FraMCos-8.

Jamali, A., Angst, U., Adey, B. and Elsener B. (2013). Modeling of corrosion-induced concrete cover cracking: A critical analysis. *Construction and Building Materials*; 42: 225-237.

Jang, B. S. and Oh, B. H (2010). Effects of non-uniform corrosion on the cracking and service life of reinforced concrete structures. *Cement and concrete research*; 40(9): 1441-1450.

Kashani, M. M., Crewe, A. J. and Alexander, N. A. (2013). Use of a 3D optical measurement technique for stochastic corrosion pattern analysis of reinforcing bars subjected to accelerated corrosion. *Corrosion Science*; *73*: 208-221.

Kashani, M. M., Lowes, L. N., Crewe, A. J. and Alexander, N. A. (2016a). A multi-mechanical nonlinear fibre beam-column model for corroded columns. *International Journal of Structural Integrity*; 7(2): 213-226.

Kashani, M. M., Crewe, A. J. and Alexander, N. A. (2016b). Structural capacity assessment of corroded RC bridge piers. *In Proceedings of the Institution of Civil Engineers-Bridge Engineering*, 1-14.

Li., C., Melchers, R. E. and Zheng, J. (2006). Analytical model for corrosion-induced crack width in reinforced concrete structures. *ACI Structural Journal*; 103(4): 479-487.

Li, F., Qu, Y., Zhao, Y. and Lu, R. (2014). Numerical Simulation Method for Fracture Effect of Corroded Steel Strand under Tension. *In Proceeding of 4th International Conference on the Durability of Concrete Structures*, Purdue University, West Lafayette, IN, USA.

Liu, Y and Weyers, R.E. (1998). Modeling the Time-to-Corrosion Cracking in Chloride Contaminated Reinforced Concrete Structures. *ACI Materials Journal*; 95(6): 675-681.

Lu, C., Jin, W. and Liu R. (2011). Reinforcement corrosion-induced cover cracking and its time prediction for reinforced concrete structures. *Journal of Corrosion Science*; 53(4): 1337-1347.

Malumbela, G., Alexander, M. and Moyo, P. (2011). Model for cover cracking of RC beams due to partial surface steel corrosion. *Journal of Construction and Building Materials*; 25(2): 987-991.

Mangat, P. S. and Elgarf, M. S. (1999). Bond characteristics of corroding reinforcement in concrete beams. *Materials and Structures*; 32: 89-97.

Marcotte, T. D. and Hansson, C. M. (2007). Corrosion products that form on steel within cement paste. *Material Structures*; 40: 325-340.

Michel, A, Pease, B. J., Geiker, M. R., Stang, H. and Olesen, J. F. (2011). Monitoring reinforcement corrosion and corrosion-induced cracking using non-destructive X-ray attenuation measurements. *Cement Concrete Research*; 41(11): 1085-1094.

Michel, A., Pease, B. J., Peterová, A., Geiker, M. R., Stang, H. and Thybo, A. E. A. (2014). Penetration of corrosion products and corrosion-induced cracking in reinforced cementitious materials: Experimental investigations and numerical simulations. *Cement and Concrete Composites*; 47: 75-86.

Michel, A., Otieno, M., Stang, H. and Geiker, M. R. (2016). Propagation of steel corrosion in concrete: Experimental and numerical investigations. *Cement and Concrete Composites*; 70: 171-182.

Molina, F.J., Alonso, C. and Andrade, C. (1993). Cover cracking as a function of rebar corrosion: Part 2 - numerical model. *Materials and Structures*; 26: 532-548.

Moreno, J., Bonilla, M., Adam, J., Borrachero, M. and Soriano, L. (2015). Determining corrosion levels in the reinforcement rebars of buildings in coastal areas. A case study in the Mediterranean coastline. *Construction and Building Materials*; 100: 11-21.

Morinaga, S (1988). Prediction of service lives of reinforced concrete buildings based on rate of corrosion of reinforcing steel. Shimizu Corp.

Mullard, J. and Stewart, M. (2011). Corrosion-induced cover cracking: new test data and predictive models. *ACI Structural Journal*; 108(1): 71-79.

Ni Choine, M., Kashani, M. M., Lowes, L. N., O'Connor, A., Crewe, A. J., Alexander, N. A. and Padgett, J. E. (2016). Nonlinear dynamic analysis and seismic fragility assessment of a corrosion damaged integral bridge. *International Journal of Structural Integrity*; 7(2): 227-239.

Nilson, A. H., Darwin, D. and Dolan, C. W. (2004). Design of concrete structures, 13th Edition. McGraw-Hill, New York, NY.

Ožbolt, J., Oršanić, F., Balabanić, G. and Kušter, M. (2012). Modeling damage in concrete caused by corrosion of reinforcement: coupled 3D FE model. *International Journal of Fracture*; 178(1-2): 233-244.

Pantazopoulou, S. J. and Papoulia, K. D. (2001). Modeling cover-cracking due to reinforcement corrosion in RC structures. *Journal of Engineering Mechanics*; 127(4): 342-351.

Petre-Lazar, I. and Gérard, B. (2000). Mechanical behaviour of corrosion products formed at the steel - concrete interface: Testing and modelling. Proceedings of EM 2000, Fourteenth engineering Mechanics Conference, ASCE, Austion, Texas, USA.

Rao, A. S., Lepech, M. D., and Kiremidjian, A. (2017a). Development of time-dependent fragility functions for deteriorating reinforced concrete bridge piers. *Structure and Infrastructure Engineering*; 13(1): 67-83.

Rao, A. S., Lepech, M. D., Kiremidjian, A. S. and Sun, X. Y. (2017b). Simplified structural deterioration model for reinforced concrete bridge piers under cyclic loading. *Structure and Infrastructure Engineering*; 13(1): 55-66.

Reale, T. and O'Connor, A. (2012). A review and comparative analysis of corrosion-induced time to first crack models. *Journal of Construction and Building Materials*; 36: 475-483.

Rodriguez, J., Ortega, L. M., Casal, J. and Diez, J. M. (1996). Corrosion of reinforcement and service life of concrete structures. *In Proceedings of the 7th international conference on durability of building materials and components 7 (Volume One)*. Stockholm, Sweden: E & FN Spon, 117-126.

Šavija, B., Lukovic, M., Pacheco, J. and Schlangen, E. (2013). Cracking of the concrete cover due to reinforcement corrosion: A two-dimensional lattice model study. *Construction and Building Materials*; 44: 626-638.

Shafei, B., Alipour, A., and Shinozuka, M. (2012). Prediction of corrosion initiation in reinforced concrete members subjected to environmental stressors: A finite-element framework. *Journal of Cement and Concrete Research*; 42(2): 365-376.

Shafei, B., Alipour, A., and Shinozuka, M. (2013). A stochastic computational framework to investigate the initial stage of corrosion in reinforced concrete superstructures. *Journal of Computer-Aided Civil and Infrastructure Engineering*; 28(7): 482-494.

Shafei, B., and Alipour, A. (2015a). Application of large-scale non-Gaussian stochastic fields for the study of corrosion-induced structural deterioration. *Journal of Engineering Structures*; 88: 262-276.

Shafei, B., and Alipour, A. (2015b). Estimation of corrosion initiation time in reinforced concrete bridge columns: how to incorporate spatial and temporal uncertainties. *Journal of Engineering Mechanics*.

Toongoenthong, K. and Maekawa, K. (2005). Simulation of coupled corrosive product formation, migration into crack and propagation in reinforced concrete sections. *Journal of Advanced Concrete Technology*; 3(2): 253-265.

Torres-Acosta, A. A. and Sagues, A. A. (2004). Concrete cracking by localized steel corrosion geometric effects. *ACI Materials Journal*; 101(6): 501-507.

Val, D. V. and Chernin, L. (2009). Serviceability Reliability of Reinforced Concrete Beams with Corroded Reinforcement. *Journal of Structural Engineering*; 135(8): 896-905.

Val, D. V., Chernin, L. and Stewart, M. G. (2009). Experimental and Numerical Investigation of Corrosion-Induced Cover Cracking in Reinforced Concrete Structures. *Journal of Structural Engineering*; 135(4): 376-385.

Vu, K., Stewart, M. G. and Mullard, J. (2005). Corrosion-induced cracking: experimental data and predictive models. *ACI Structural Journal*; 102(5): 719-726.

Washington State Bridge Inspection Manual (2015). Bridge preservation office, Washington State Department of Transportation, Washington.

Williamson, S. J. and Clark, L. A. (2000). Pressure required to cause cover cracking of concrete due to reinforcement corrosion. *Magazine of Concrete Research*; 52(6): 455-467.

Wong, H. S., Zhao, Y. X., Karimi, A. R., Buenfeld, N.R. and Jin, W. L. (2010). On the penetration of corrosion products from reinforcing steel into concrete due to chloride-induced corrosion. *Journal of Corrosion Science*; 52(7): 2469-2480.

Xia, N., Ren, Q., Liang, R., Payer, J. and Patnaik, A. (2012). Nonuniform corrosion-induced stresses in steel-reinforced concrete. *Journal of Engineering Mechanics*; 138(4): 338-346.

Xu, Y. D. and Qian, C. X. (2013). Influence of coupled chemo-mechanical process on corrosion characteristics in reinforcing bars. *Journal of Wuhan University of Technology*, Materials Science Edition; 28(3): 538-543.

Yokozeki, K., Motohashi, K., Okada, K. and Tsutsumi, T. (1997). A rational model to predict the service life of RC structures in marine environment. *ACI International Concrete Abstracts Portal, Special Publication*; 170: 777-799.

Yuan, Y.S. and Ji, Y.S. (2009). Modeling corroded section configuration of steel bar in concrete structure. *Construction and Building Materials*; 23(2009): 2461-2466.

Zhang, R. J., Castel, A. and François, R. (2010). Concrete cover cracking with reinforcement corrosion of RC beam during chloride-induced corrosion process. *Cement and Concrete Research*; 40(3): 415-425.

Zhang, X. G., Wang, X. Z., Lu, Z. H. and Xing, F. (2011). Analytical model of non-uniform corrosion induced cracking of reinforced concrete structures. *Journal of Central South University of Technology*; 18: 940-945.

Zhou, K., Martin-Perez, B. and Lounis, Z. (2005). Finite element analysis of corrosion-induced cracking, spalling and delamination of RC bridge decks. *In Proceedings of the 1st Canadian conference on effective design of structures*. Hamilton, Ontario; 187-196.

Table 2-1. Comparison of predicted and experimental results for time to cracking

Reference test	Observed time (h)	i_{corr} (μA/cm^2)	Liu and Weyers (1998)		EI Maaddawy and Soudki (2005)		Lu et al. (2011)	
			Predicted time (h)	T_{model}/T_{test}	Predicted time (h)	T_{model}/T_{test}	Predicted time (h)	T_{model}/T_{test}
Andrade et al. (1993)	96	100	112.9	1.18	96.8	1.01	95.0	0.99
Lu et al. (2011)	147.5	100	253.2	1.72	145.8	0.99	*161.4*	1.09
	87	150	168.8	1.94	97.2	1.12	*107.6*	1.24
	112	100	188.8	1.69	125.9	1.12	*138.8*	1.24
EI Maaddawy and Soudki (2005)	95	150	109.9	1.16	*78.0*	0.82	77.0	0.81
Liu and Weyers (1998)	1.84yrs	2.35	*0.84yrs*	0.46	0.58yrs	0.32	1.33yrs	0.73
	3.54yrs	1.79	*1.72yrs*	0.49	0.95yrs	0.27	2.63yrs	0.74
	0.72yrs	3.75	*0.29yrs*	0.40	0.27yrs	0.38	0.47yrs	0.66
Vu et al. (2005)	134	100	112.2	0.84	96.5	0.72	98.2	0.73
	194.7	100	210.6	1.08	132.2	0.68	139.4	0.72
	116	100	105.3	0.91	93.5	0.81	96.6	0.83
	155.7	100	193.1	1.24	126.6	0.81	136.1	0.87
	136.1	100	101.5	0.75	91.8	0.67	95.7	0.70

Table 2-2. Summary of numerical models

Reference	Molina et al. (1993)	Yokozeki et al. (1997)	Zhou et al. (2005)	Toongoenthong and Maekawa (2005)	Chen and Mahadevan (2013)	Val et al. (2009)
Dimensionality	2D	2D	2D	2D	3D	2D
No. of rebars	Single	Multiple	Two	Multiple	Single	Multiple
Poisson's ratio of rust	ν_r=0.5	ν_r =0.3	Rust not simulated	Steel and rust as one expansive material	Rust not simulated	Rust not simulated
Elastic modulus of rust	E_r=3(1-2ν_r)K_r, K_r=2GPa	E_r =250MPa	Rust not simulated	Steel and rust as one expansive material	Rust not simulated	Rust not simulated
Concrete model	Smeared fixed crack model with linear softening	Smeared crack model, tension softening based on Model Code 1990	Damaged plasticity model	Smeared crack model with nonlinear tension softening	Smeared crack model	Fixed orthogonal crack model
Elements for concrete	Eight node plane strain element	-	Eight node isoparametric element	Plain strain element	Solid65 – eight nodes with three DOFs at each node	Four node bilinear plain strain quadrilateral element with reduced integration and hourglass control
Rust modeling approach	Thermal load	-	Radial displacement	Steel and rust as one compatible growing material	Radial displacement	Thermal analogy
Rust penetrating into concrete cracks	No	No	No	Yes	No	No
Validation	Quantitative comparison with experimental tests	Quantitative comparison with experimental tests in the literature	No	Yes	No	Only qualitatively

Table 2-3. Properties of iron and major corrosion products

Corrosion products	Composition	Molecular weight ratio γ	Volumetric ratio λ
Iron	Fe	1	1
Geothite	α-FeOOH	0.629	2.91
Akaganeite	β-FeOOH	0.629	3.48
Lepidocrocite	γ-FeOOH	0.629	3.03
Iron oxide	FeO	0.778	1.70
Hematite	$1/2Fe_2O_3$	0.350	2.00
Magnetite	$1/3Fe_3O_4$	0.241	2.10
Ferrous hydroxide	$Fe(OH)_2$	0.622	3.60
Ferric hydroxide	$Fe(OH)_3$	0.523	4.00
Hydrated ferric oxide	$Fe(OH)_3 \cdot 3H_2O$	0.348	6.15

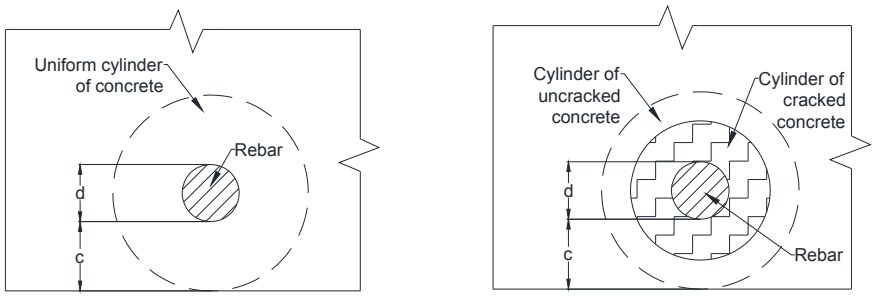

(a) (b)

Figure 2-1. The two analytical models of corrosion-induced cracking (a) TWUC; (b) TWDC

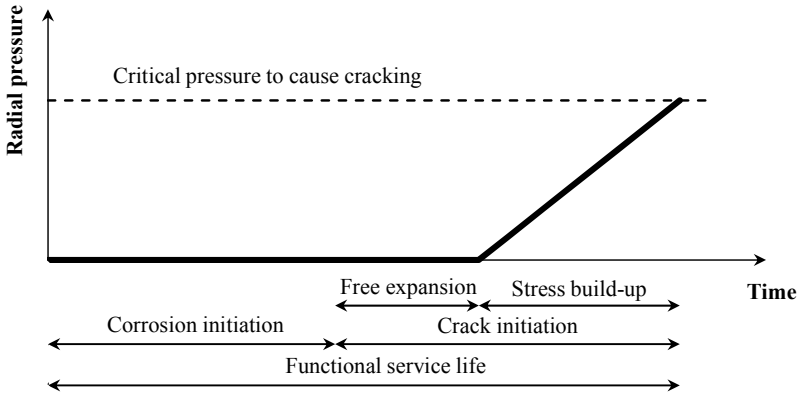

Figure 2-2. Different stages of the corrosion process

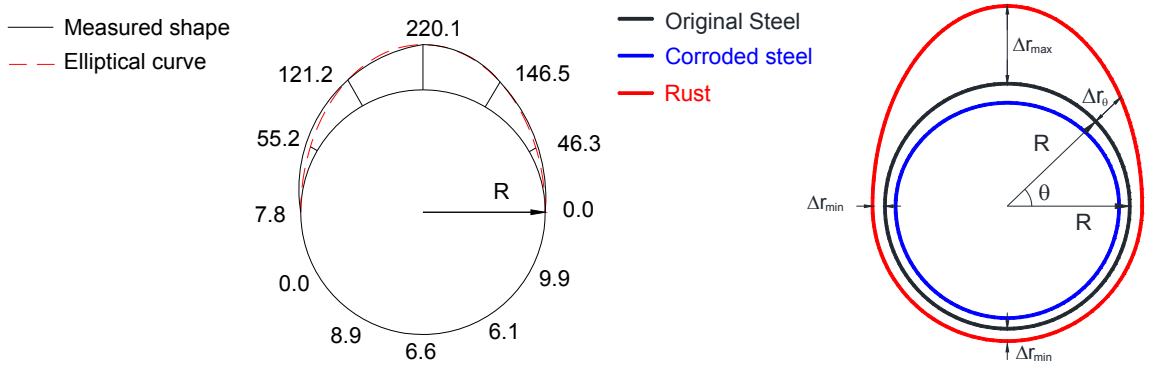

Figure 2-3. (a) Distribution of corrosion products in pitting conditions (Yuan and Ji 2009);

(b) Developed elliptical model for rust distribution

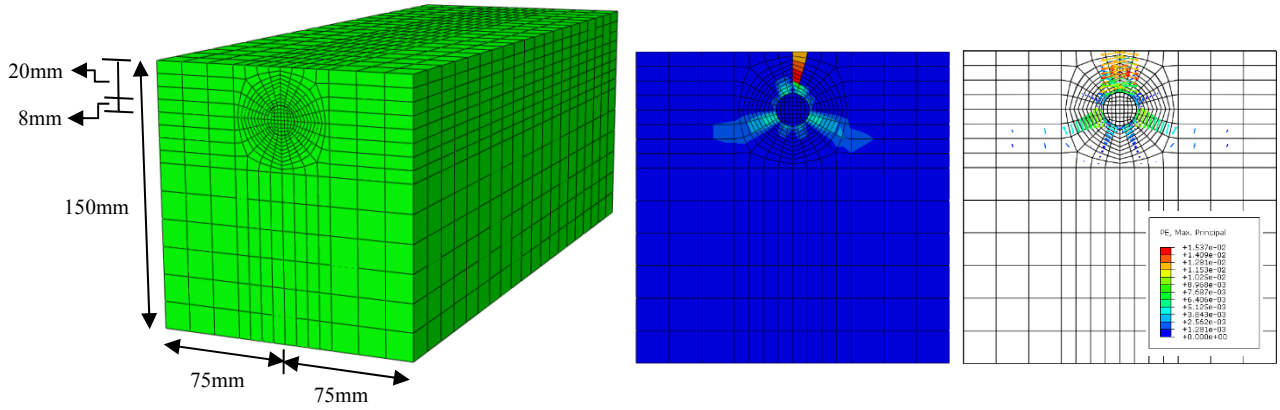

(a) (b)

Figure 2-4. (a) The FE model and (b) Crack patterns of the cross section in terms of maximal principle strains (contour and arrow view)

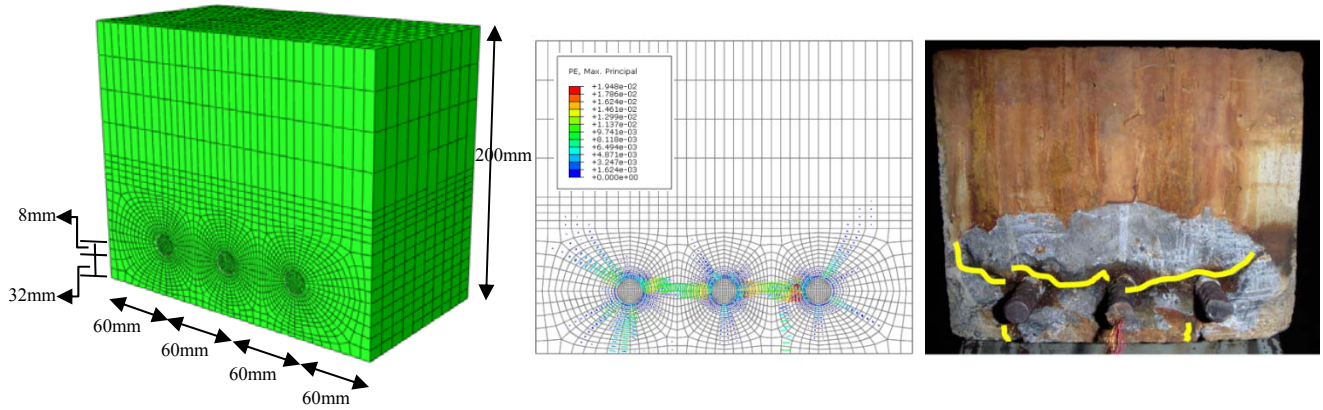

(a) (b) (c)

Figure 2-5. (a) The FE model; (b) Crack pattern of FE model; (c) Crack pattern of test specimen

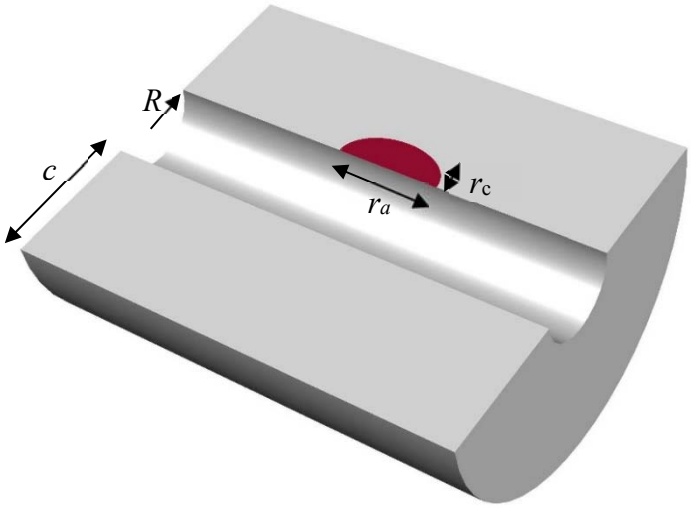

c: concrete cover depth
R: original radius of the steel bar
r_a: length of rust expansion
r_c: depth of rust expansion

Figure 2-6. Three dimensional non-uniform corrosion and rust expansion

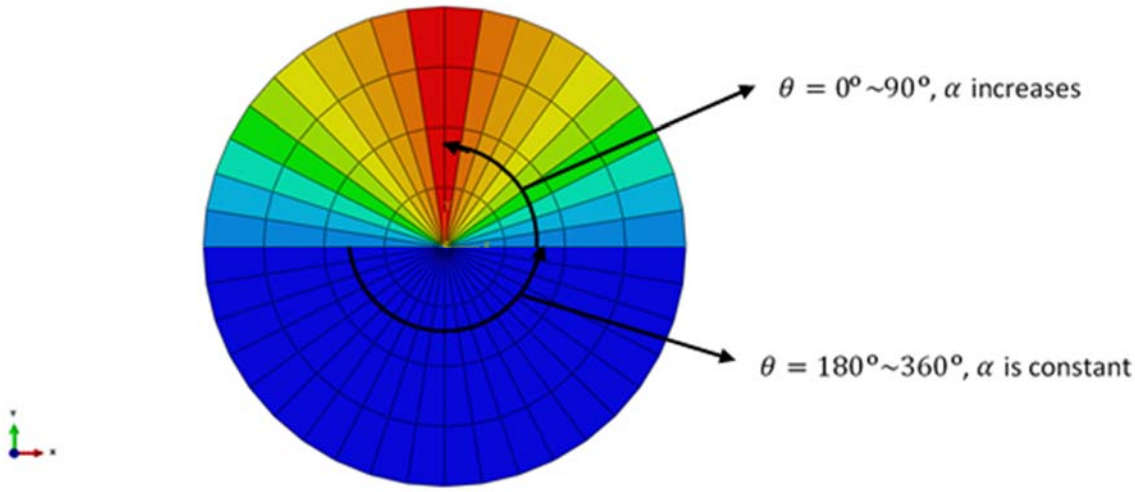

Figure 2-7. The distribution of radial thermal coefficients

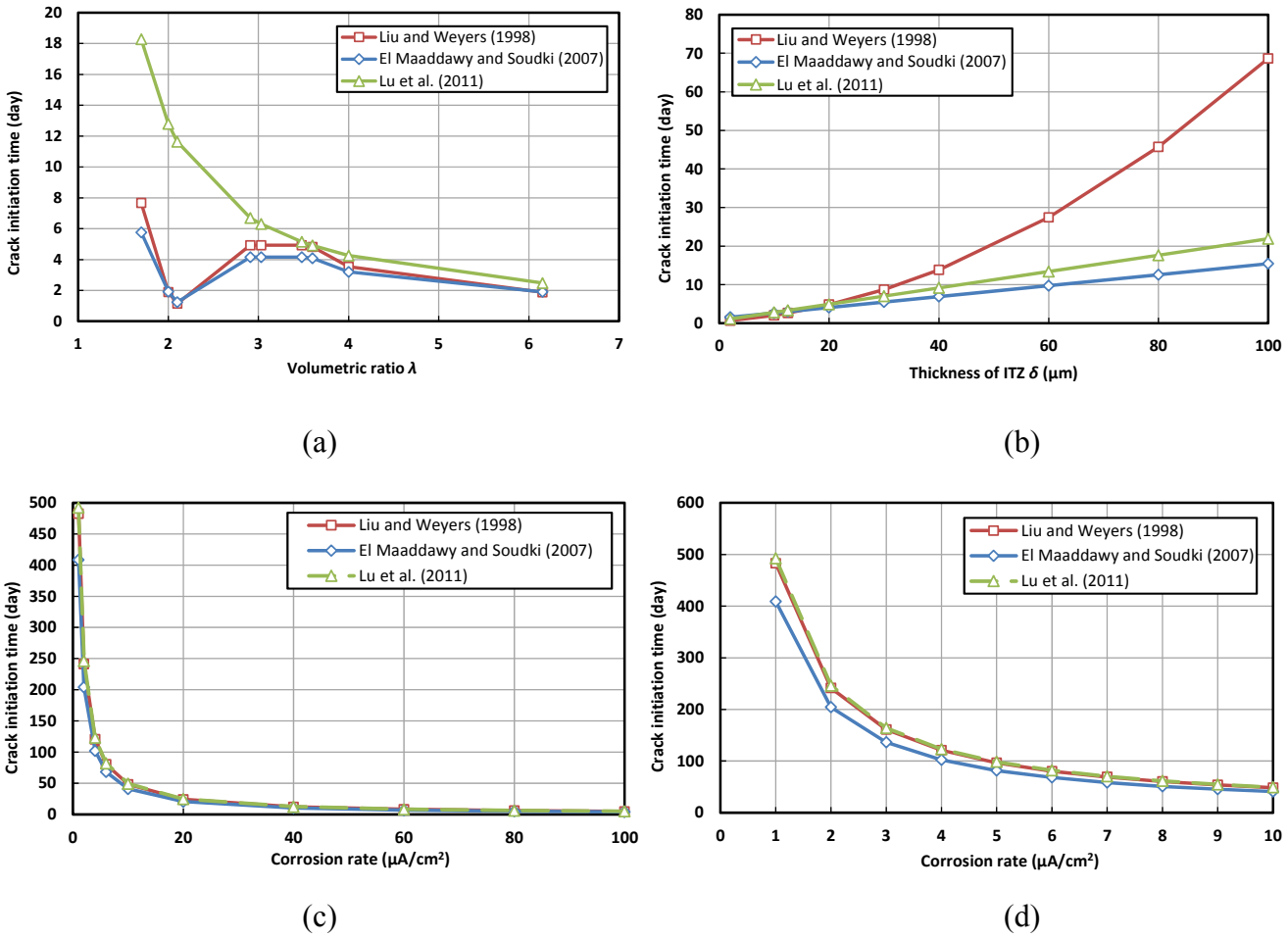

Figure 2-8. Effect of influencing parameters on crack initiation time: (a) type of corrosion product; (b) thickness of ITZ; (c) corrosion rate up to 100μA/cm^2; (d) long-term corrosion

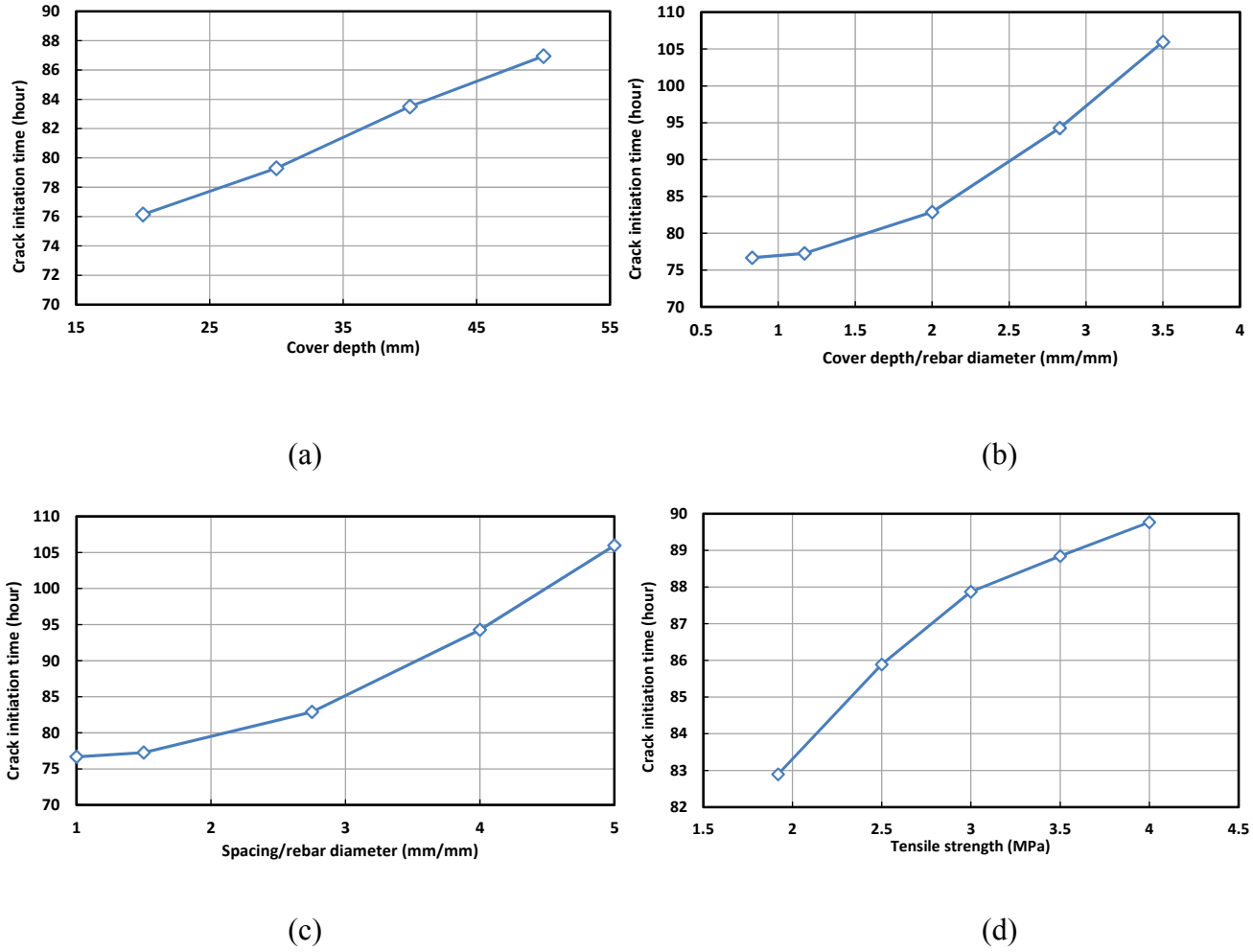

Figure 2-9. Effect of influencing parameters on crack initiation time: (a) cover depth; (b) *c*/*d*; (c) *s*/*d*; (d) tensile strength of concrete

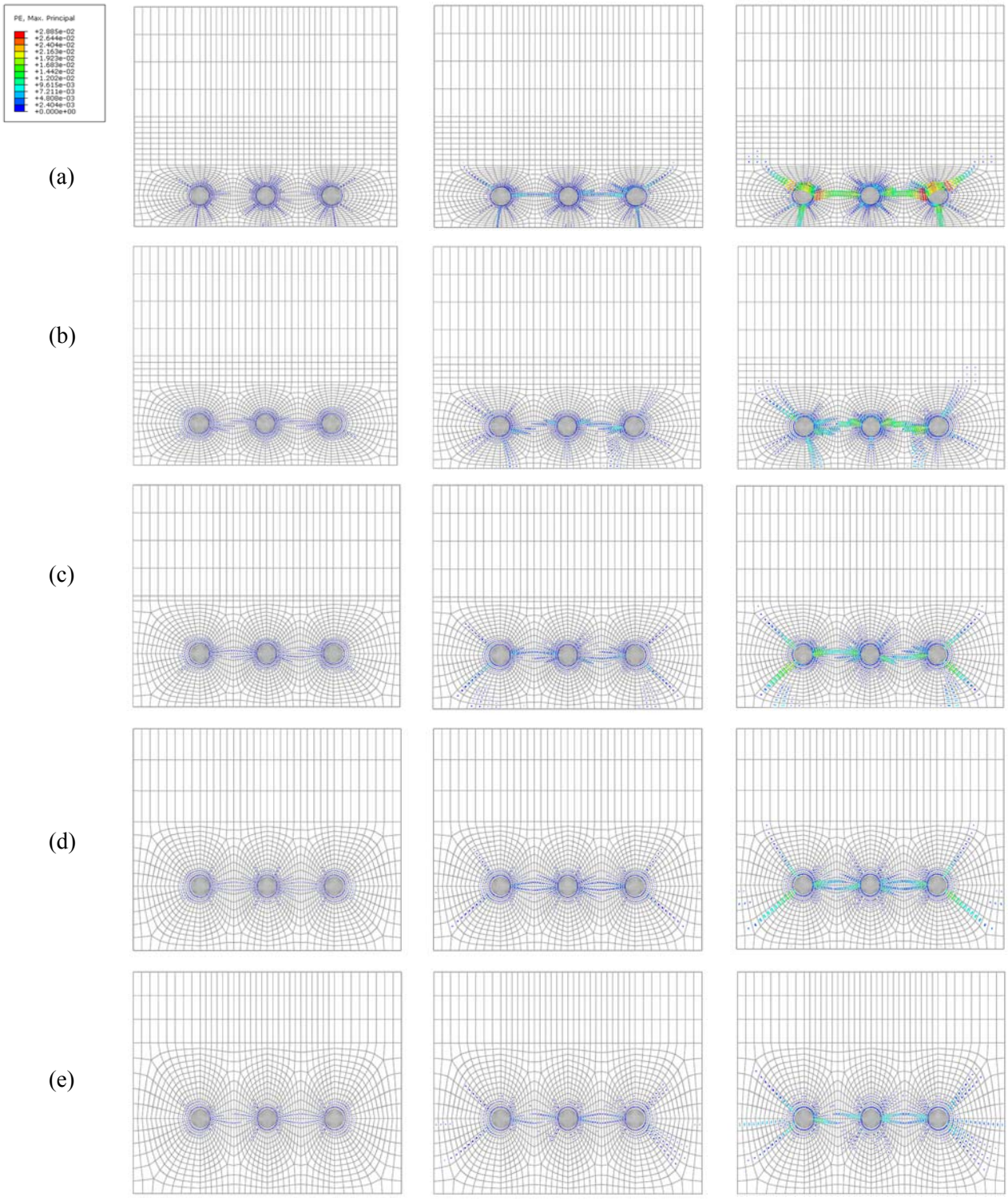

Figure 2-10. Crack propagation patterns for different cover depths: (a) 20mm; (b) 30mm; (c) 40mm; (d) 50mm; (e) 60mm at bottom (d=16mm, s=60mm, s_{cl}=22mm, f_t=1.92MPa)

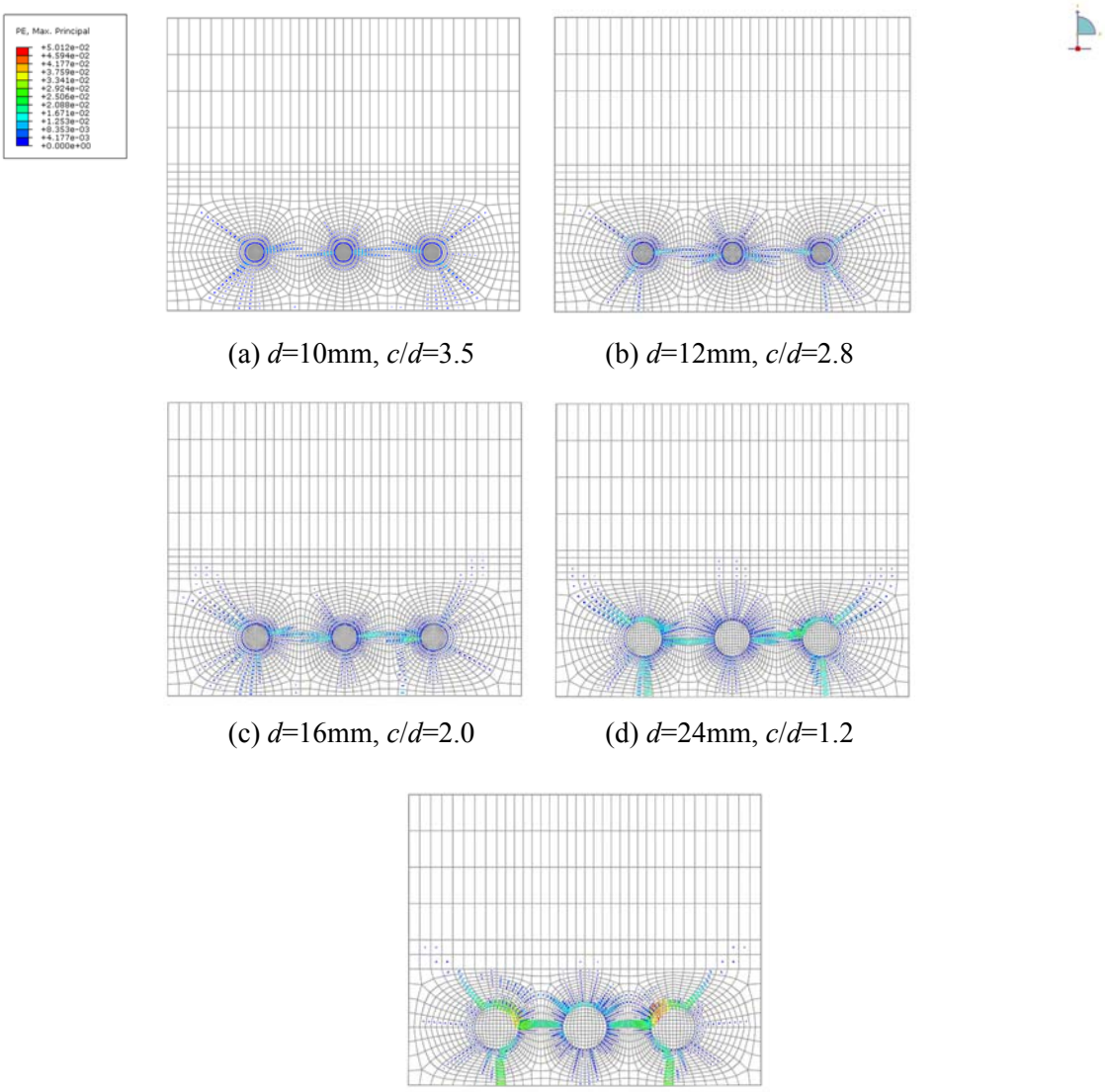

(a) d=10mm, c/d=3.5 (b) d=12mm, c/d=2.8

(c) d=16mm, c/d=2.0 (d) d=24mm, c/d=1.2

(e) d=30mm, c/d=0.8

Figure 2-11. Crack propagation patterns for different cover depth to bar diameter ratios (f_t=1.92MPa, t=131h)

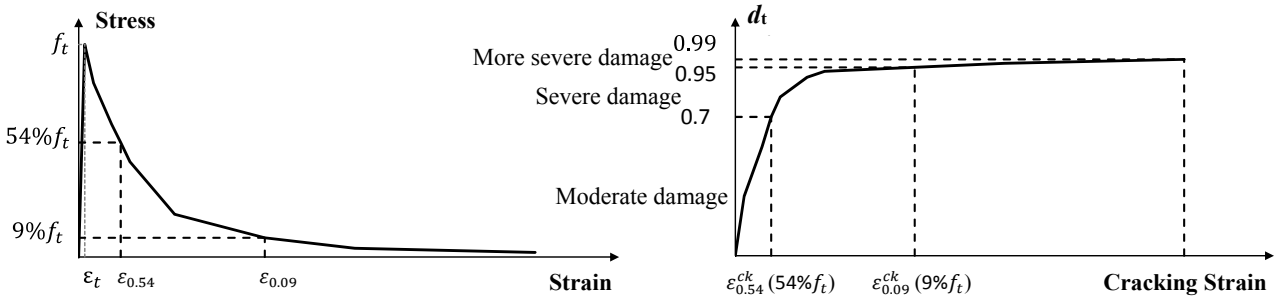

(a) (b)

Figure 2-12. (a) Stress-strain curve of concrete in tension; (b) Relationship between cracking strain and tensile damage in concrete

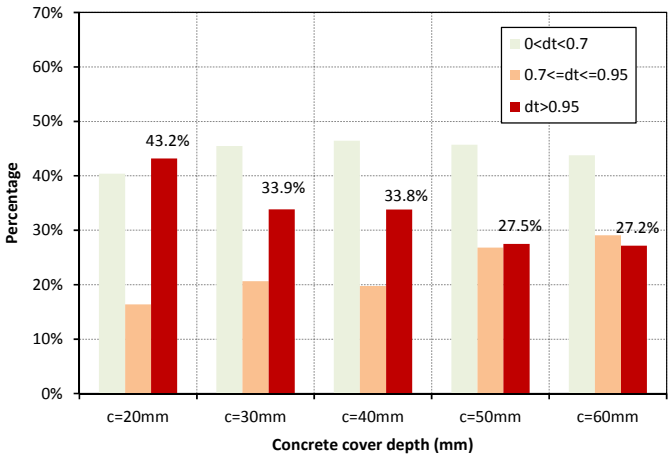

(a)

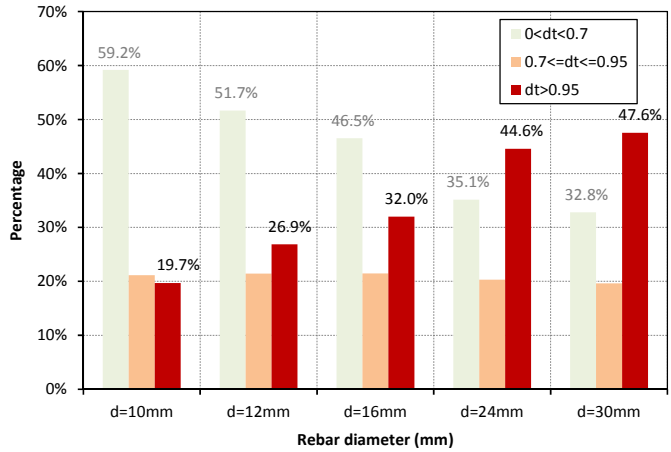

(b)

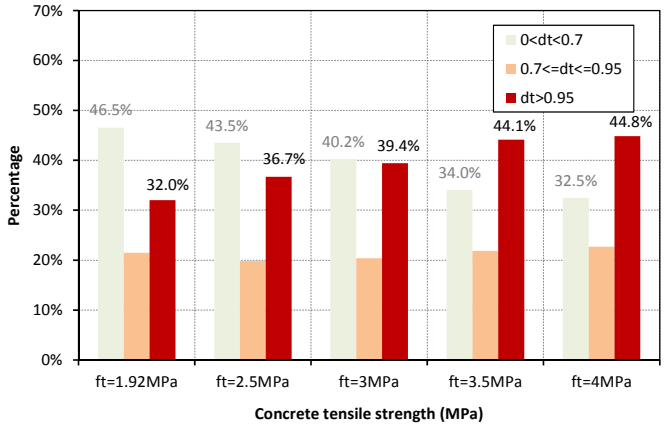

(c)

Figure 2-13. Variation of tensile damage extent in cracked concrete elements with (a) different cover depths; (b) different rebar diameter; (c) different concrete tensile strength

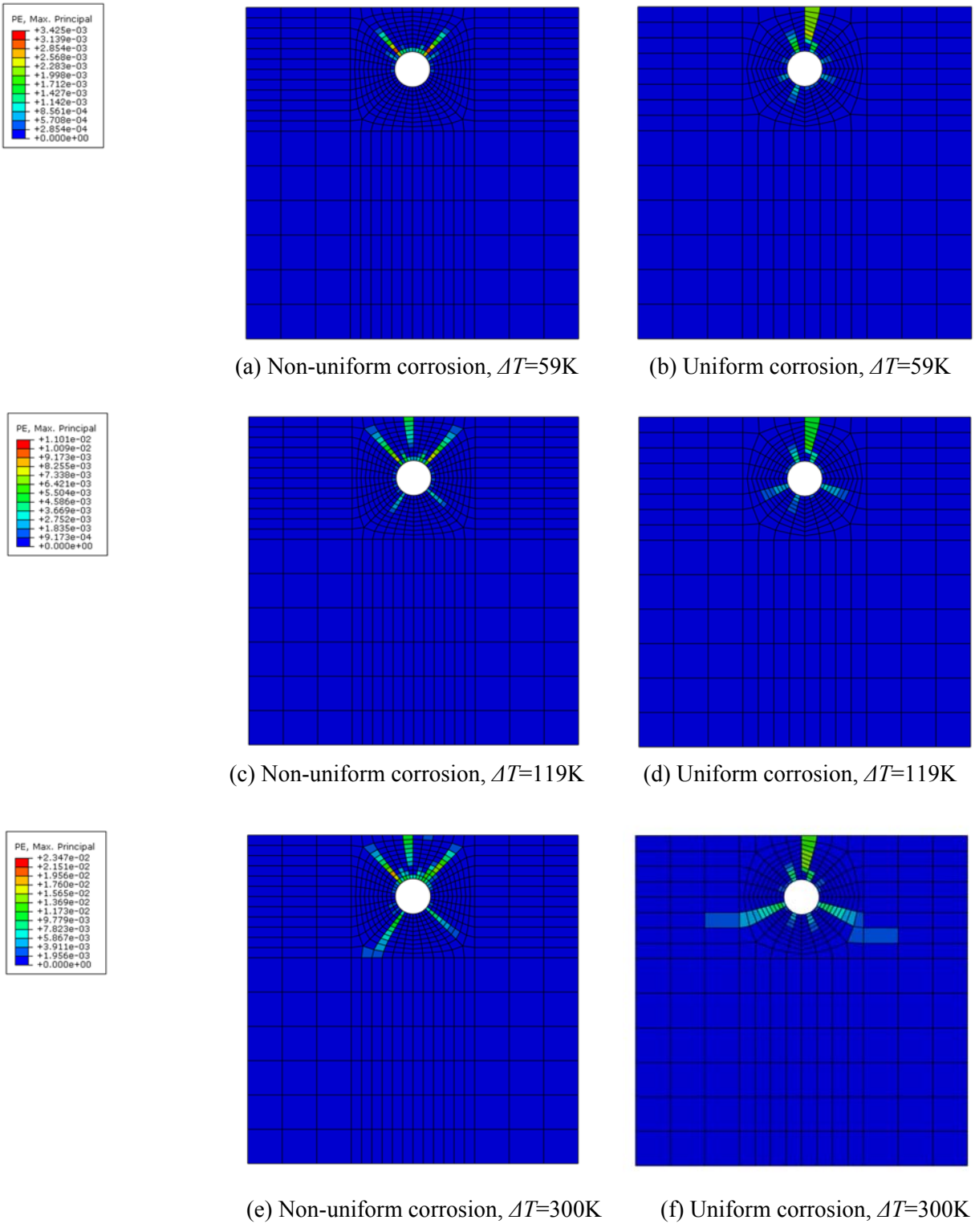

(a) Non-uniform corrosion, ΔT=59K (b) Uniform corrosion, ΔT=59K

(c) Non-uniform corrosion, ΔT=119K (d) Uniform corrosion, ΔT=119K

(e) Non-uniform corrosion, ΔT=300K (f) Uniform corrosion, ΔT=300K

Figure 2-14. Crack patterns for non-uniform and uniform corrosion

(Non-uniform corrosion: Δrmax/Δrmin=4, at the pit which is 233mm from the end)

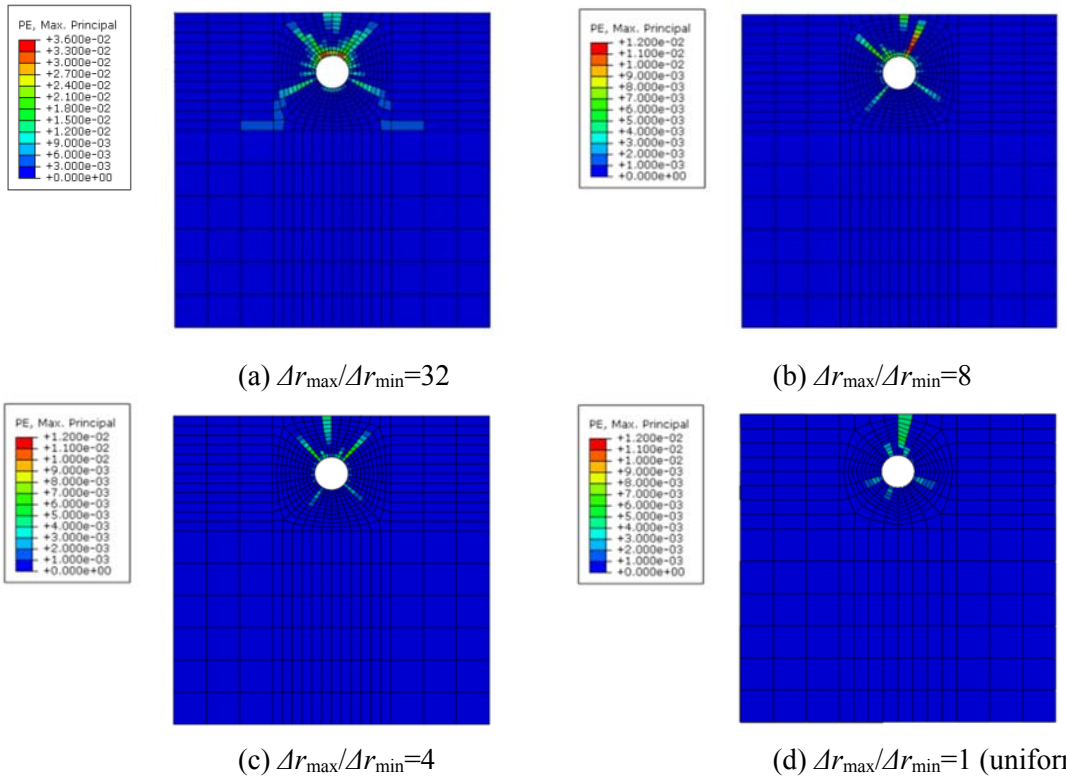

(a) $\Delta r_{max}/\Delta r_{min}$=32 (b) $\Delta r_{max}/\Delta r_{min}$=8

(c) $\Delta r_{max}/\Delta r_{min}$=4 (d) $\Delta r_{max}/\Delta r_{min}$=1 (uniform)

Figure 2-15. Crack patterns of non-uniform and uniform corrosion

(Non-uniform corrosion: at the pit which is 233mm from the end)

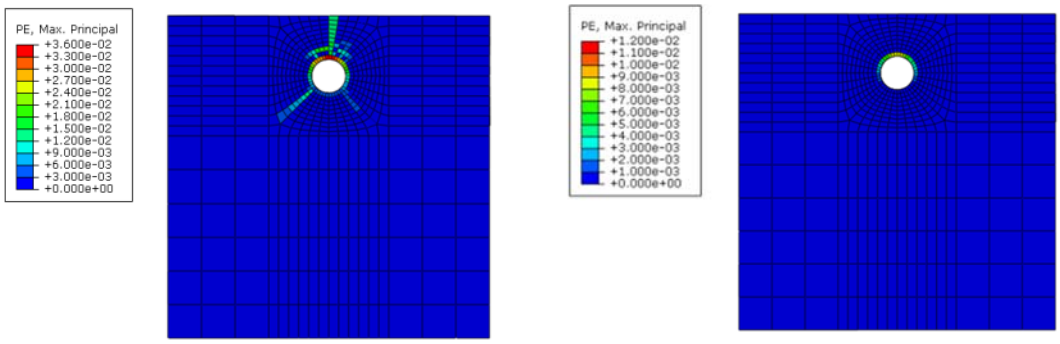

(a) $\Delta r_{max}/\Delta r_{min}$=32 (b) $\Delta r_{max}/\Delta r_{min}$=8

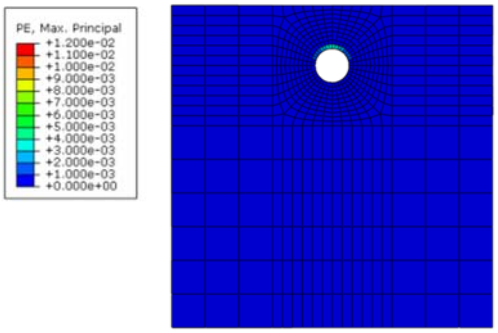

(c) $\Delta r_{max}/\Delta r_{min}$=4

Figure 2-16. Crack patterns of non-uniform corrosion

(at the end, not at the location of pits)

CHAPTER 3. A DETAILED FINITE ELEMENT APPROACH FOR PERFORMANCE ASSESSMENT OF CORRODED REINFORCED CONCRETE BEAMS

Modified from a paper published in the proceedings of *The ASCE Structures Congress 2014*, Boston, Massachusetts.

Zhen Cui, Alice Alipour

3.1 Abstract

Structural behavior of reinforced concrete beams with corroded reinforcement is studied in this paper. The degrading effects of corrosion on the structural response of reinforced concrete beams has been simulated considering factors such as the reduction of cross sectional area of steel, change in steel and concrete material properties and bond deterioration. A three dimensional finite element model, which is capable of considering the nonlinearity in material and geometric properties, is proposed to investigate the structural performance of reinforced concrete beams with different reinforcement ratios and arrangements under varying corrosion levels. Nonlinear relationship for the bond-slip deterioration as a function of corrosion level has been developed and implemented into the finite element model. At the final stage, the results have been verified with the available experimental data.

3.2 Introduction

Different mechanisms such as chloride intrusion, carbonation, or sulfate attack can result in corrosion initiation in steel reinforcement. In coastal regions or those areas with harsh winters and high exposure to deicing salts, the chloride induced corrosion is one of the major causes of deterioration of reinforced concrete structures. The deterioration mechanism can be divided into two major phases: a) corrosion initiation and b) corrosion propagation. At the corrosion

initiation level, the chloride ions diffuse into the concrete through the pores and micro cracks. As the chloride content in the vicinity of the rebars reaches a critical level, the protective film around the rebar is depassivated and the corrosion starts. During the corrosion process the cross sectional area of the steel is reduced to produce the corrosion products. Since the volume of rust produced in the corrosion process is larger than that of steel used in the process internal pressure is applied to the surrounding concrete which results in concrete cracking, spalling, and de-bonding (Val and Chernin 2009, Alipour et al. 2010, and Shafei and Alipour 2013). Extensive research has been conducted to estimate the corrosion initiation time (Shafei et al. 2012 and 2013), and the concrete cracking due to corrosion (Pantazopoulou and Papoulia 2001, El Maadaway and Soudki 2007, Shafei and Alipour 2012, and Alipour et al. 2011 and 2013). However not many studies have included the effect of bond loss. According to EI Maaddawy et al. (2003), most of the research on the effect of corrosion on bond strength is based on experimental studies. The studies on the effect of corrosion on structural capacity of the beams (Rodriguez et al. 1996 and 1997) and bond behavior and strength (Al-Sulaimani et al. 1990, Cabrera and Ghoddoussi 1992, Clark and Saifullah 1993, Rodriguez et al. 1994, Almusallam et al. 1996, Berto et al. 2008, Al-Hammound et al. 2010) are good examples of the many experimental tests available in the field. This paper aims to provide a clear approach on finite element modeling of the response of corroded reinforce concrete beams, considering the change in: steel cross sectional area both in longitudinal and transverse reinforcement, yield strength of the steel material, mechanical properties of concrete in tension and compression, and bond. The results from the developed finite-element models will be validated with those from Rodriquez et al. (1996 and 1997) experimental tests.

3.3 Corrosion effects on material behaviors

3.3.1 Corrosion of reinforcing steel

The effect of steel corrosion can be accounted for by reducing the cross sectional area of reinforcing bars, decreasing yield and ultimate strengths and enforcing a lower ultimate strain in constitutive model of steel. Corrosion can occur in two forms: general and pitting. The pitting corrosion starts by a localized dissolution of the metal surface due to attack by chloride ions. On the other hand the uniform dissolution of the passive steel surface results in general corrosion. The reduction of cross sectional area of the steel bar due to pitting corrosion can be expressed as the following (Berto et al. 2008):

$$A_s^r = \frac{\pi(D_0 - \lambda x)^2}{4} \tag{3-1}$$

In general (uniform) corrosion, the procedure suggested by Alipour (2010) could be used:

$$A_s^r = \frac{(\pi D_0^2 - 4\Delta V_{loss})}{4} \tag{3-2}$$

where A^r_s is the residual cross sectional area of a steel bar, D_o is the initial diameter of a steel bar, x is corrosion depth in the bar (Val and Melchers 1997), λ takes into account the possibility of a one-side or two-side corrosion attack penetration, ΔV_{loss} is the change in the volume of corroded steel per unit length.

Apostolopoulos et al. (2013) conducted an experiment and proved that the yield strength and uniform elongation progressively impaired after corrosion initiation. In high levels of corrosion, the steel becomes very brittle which can result in sudden rupture of reinforcement and ultimately the structural failure. The residual strength of corroded reinforcement can be estimated using the following empirical formula (Du et al. 2005):

$$f_y^r = (1 - 0.005 m_{loss}) f_y^0 \tag{3-3}$$

where f_y^r is the residual yield strength of corroded reinforcement, f_y^0 is the yield strength of pristine reinforcement and m_{loss} is the percentage of steel mass loss, calculated from the consumed mass per unit length divided by the initial steel mass per unit length ($m_{loss}=M_{loss}/M_0\times100$).

Ductility reduction is generally associated with notch formation during the pitting corrosion (Berto et al. 2008) and can be taken into account by adopting a lower ultimate strain for steel. The ultimate strain of steel is linearly dependent on the reduction of steel cross sectional area. Coronelli and Gambarova (2004) suggested the following simplified equation:

$$\varepsilon'_{su} = \varepsilon_{sy} + \left(\varepsilon_{su} - \varepsilon_{sy}\right)\left(1 - \frac{\alpha_{pit}}{\alpha_{pit}^{max}}\right) \quad (3\text{-}4)$$

where α_{pit} is the percent reduction of the bar cross section, ε_{sy} is the steel yield strain, and ε'_{su}, and ε_{su} are the ultimate strain of corroded steel and pristine steel, respectively. Equation 4-4 is only applicable for $\alpha_{pit}< \alpha_{pit}^{max}$.

By defining the reduction percentage of the rebar cross sectional area α_{pit}, the evolution of steel ultimate strain can be described. If the steel is not corroded Equation 3-4 will reduce to: $\varepsilon'_{su}=\varepsilon_{su}$ (i.e., $\alpha_{pit}=0$) in contrary $\varepsilon'_{su}= \varepsilon_{sy}$ indicates a complete loss of ductility.

3.3.2 Concrete degradation

The expansion of rust layers around the steel rebar during corrosion process causes internal pressure to the surrounding concrete and eventually result in cracking and spalling of the cover. General corrosion is known to be the major cause of most of concrete cover spalling compared to the pitting corrosion (Berto et al. 2008). The corrosion effect on concrete can be considered by decreasing the thickness of concrete cover elements, decreasing the concrete compressive strength in the concrete cover and using a brittle post-peak behavior in the constitutive model

of concrete (Coronelli and Gambarova 2004). The reduced compressive strength of concrete can be calculated using the following equation:

$$f_c^r = \frac{f_c'}{1+\frac{R\varepsilon_a}{\varepsilon_c}} \tag{3-5}$$

$$\varepsilon_a = \frac{b_1}{b_0} - 1 \tag{3-6}$$

$$b_1 = b_0 + nw \tag{3-7}$$

where ε_c is the strain at the compressive strength f'_c, ε_a is the average tensile strain in cracked concrete perpendicular to the direction of the applied compression, R is a coefficient related to the roughness and diameter of reinforcement. R = 0.1, recommended by Coronelli and Gambarova (2004), b_0 is the original width of the cross section, b_1 is the increased width due to corrosion cracks, n is the total number of the reinforcement in the top layer, and w is the total crack width, which can be calculated based on Molina et al. (1993).

$$w = \sum_i w_i = 2\pi x_b(\lambda - 1) \tag{3-8}$$

where w_i is each single crack width, x_b is the radius reduction of reinforcement, and λ is the volumetric ratio, which varies depending on the composition of corrosion products. The value of λ can be found in Section 2.5.1 of Chapter Two.

3.4 Bond deterioration

3.4.1 Bond models

Bond is the mechanism through which forces are transferred between reinforcement and surrounding concrete in reinforced concrete structures. Bond in RC structures consists of three main mechanisms: chemical adhesion between steel and concrete, friction due to the roughness of the interface, mechanical interlock (bearing forces) between the ribs of deformed bars and surrounding concrete (ACI Committee 408 2003). When a deformed bar moves with respect

to surrounding concrete, chemical adhesion is lost, and bearing forces and frictional forces are mobilized. As slip increases, friction reduces. After initial slip of the bar, most of the forces are transferred by bearing. If concrete cover, bar spacing or stirrups is not sufficient, the system will fail by splitting failure. If concrete cover or bar spacing is sufficient, or there is enough transverse reinforcement provided to prevent splitting failure, the system will fail by pull-out failure. In the pull-out failure, the concrete between bar lugs shears off from surrounding concrete. If the anchorage to concrete is adequate, the system can fail due to yielding.

According to ACI Committee 408 (2003), the bond strength is governed by

- The mechanical properties of concrete (tensile and bearing strength),
- The volume of concrete around the reinforcement, related to concrete cover and bar spacing,
- The presence of confinement, in the form of transverse reinforcement,
- The surface condition and geometry of reinforcement, such as deformation height, width, spacing and face angle.

According to *fib* (2010), the bond stress-slip relation for ribbed bars in well-confined concrete is described as Figure 3-1 and Equation 3-9.

$$\tau_b = \begin{cases} \tau_{b,max}\left(\frac{S}{S_1}\right)^{\alpha} & 0 \le S \le S_1 \\ \tau_{b,max} & S_1 \le S \le S_2 \\ \tau_{b,max} - \frac{\tau_{b,max}-\tau_f}{S_2-S_3}(S-S_3) & S_2 \le S \le S_3 \\ \tau_f & S_3 \le S \le S_4 \\ 0 & S \ge S_4 \end{cases} \quad (3\text{-}9)$$

where τ_b is bond stress, S is slip, $\tau_{b,max}$ is maximum bond stress, τ_f is the bond stress at the lower constant level (40% of $\tau_{b,max}$), α and S_1~S_4 are the parameters of the model, see Table 3-1 (*fib* 2000).

The bond-slip curve can be characterized by different stages. At the first stage, there is a nonlinear increase of bond stress up to the maximum bond strength, $\tau_{b,max}$. This stage refers to the mechanism of local crushing and micro-cracking due to the penetration of steel rebar ribs into concrete. The slip during this stage is relatively small. The decreasing slope indicates the degradation of stiffness during this stage which is an indicator of the damage progress. Normally under confined conditions, the bond stress remains constant for a certain range of slip. This stage corresponds to the advanced and continued crushing and tearing off of the concrete. If there is a lack of confinement or progress in deterioration, this horizontal stage will become inclined with a negative slope representing a splitting failure rather than a pull-out failure. After that, the bond stress will decrease to a much smaller constant level, τ_f. This curve indicates a typical mechanism for pull-out failure if the steel rebar in concrete is well-confined. However, if the steel is under poor confinement condition or deterioration, instead of pull-out failure, splitting failure will occur (Figure 3-1-dashed line).

3.4.2 Bond loss

3.4.2.1 Experimental tests

Al-Sulaimani et al. (1990) conducted a series of pull-out and beam tests to examine the bond behavior at different stages of reinforcement corrosion: non-corrosion, pre-cracking, cracking and post-cracking levels. They obtained the bond stress/load-slip relationship at different corrosion levels and showed that the bond strength increased with the increase of corrosion under low level of corrosion up to 0.5 to one percent, but decreased consistently with further increase of corrosion. The initial increase in bond strength was due to the increased roughness of steel-concrete interface caused by the growth of the expansive rust. With the opening of a longitudinal crack, a sharp jump will be noticed in the free slip. In their pull-out tests simulating

severe localized corrosion, the bond strength increased up to 1.7 times that of non-corroded specimens at 1 percent corrosion and declined almost linearly to a negligible level at 8.5, 7.5 and 6.5 percent corrosion for 10, 14 and 20mm bars, with *c*/*d* ratios of 7.50, 5.36 and 3.75, respectively. In the beam tests, the decrease of bond strength after initial increase was very gradual. In the beam specimens with adequate development length of reinforcement and proper amount of shear stirrups ensuring that the flexural failure precedes bond and shear failure, the ultimate load was not affected by corrosion up to 1.5 percent and reduced by 12 percent for 4.5 percent corrosion. This phenomenon is due to the cross sectional area reduction. It was reported that the bond behavior was greatly influenced by the concrete cover to bar diameter ratio, the surface condition of the bar, as well as the confinement of the bar.

Cabrera and Ghoddoussi (1992) conducted a series of pull-out and beam tests to investigate the effect of reinforcement corrosion on bond strength, crack width and deflection. According to their pull-out tests, the bond strength increased with corrosion up to a maximum and then significantly decreased. For example, the residual bond strength of the specimens at 12.6 percent corrosion was only 23.8 percent of the bond strength in pristine condition. In the beam tests, the variation of bond strength with corrosion has a similar trend. The critical bond stress of tested beams due to bond failure increased by 16-18 percent at about 0.5 percent corrosion. The residual bond strength of tested beams failed in flexure at 9.2 percent corrosion was around 80 percent of the original bond strength.

Almusallam et al. (1996) conducted pull-out tests to examine the effect of reinforcement corrosion on bond strength, free end slip and failure mode in pre-cracking, cracking and post-cracking stages. The influence of crack width and rib profile degradation on bond strength was another factor considered. It was found that in the pre-cracking stage (0-4

percent corrosion), the bond strength increased by 17 percent with a decrease in the slip at bond strength. The first crack appeared at 5 percent of corrosion, and the bond strength decreased gradually at 5-6 percent corrosion. After that point, the bond strength dropped dramatically. At a corrosion level of 7 percent, the residual bond strength decreased to 35 percent of the original strength. Significant increase in crack width and rib profile loss was noticed at 5-7 percent of corrosion, resulting in the sharp reduction of 30 to 70 percent in bond strength, after which there was only 20 percent loss in bond strength up to 80 percent corrosion. The failure mode at a corrosion level of 4-6 percent is the splitting failure. The failure occurred suddenly at a very low free end slip. At the ultimate bond failure, a large slip was noted due to the slitting of specimens. The failure mode changed from splitting to continuous slippage at a corrosion level of around 12 percent, due to loss of rib profile, production of rust layer and loss of confinement.

The results of a series of pull-out tests were reported in Rodriguez et al. (1994) to investigate the bond behavior of corroded RC beams, and the influence of c/d ratio, bar position and amount of stirrups on bond deterioration. Empirical formulas which best fitted the experimental data were then developed. Rodriguez et al. (1997) conducted a series of experiments on RC beams to study the effect of corrosion on their structural capacity. It was found that reinforcement corrosion reduced the strength at ultimate load, and increased both deflections and crack widths at service load. Reinforcement corrosion changed failure mode from bending to shear in most of the cases. The reduction of bar section at pits and cracking of concrete significantly reduced the load carrying capacity in corroded beams. The confinement produced either by transverse reinforcement or external pressure at support region had an

influence on residual bond strength. The load carrying of tested beams decreased by 20-40 percent depending on the reinforcement ratio and arrangement.

Auyeung et al. (2000) conducted pull-out tests with 19mm reinforcement to study the loss of bond strength under various corrosion levels (0-5.91 percent). They reported that low levels of corrosion less than one percent improved bond strength and bond stiffness. The bond strength increased by about 30 percent at a corrosion level of one percent. Corrosion levels of more than one percent caused reduction in bond strength. However, even after severe corrosion (5.91 percent), measurable bond strength still existed (about 23 percent of the original bond strength). Slip at failure decreased exponentially with corrosion, meaning that ductility reduced with corrosion. Cracking started when corrosion approached approximately 2 percent and deterioration accelerated after cracking. The specimen with less than 2 percent corrosion failed by simultaneous concrete splitting and pull-out failure, whereas those with 2 percent corrosion failed by splitting failure. Specimens with higher level of corrosion resulted in less brittle failure even the slip at maximum load decreased consistently.

Al-Hammound et al. (2010) conducted nine beam tests to assess the bond behavior of non-corroded and corroded RC beams under both monotonic and fatigue loads. They reported that the fatigue bond strength reduced by 30 percent at a corrosion level of 3.9 percent, compared to the static bond strength reduced by 25 percent at the same corrosion level. The decrease in fatigue bond strength did not change significantly with fatigue life. The fatigue life of RC beams varied linearly with the applied load range with a very small slope. It was shown that fiber reinforced polymer (FRP) reinforcement can be an alternative to traditional methods for repairing and strengthening RC structures.

3.4.2.2 Numerical models

Many experimental studies devoted to bond loss, such as those mentioned in the previous section, lead to the following conclusions: the corrosion of the reinforcement affects the bond strength. At the initial stage of corrosion, the rust penetrates into the porous media resulting in increased bond strength. As the volume of corrosion products increase with corrosion progress, cracking of surrounding concrete initiates and the bond between steel and concrete deteriorates (Figure 3-2). Therefore, the bond-slip relationship must be modified accordingly to incorporate the corrosion effects, shown in Figure 3-1.

Rodriguez et al. (1994) proposed an expression based on their tests to calculate the residual bond strength and describe the descending branch of the corroded bond-slip curve:

$$\tau_{b,max}^{r} = K x_b^{-\Gamma} \tag{3-10}$$

where $\tau^{r}_{b,max}$ is the residual bond strength (MPa), x_b is corrosion attack penetration or bar radius reduction (μm), and K and Γ are constants to fit with test results.

Coronelli and Gambarova (2004) modified the bond-slip relationship based on Rodriguez et al. (1994), assuming the corrosion is uniformly distributed (at the same corrosion level x_b), thus the bond-slip relationship is the same for the entire reinforcement.

$$\tau_{b,max}^{r} = \tau_c + \tau_s = 0.6\left(0.5 + \frac{c}{d}\right) f_t'(1 - \psi x^{\mu}) + \frac{\kappa A_{tr} f_y}{s_{tr} d} \tag{3-11}$$

where τ_c is contribution of concrete to bond, τ_s is contribution of stirrups to bond, f'_t is the tensile strength of concrete, f_y is yield stress of the stirrups, c/d is concrete cover to bar diameter ratio, s_{tr} is spacing of stirrups, A_{tr} is cross sectional area of stirrups and ψ, μ, and κ are empirical constants (Berto et al. 2008).

This expression is obtained by fitting various experimental bond test results and depends on the material and geometrical characteristics of the test specimens. The validity of

this equation is limited to those cases where the general arrangement of the reinforcement is close to the tests conducted by Rodriguez et al (1996).

Val and Chernin (2009) modified the bond-slip relationship based on some experimental results from several researchers. The proposed expression is as follows:

$$\frac{\tau^{r}_{b,max}}{\tau_{b,max}} = \begin{cases} (1+K_1)\frac{x_b}{x_{cr}}, & x_b \le x_{cr} \\ max[K_1 - K_2(x_b - x_{cr}); 0.15] & x_b > x_{cr} \end{cases} \quad (3\text{-}12)$$

where $\tau^{r}_{b,max}/\tau_{b,max}$ is the normalized bond strength, representing the ratio of the residual bond strength under corrosion to the initial bond strength, x_{cr} is the corrosion penetration corresponding to crack initiation in concrete cover (Equation 3-13), K_1 is the initial increase of the bond strength after corrosion initiation, depending on confinement level provided by concrete cover and stirrups (Equation 3-14), and K_2 is the rate of bond strength degradation after formation of cracks (Equation 3-15).

$$x_{cr} = a_1 + a_2\frac{c}{d} + a_3 f_t' \quad (3\text{-}13)$$

$$K_1 = \begin{cases} 1 & c/d \le 1 \\ 1 + 0.085\left(\frac{c}{d} - 1\right) & c/d > 1 \end{cases} \quad (3\text{-}14)$$

$$K_2 = \begin{cases} 0.005 & \rho \le 0.25 \\ 0.005 - \frac{\rho - 0.25}{300} & 0.25 < \rho \le 1 \\ 0.0025 & \rho > 1 \end{cases} \quad (3\text{-}15)$$

where a_1 - a_3 are coefficients, obtained by the regression analysis (μm), and ρ is the total area of stirrups within the development length to that of longitudinal reinforcement enclosed by stirrups.

The bond stiffness between concrete and steel varies depending on the corrosion level. However, most of the current research focuses on the corrosion effect on bond strength. Not many researchers study the corrosion effect on bond stiffness. Some test results shows that the

variation of bond stiffness at different corrosion levels (Almusallam et al. 1996, Auyeung et al. 2000). Clark and Saifullah (1993) conducted a series of pull-out tests and found out that for both plain and ribbed bars, bond stiffness initially increased with increase of corrosion level and started to decrease just before bond strength reached the maximum value. Bond stiffness kept decreasing thereafter, with a high rate up to a stage when a visible crack appeared on the surface of concrete cover, and then with a very slow rate with further corrosion. However, this does not agree with the result from Al-Sulaimani et al. (1990), which indicated that bond stiffness decreased with increase of corrosion at the pre-cracking stage. In addition, some researchers believe that the expected possible reduction of bond stiffness due to corrosion will lead to a small decrease of structural stiffness of RC beams (Val and Chernin 2009). Further research might be needed to reach a unanimous conclusion.

According to *fib* (2000), the bond stress can be determined using

$$\tau_b = \tau_{b,\max}^{r}\left(\frac{S}{S_1}\right)^{0.4} \tag{3-16}$$

The bond stiffness varies as the bond strength changes due to corrosion. A decrease of bond stiffness will be noticed when the corrosion is increasing. Using this formula, the variation of bond stiffness can be derived.

3.5 Validation with experimental results

Rodriguez et al. (1997) conducted experimental tests on 40 beams to assess the structural behavior of concrete structures with corroded reinforcement. The analytical models in this paper have been compared with their experimental results of two types of simply supported reinforced concrete beams (Type 11 and 31) with different corrosion levels. Type 11 and 31 beams were different due to facts such as ratio of tensile and compressive reinforcements and spacing of shear reinforcement. Both the corroded and non-corroded beams were tested up to

failure. Two symmetrical point loads were applied at a distance of 200 mm from the middle section of the beam by a hydraulic actuator with a constant increasing rate. The vertical displacement at mid-span was continuously measured during the loading test and the slip between the ends of the bottom steel and the surrounding concrete was measured by dial-gauges. Figure 3-3 and Table 3-2 show the geometry and corrosion level of the experimental beam samples. Material properties of the reinforcement are listed in Table 3-3. The load-deflection curves obtained in the tests are plotted in Figures 3-8 and 9.

3.6 Finite element modeling

3.6.1 Concrete models

Modeling of concrete is a very important aspect in simulating reinforced concrete structures. Currently, there are three different constitutive models for concrete available in ABAQUS: the brittle cracking model, the smeared crack concrete model and the concrete damaged plasticity model (ABAQUS 2012). The brittle cracking model is intended for the applications with a dominant tensile cracking, as the model is capable of considering the anisotropy induced by cracking. Compressive failure is not important and elastic behavior in compression is assumed. The smeared crack model is designed for the cases where the concrete is subjected to essentially monotonic straining, either tensile cracking or compressive crushing. The most important aspect of concrete behavior is assumed to be cracking. The representation of cracking and post-cracking anisotropic behavior dominates the modeling. The smeared crack model does not track individual “macro” cracks. Constitutive calculations are independently performed at each integration point. To account for the presence of the cracks, the stress and material stiffness at each integration point is updated if a crack occurs. This concrete model is

often used to model reinforced concrete structures (Thiagarajan and Roy 2005, Steinberg et al. 2011, Valente 2012 and Li et al. 2014).

The damaged plasticity model is designed for applications with the concrete under arbitrary loading conditions, such as cyclic and dynamic loading. It uses concepts of isotropic damaged elasticity in combination with isotropic tensile and compressive plasticity to represent the inelastic behavior of concrete and also accounts for stiffness recovery effects during cycle load reversals. The model is a continuum, plasticity based, damage model for concrete. Two main failure mechanisms: tensile cracking and compressive crushing are considered. The elastic behavior of concrete is assumed to be isotropic and linear. The damaged plasticity model is widely used to model reinforced concrete structures (Grace and Jensen 2008, Sinaei et al. 2012 and Mohamed et al. 2012). It is selected to model the concrete in the FE models in this study. The uniaxial tensile and compressive behavior of concrete in damaged plasticity model is shown in Figure 3-4.

3.6.2 Steel reinforcement models

Within the framework of finite element modeling, there are three different approaches to model the steel reinforcement: the discrete model, the embedded model and the smeared model (El-Mezaini and Citipitioglu 1991, Thiagarajan and Roy 2005).

In the discrete model, the steel bar and the concrete are modeled as distinct elements. The interaction between concrete and steel are normally simulated using some interface elements or connectors. This approach is capable of capturing the bond-slip behavior between concrete and steel as well as the corrosion effect on the bond mechanism. The disadvantage of discrete modeling is the restriction that is imposed on the finite element mesh patterns by the location of reinforcement. In terms of element selection, different types of elements are

allowed in this approach. For example, both concrete and steel can be modeled using plane elements (Berto et al. 2008) or solid elements (Valente 2012). Using this method, the geometry of the steel bar, such as the shape of the ribs, can be accurately modeled to capture the effect of geometrical characteristics providing the option for an accurate and localized analysis. To achieve the increased accuracy, very fine meshes are required which result in high computational costs. A great application would be to model the concrete block with the reinforcement to study bond-slip relationship. The alternative method is to use line elements, such as beam or truss elements to model the reinforcement. Although this method significantly simplifies the real behavior, it requires specific constitutive law for interface elements. Therefore, it is still able to take into account the major aspects of bond phenomena and the geometrical characteristics of bond zone, such as rib size, bar size and spacing (Birgul et al. 2003 and Koyuncu et al. 2003).

In the embedded model, the steel bar and the concrete are modeled separately. The bar elements are then embedded into the host concrete element, so that the nodes of embedded bar elements have the same displacement as that of the concrete element. Example of the application of embedded model can be found in Darmawan and Stewart (2007), Mohamed et al. (2012) and Sinaei et al. (2012). The embedded model overcomes the problem of mesh dependence in discrete model. It allows independent choice of concrete mesh, however, the additional nodes of reinforcement increase the total number of degree of freedom (DOF) and the computational effect (El-Mezaini and Citipitioglu 1991). Moreover, this approach cannot simulate the bond loss between concrete and steel under corrosion. Perfect bond is assumed in this model.

In ABAQUS, the embedded model can be achieved by the constraint “embedded region”. The embedded element technique can be used to specify an element or a group of elements embedded in a group of host elements, which constrain the translational degrees of freedom of the embedded nodes (ABAQUS 2012). Different element types for embedded elements are allowed, for instance, solid elements embedded in solid elements, truss or beam elements embedded in solid elements, shell, membrane or surface elements in solid elements. Perfect bond is assumed if using this method.

In the smeared model, reinforcing bars are assumed to be smeared into every element of concrete. The bars are modeled implicitly by adding its stiffness to the material property of concrete. Perfect bond is assumed in the smeared model. This model is frequently used for studying the global behavior of reinforced concrete structures. However, it cannot directly simulate the bond-slip behavior between concrete and steel. Considering that bond loss is a major issue when modeling corroded RC structures, this model is not appropriate.

In ABAQUS, there is a rebar option, under which there are two ways to model the reinforcement: i) rebar layers; ii) element-based rebars. The first method is to define layers of uniaxial reinforcement in membrane, shell, and surface elements. Such layers are treated as a smeared layer with a constant thickness, which is equal to the area of each bar divided by the bar spacing. The way to define rebars in solid elements is to embed reinforced surface or membrane elements in the host solid elements. The second way is to define uniaxial reinforcement in shell, membrane, and solid elements as an element property. The element-based rebar can be defined as individual bars in solid elements, or layers of uniformly spaced bars in shell, membrane, and solid elements (ABAQUS 2012). This method is more

complicated than the first method. Both methods assume perfect bond between concrete and steel.

For corroded RC structures, when the bond mechanism and the corrosion effect on bond need to be modeled, the discrete model is necessary. However, some researchers believe that the effect of bond-slip can be included by the application of tension stiffening (Thiagarajan and Roy 2005). Therefore, the bond-slip behavior of RC structures can be modeled using the embedded or smeared model with tension stiffening.

In order to assess the structural performance of RC structures subjected to corrosion, the reinforcement is modeled explicitly using the discrete model in this study. The bilinear hardening model of steel, which is widely used, will be adopted for the steel reinforcement in the FE models.

3.6.3 Bond modeling

The interaction between concrete and steel, i.e. bond-slip effect, can be modeled via different ways or different interface elements. Coronelli and Gambarova (2004) proposed a two dimensional FE model to investigate the structural response of corroded RC beams with four node plane stress elements for the concrete and two node truss elements for the reinforcement. The bond behavior between concrete and steel was modeled via bond-link elements, which exhibited a relative slip between concrete and steel. Similarly, Val and Chernin (2009) developed a two dimensional FE model to study the behavior of RC beam with corroded reinforcement. The two node beam element with three DOFs was used for the concrete and the two node bar element with one DOF was used for the corroded reinforcement. The interface element, which modeled the bond and its deterioration under corrosion, is a four node element with two nodes having three DOFs and two nodes having only one DOF. Both Coronelli and

Gambarova (2004) and Val and Chernin (2009) verified their model with available experimental data.

In ABAQUS, there are two main options to model the bond slip relationship: springs either linear or non-linear and connectors either Translator or Axial. Koyuncu et al. (2003) modeled a simply supported AASHTO Type-III I-girder in ABAQUS using eight node solid elements for the concrete and two node truss elements for the tendons. The truss elements were connected to the concrete at the nodes through linear springs with constant stiffness. Linear elastic bond-slip behavior was assumed in the FE model. As a matter of fact, the bond-slip behavior is a nonlinear relationship, therefore, in order to capture the nonlinear behavior and the deterioration due to corrosion, non-linear spring elements are selected to model the bond-slip behavior between concrete and steel for the FE models in this study.

Spring elements can couple a force with a relative displacement. They can model actual physical springs as well as idealize axial and torsional components (ABAQUS 2012). Spring elements can either be between a node and ground or between two nodes. The spring elements used in this study are defined between two nodes with a fixed direction (Figure 3-5).

The relative displacement across the spring element is the difference between the *m*th displacement component of the first node and the *n*th displacement component of the second node:

$$\Delta u = u_m^1 - u_n^2 \tag{3-17}$$

The direction of action for the spring element is defined by giving the DOF at each node of the element. The DOF can be in a local coordinate system, which is assumed to be fixed. To obtain a tensile spring, the element should be set up as shown in Figure 3-5, so that when $u^1{}_m = 1$ and $u^2{}_n = 0$, the force in the spring element is positive and the spring appears to be in tension.

Other option in ABAQUS for modeling the bond-slip behavior is to use connectors, such as Translator or Axial, which can provide a connection between two nodes and define linear or nonlinear spring-like behavior. Li et al. (2014) developed a 2-D FE model in ABAQUS for RC seawalls subjected to corrosion. The compressive steel bar was assumed to be perfectly bonded with the concrete and the tensile steel bar was connected to the concrete through the line element Translator. The translator has two nodes, but only the displacement in the x-axis of local coordinate system is enabled and all other DOFs of the two nodes are relatively restrained to each other. Thus, only axial relative movement between the two nodes is allowed. The two nodes of the translator are connected to the concrete and the steel nodes, respectively, representing the physical bond. The bond-slip relationship considering corrosion effect can be assigned to the force-displacement relationship of the translator. Their FE results were then compared with the experimental results, showing a good agreement between the numerical and experimental results.

As mentioned before, the effect of bond-slip behavior may also be modeled approximately by introducing some tension stiffening into the concrete modeling (ABAQUS 2012). Tension stiffening characterizes concrete ability to carry tension between cracks. Tensile force is carried by both concrete and steel in RC beams. After concrete cracks, the load is transferred across cracks though the steel at individual cracks. Tension stiffening decreases tension in the steel due to bond. In terms of numerical modeling, it can reduce the mesh sensitivity and hence improve the accuracy of the FE models in presenting cracks. It can also improve the stability of numerical solutions. The amount of tension stiffening depends on factors such as density of reinforcement, quality of bond, relative size of concrete aggregate compared to rebar diameter and mesh of the FE model. Tension stiffening can be specified by

means of a post-failure stress-strain relation or by applying a fracture energy cracking criterion (ABAQUS 2012). Therefore, by appropriately modifying the post-cracking stress-strain relation of the concrete model, a reasonable amount of tension stiffening can be included to approximately model the bond-slip effect. Examples of the application of tension stiffening to model the bond-slip behavior is presented in Thiagarajan and Roy (2005). However, this method can only approximately model the effect of bond-slip. The amount of tension stiffening needs to be estimated and calibrated to each particular case. In order to directly apply the nonlinear constitutive law of bond and the corrosion effect on bond to obtain more accurate results for corroded RC beams, a discrete model of steel with a proper type of interface elements presenting bond is necessary.

3.6.4 Element type

Sinaei et al. (2012) proposed a three dimensional model in ABAQUS to study the structural behavior of RC beams. The concrete was modeled using an eight node linear brick element with reduced integration. The reinforcement was modeled using a three dimensional two node linear truss element. The reinforcement was embedded in the solid elements of concrete. The FE results were compared with the experimental data for the beams under flexural loading. It was shown that the mid-span deflection, the tensile strain of reinforcement, and the compressive strain of concrete from FE models were in good agreement with the experimental results. Mohamed et al. (2012) developed a three dimensional model in ABAQUS for reinforced concrete deep beams, the result of which showed a good agreement with the experimental result. The concrete was modeled using eight node solid elements and the embedded reinforcement was modeled using three dimensional truss elements. Similarly, Darmawan and Stewart (2007) and Grace and Jensen (2008) modeled RC beams in ABAQUS

using eight node solid elements for concrete and two node truss elements for steel strands. The results showed the selections of element types were efficient.

In this study, three dimensional eight node solid element is selected to model the concrete for the FE models, and three dimensional two node truss element is selected to model the steel reinforcement.

3.6.5 FE model development

Three dimensional nonlinear finite element models, which are capable of considering the nonlinearity of material and geometric properties, are proposed in this paper to model the tested beams in the experiment test by Rodriguez et al. (1996). The analysis was conducted in FE software ABAQUS. Three dimensional eight node solid elements are selected for the concrete beam. The reinforcement is modeled using the three dimensional two node linear truss elements.

The interaction between the concrete and steel, i.e. bond-slip effect, is modeled via spring elements. In this study, to capture the effects of bond deterioration on structural behavior, nonlinear springs have been introduced on the interface of the concrete and truss elements. For intact beams (Beam 111 and 112, Beam 311 and 312), the truss elements are embedded in the solid elements. The finite element model is shown in Figure 3-6.

The bilinear hardening model (Figure 3-7left) is adopted for the steel reinforcement, with a density of 7850 kg/m^3, Young's modulus of 200 GPa, and Poisson's ratio of 0.3. The damaged plasticity model is selected to model the concrete material. This material is capable of considering the degradation of the elastic stiffness induced by plastic straining both in tension and compression (ABAQUS 2012). The nonlinear tension stiffening effect after

concrete starts cracking is also included. The constitutive model for concrete is shown in Figure 3-7right.

The modified bond-slip relationship considering the corrosion effects is adopted for the models of corroded beams. The elements used to model bond-slip effect are nonlinear springs. The displacement can represent the slip between concrete and steel. The force in the spring is the bond stress multiplied by the contact area between steel and concrete along element length.

$$F = \tau_b A_{cont.} = \tau_b \pi d L \tag{3-18}$$

where d is the diameter of the reinforcement and L is the element length.

The residual bond strength $\tau^{r}_{b,max}$ under corrosion can be calculated by Equations 3-10 to 3-12. Table 3-4 compares the residual bond strength for the corroded beams using these equations which shows that the two methods are fairly comparable.

3.7 Results and discussions

The results of the finite element analysis are shown in Figures 3.8 and 3.9. Type 11 beams with low reinforcement ratio failed by tensile reinforcement according to the test results. Beam 111 is a non-corroded beam that shows a stiffness degradation when bottom bars reaches the yield stress. In the finite element model, the bottom steel yields at a load of 41.36 kN. The crushing of concrete does not initiate when the tensile steel yields. The concrete at the bottom near mid-span starts to crack when the applied load reaches 26.25 kN, After concrete cracks, the stiffness of the beam decreases drastically.

The corrosion-induced mass loss at the level of bottom bars in Beam 115 is equal to 13.9%. The load versus mid-span deflection curve of this beam with low corrosion level is similar to that of the non-corroded beam. Concrete at the bottom starts to crack when the applied load reaches 21.67 kN, followed by the significant stiffness degradation. Then the

tensile reinforcement yields at a load of 32.50 kN. The load carrying capacity of the beam decreases by 21.4% compared to the pristine beam. The concrete cover is not heavily deteriorated as the corrosion of the compressive reinforcement is only 12.6%. The crushing is not initiated in concrete when the bottom steel yields.

The corrosion of the tensile steel in Beam 114 is 17.2%. The cracking in concrete initiates when the load reaches 18.22 kN, which is much lower than 26.25 kN for the pristine Beam 111. The concrete crushing occurs prior to the tensile steel yielding due to heavily corroded top reinforcement (24.3% mass loss due to corrosion). The bottom bar yields at a load of 30.22 kN. The load carrying capacity decreased by 26.9% compared to the pristine beam.

Beam 116 is heavily corroded. According to the test, Beam 116 finally fails due to pits in the tensile bars. The maximum value at pitting in the bottom bars is 2.1mm. The pitting corrosion is not considered in the finite element model; only general corrosion which is 26.4% is applied to the model. Yielding in the bottom bars occurs at 26.76 kN. The load carrying capacity decreases by 35.3% when only general corrosion is considered.

Type 31 beams with high reinforcement ratio fail by concrete crushing according to Rodriguez et al. (1996). A slope change occurs when tensile steel yields in the pristine beam 311. In the finite element model, the bottom steel yields when the applied load reaches 104.49 kN, which is much higher than the load carrying capacity of Type 11 beams due to its higher reinforcement ratio. After the tensile steel yields, the curve follows a quasi-horizontal line. The cracking of concrete first starts at a load of 18.09 kN, after concrete starts cracking a slope degradation of the load-displacement curve is observed which indicates the stiffness degradation. Top concrete crushes when the applied load reaches 76.42 kN. The crushing occurs before the yielding in the bottom steel.

Beam 313 with a corrosion level of 9.8% in tensile bars fails in a lower load compared to the pristine Beam 311. The concrete at the bottom of the beam near the mid-span cracks first when the load reaches 13.86 kN resulting in degradation of stiffness. The crushing of compressive concrete occurs at a load of 61.83 kN while the tensile steel yields later at a load of 86.83 kN with a 16.9% decrement in load carrying capacity.

In Beam 314, with 15.4% corrosion level, crushing in compressive zone starts due to extensive corrosion in compressive steel (12.6%), when the applied load reaches 43.93 kN, which is much earlier than the yielding of the tensile steel. It can be seen from the above that the failure mode of non-corroded beams depends on the reinforcement ratio, in such a way that lightly reinforced beams fail by the yielding of tensile reinforcement without concrete crushing, while moderately reinforced beams are more likely to fail by concrete crushing. The deterioration of the reinforcement significantly affects the structural behavior of reinforced concrete structures, such as load carrying capacity.

There is reasonably good agreement between the experimental results and the finite element results. The main differences are the initial slope of the load versus deflection curves and the overestimation of the load carrying capacity of the corroded beams in the finite element results. A major reason for these discrepancies is the naturally stiffer models in finite element simulation compared to the beams in experimental tests, because of the existence of cracks in the test specimens before loading. The numerical results overestimate the load carrying capacity of the corroded beams because the finite element models account only for general corrosion, i.e. the pitting corrosion is not considered. However, in the test, the localized corrosion usually happens, which causes the non-uniform reduction of load carrying capacity and may lead to structural failure at the maximum pitting locations. Beam 116 is a good

example of this case as it fails due to pitting corrosion in the tensile reinforcement, which explains why the curve obtained from the numerical result is higher than the curve obtained from the test.

Crack patterns can also be obtained from the finite element models. As damaged plasticity model is adopted for concrete, the crack patterns in the concrete beam can be visualized by introducing the concept of an effective crack direction (ABAQUS 2012). Concrete cracking initiates at points where the maximum principal plastic strain (PE, MAX. Principal) is greater than zero. The direction of PE, MAX. Principal is assumed to be parallel to that of the vector normal to the crack plane. This direction is shown in Figures 4-10 to 4-12, indicating the crack patterns of Type 31 beams (311, 313 and 314) under a load of the same value 84kN.

The crack initiated from the concrete at the bottom near the mid-span and propagated upwards. There were more cracks growing along the span when the load was increasing. It can be seen from those figures that subjected to the same external loading, the higher the corrosion level was, the more cracks the beam had. The non-corroded Beam 311 had the least cracks, while cracks in Beam 313 grew deeper towards the top of the beam. The relatively highly corroded Beam 314 had the most cracks and the cracks near mid-span were very severe with relatively large openings.

It can also be noted that for the same beam under the same loading, the mid-span deflection increased a lot when the corrosion increased. At a load of 84kN, the pristine beam (311) had a deflection of 9.78mm, while the mid-span displacements of the corroded beams (313, 314) are 12.58mm and 33.29mm, respectively. It can be known from all above that corrosion may also cause serviceability failure due to excessive cracking or deflections.

3.8 Conclusions

This paper studies the adverse effects of corrosion in reinforcement on structural behavior of reinforced concrete beams. Finite element modeling of such structures requires effective nonlinear models to capture all the major effects of corrosion such as bond degradation, reduction in steel cross section and change of material properties. A nonlinear finite element model which is able to take into account all the parameters above is presented and verified with the available experiment data. Special attention is drawn to model the bond between concrete and reinforcing steel as well as its deterioration under different corrosion levels. The results presented in this paper clearly show that corrosion affects the strength and ductility of a structure at ultimate condition. For instance, the load carrying capacity of Type 11 beams was reduced by 21.4% - 35.3%, depending on corrosion level. The corrosion may also cause excessive cracking and deflection, which leads to serviceability failure. The analytical model can provide a good prediction of the damage process of reinforced concrete structures subjected to corrosion.

3.9 References

ABAQUS (2012). ABAQUS 6.12 Documentation, Dassault Systèmes Simulia Corp.

ACI Committee 408 (2003). "Bond and development of straight reinforcing bars in tension (ACI 408R-03)." American Concrete Institution.

Al-Hammoud, R., Soudki, K. and Topper, T. (2010). "Bond analysis of corroded reinforced concrete beams under monotonic and fatigue loads." *Journal of Cement and concrete composites* 32(3), 194-203.

Alipour, A. (2010). "Life-cycle performance assessment of highway bridges under multi-hazard conditions and environmental stressors." Ph.D. Dissertation, Department of Civil and Environmental Engineering, University of California, Irvine, CA.

Alipour, A., Shafei, B., and Shinozuka, M. (2010). "Life cycle cost analysis of highway bridges in chloride contaminated environments." *In: Proceedings of the ASCE-SEI Structures Congress*, Orlando, FL, May 12-14.

Alipour, A., Shafei, B. and Shinozuka, M. (2011). "Performance evaluation of deteriorating highway bridges Located in High Seismic Areas." *Journal of Bridge Engineering* 16(5), 597–611.

Alipour, A., Shafei, B., and Shinozuka, M. (2013). "Capacity loss evaluation of reinforced concrete bridges located in extreme chloride-laden environments." *Journal of Structure and Infrastructure Engineering*, 9(1), 8-27.

Almusallam, A.A., Al-Gahtani, A.S., Aziz, A.R. and Rasheeduzzafar (1996). "Effect of reinforcement corrosion on bond strength." *Journal of Construction and Building Materials,* 10(2), 123-129.

Al-Sulaimani, G. J., Kaleemullah, M., Basumbul, I. A. and Rasheeduzzafar (1990). "Influence of corrosion and cracking on bond behavior and strength of reinforced concrete members." *ACI Structural Journal*, 87(2), 220–231.

Apostolopoulos, C. A., Demis, S. and Papadakis, V. G. (2013). "Chloride-induced corrosion of steel reinforcement - Mechanical performance and pit depth analysis." *Journal of Construction and Building Materials*, 38, 139-146.

Auyeung, Y., Balaguru, P., and Chung, L. (2000). "Bond behavior of corroded reinforcement bars." *ACI Materials Journal*, 97(2), 214–220.

Berto, L., Simioni, P. and Saetta, A. (2008). "Numerical modeling of bond behavior in RC structures affected by reinforcement corrosion." *Journal of Engineering Structures*, 30(5), 1375-1385.

Birgul, R., Koyuncu, Y., Ahlborn, T. M. and Aktan, H. M. (2003). "A 40-Year Performance Assessment of Prestressed Concrete (PC) I-Girder Bridges in Michigan." *TRB 2003 Annual Meeting CD-ROM*.

Cabrera, J. G. and Ghoddoussi, P. (1992). "The effect of reinforcement corrosion on the strength of the steel/concrete bond." *In: Proceedings of International Conference Bond in Concrete*, Riga, Latvia, 10.11-10.24.

Clark, L. A. and Saifullah M. (1993). "Effect of corrosion on reinforcement bond strength." *In: Proceedings of 5th international conference on structural faults and repairs*, 3, 113-119. Edinburgh: Engineering Technical Press.

Coronelli, D. and Gambarova, P. (2004). "Structural assessment of corroded reinforced concrete beams: Modeling Guidelines." *Journal of Structural Engineering*, 130(8), 1214-1224.

Darmawan, M. S. and Stewart, M. G. (2007). "Spatial time-dependent reliability analysis of corroding pretensioned prestressed concrete bridge girders." *Journal of Structural Safety*, 29(1), 16-31.

Du, Y.G., Clark, L.A., and Chan, A.H.C. (2005). "Residual capacity of corroded reinforcing bars." *Magazine of Concrete Research*, 57(3), 135-147.

El Maaddawy, T., and Soudki, K. (2007). "A model for prediction of time from corrosion initiation to corrosion cracking." *Journal of Cement and Concrete Composites*, 29 (3), 168-175.

El-Mezaini, N. and Citipitioglu, E. (1991). "Finite element analysis of prestressed and reinforced concrete structures." *Journal of Structural Engineering*, 117(10), 2851-2864.

fib (2000). *Bond of reinforcement in concrete*. State-of-art report, fib Bulletin No. 10.

fib (2010). *Model Code*. International Federation for Structural Concrete, Switzerland.

Grace, N. F. and Jensen, E. (2008). "Use of unbounded CFCC for transverse post-tensioning of side-by-side box-beam." Research Report RC-1509, Michigan Department of Transportation (MDOT), Construction and Technology Division.

Koyuncu, Y., Birgul, R., Ahlborn, T. M. and Aktan, H. M. (2003). "Identifying Causes for Distress Patterns in Prestressed Concrete (PC) I-Girder Bridges." *TRB Annual Meeting CD-ROM*.

Li, C. Q., Yang, S. T. and Saafi, M. (2014). "Numerical simulation of behavior of reinforced concrete structures considering corrosion effects on bonding." *Journal of Structural Engineering, ASCE*.

Molina, F.J., Alonso, C. and Andrade, C. (1993). "Cover cracking as a function of rebar corrosion: Part 2 - numerical model." *Materials and Structures*, 26, 532-548.

Pantazopolou, S. J., and Papoulia, K. D. (2001). "Modeling cover-cracking due to reinforcement corrosion in RC structures." *Journal of Engineering Mechanics*, ASCE, 127(4), 342-351.

Rodriguez, J., Ortega, L., and Garcia, A. (1994). "Corrosion of reinforcing bars and service life of reinforced concrete structures: Corrosion and bond deterioration." *In: Proceedings, International Conference on Concrete across Borders*, 2, 315–326.

Rodriguez, J., Ortega, M., Casal, J., and Diez, M. D. (1996). "Assessing structural conditions of concrete structures with corroded reinforcement." *Concrete Repair, Rehabilitation and Protection*, London: E&FN Spon.

Rodriguez, J., Ortega, L., and Casal, J. (1997). "Load carrying capacity of concrete structures with corroded reinforcement." *Journal of Construction and Building Materials*, 11(4), 239-248.

Shafei, B., Alipour, A., and Shinozuka, M. (2012). "Prediction of corrosion initiation in reinforced concrete members subjected to environmental stressors: A finite-element framework." *Journal of Cement and Concrete Research*, 42(2), 365-376.

Shafei, B. and Alipour, A. (2012). "Vulnerability assessment of deteriorated bridges under seismic events." *In: Proceedings of the 15th World Conference on Earthquake Engineering (15WCEE)*, Lisbon, Portugal, September 24-28.

Shafei, B., Alipour, A., and Shinozuka, M. (2013). "A stochastic computational framework to investigate the initial stage of corrosion in reinforced concrete superstructures." *Journal of Computer-Aided Civil and Infrastructure Engineering*, 28(7), 482-494.

Shafei, B. and Alipour, A. (2013). "Assessment of extent of capacity loss in deteriorated highway bridges." *In: Proceedings of the ASCE-SEI Structures Congress*, Pittsburgh, PA, May 2-4.

Sinaei, H., Shariati, M., Abna, A. H., Aghaei, M. and Shariati, A. (2012). "Evaluation of reinforced concrete beam behavior using finite element analysis by ABAQUS." *Scientific Research and Essays*, 7(21), 2002-2009.

Steinberg, E., Miller, R., Nims, D. and Sargand, S. (2011). "Structural Evaluation of LIC-310-0396 and FAY-35-17-6.82 Box Beams with Advanced Strand Deterioration." The Ohio Department of Transportation, Office of Research and Development and the Federal Highway Administration.

Thiagarajan, G. and Roy, S. (2005). "Finite element modeling of reinforced concrete bridge decks with ABAQUS." Technical report UTC R1111, University Transportation Center Program, the University of Missouri-Rolla.

Val, D. and Chernin, L. (2009). "Serviceability Reliability of Reinforced Concrete Beams with Corroded Reinforcement." *Journal of Structural Engineering*, 135(8), 896-905.

Val, D. and Melchers, R. (1997). "Reliability of Deteriorating RC Slab Bridges." *Journal of Structural Engineering*, 123(12), 1638-1644.

Valente, M. (2012). "Bond strength between corroded steel rebar and concrete." *IACSIT International Journal of Engineering and Technology*, 4(5), 653-656.

Table 3-1. Parameters in the bond-slip model for normal strength concrete

$\tau_{b,max}$	τ_f	α	S_1	S_2	S_3	S_4
$0.45f'_{cm}$	$0.4\tau_{b,max}$	0.4	1mm	3mm	Clear rib spacing	3×rib spacing

f'_{cm} is the mean compressive strength of concrete.

Table 3-2. Corrosion levels of test beams

Beam type	Beam number	Concrete f'_c (MPa)	Attack penetration (mm) (general corrosion)		
			bottom	top	stirrups
11	111	49.9	-	-	-
	112	49.9	-	-	-
	114	36.8	0.45	0.52	0.39
	115	31.4	0.36	0.26	0.37
	116	31.4	0.71	0.48	0.66
31	311	48.8	-	-	-
	312	48.8	-	-	-
	313	35.8	0.30	0.20	0.35
	314	35.8	0.48	0.26	0.50

Table 3-3. Material properties of reinforcement

Bar diameter (mm)	Yield stress (MPa)	Ultimate stress (MPa)
6	626	760
8	615	673
10	575	655
12	585	673

Table 3-4. Residual bond strength of corroded Type 11 beams

Beam No.	Attack penetration (mm)	Equation 4-10	Equation 4-11	Equation 4-12
114	0.45	3.37	3.25-4.33	4.1
115	0.36	3.37	3.30-4.40	4.13
116	0.71	3.37	3.11-4.14	4.04

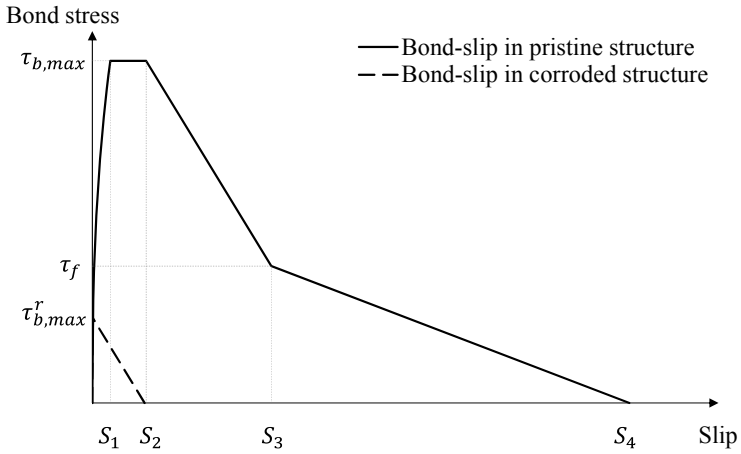

Figure 3-1. Bond-slip model

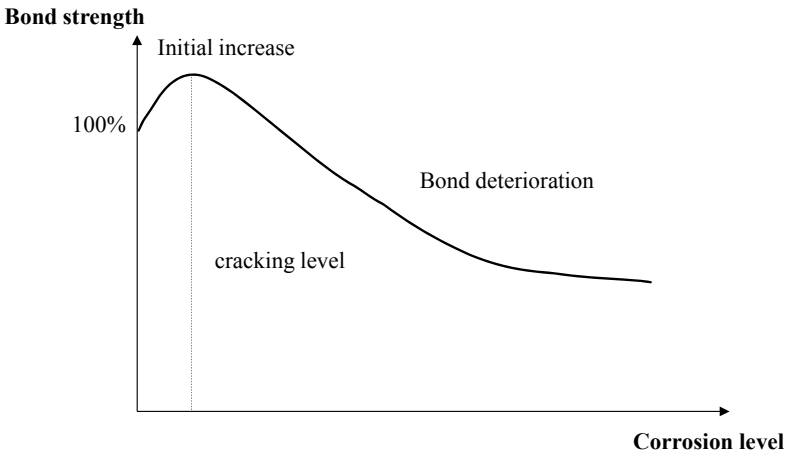

Figure 3-2. Schematic variation in bond strength with corrosion level

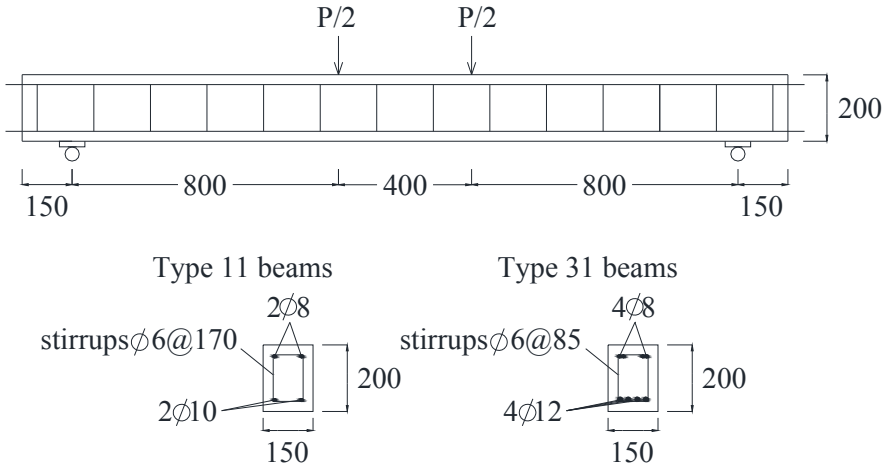

Figure 3-3. Geometry of the test beams (dimensions are in mm) (Rodriguez et al. 1996)

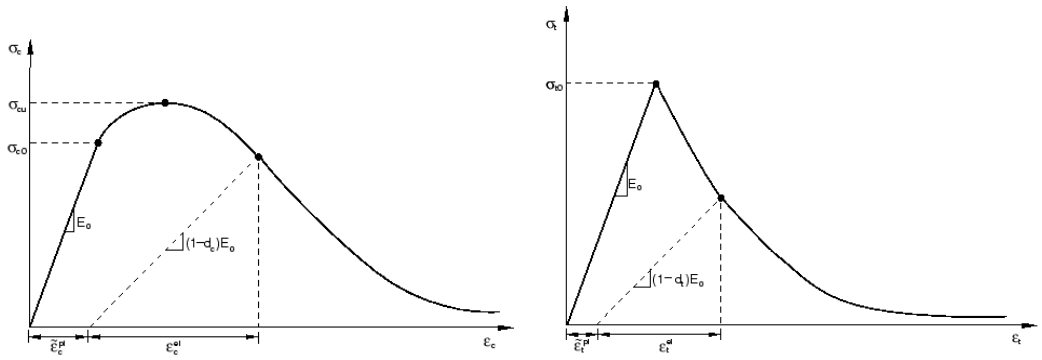

Figure 3-4. Constitutive model of concrete in compression (left) and tension (right)

(ABAQUS 2012)

Figure 3-5. Configuration of SPRING2 element (tensile spring)

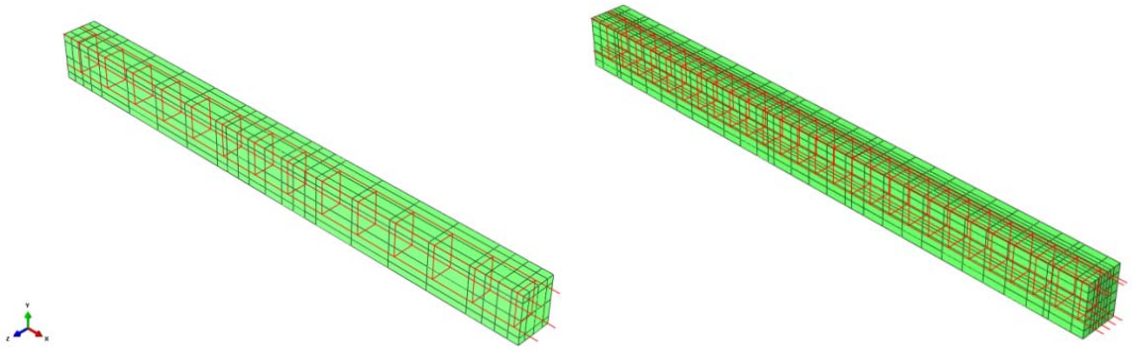

Figure 3-6. FE models of the tested beams: Type 11 (left) and Type 31(right)

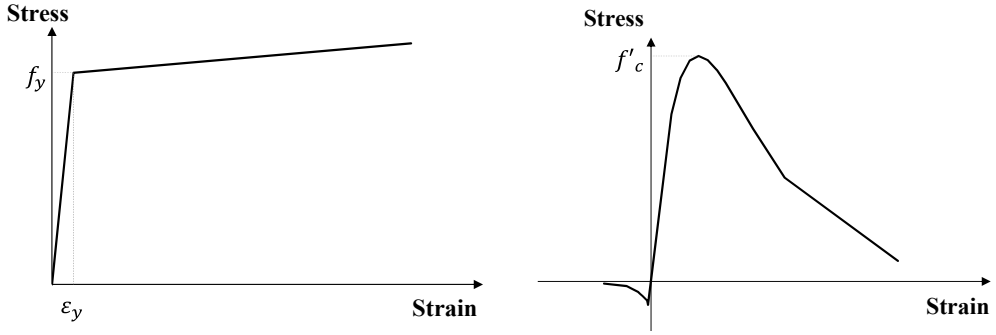

Figure 3-7. Constitutive model of steel (left) and concrete (right)

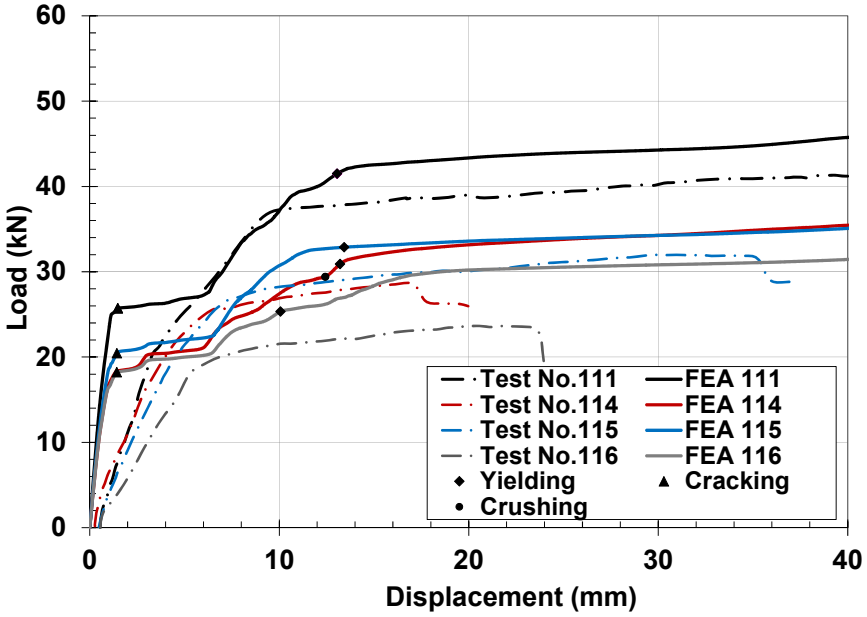

Figure 3-8. Comparison of experimental and FE results for Type 11 beams

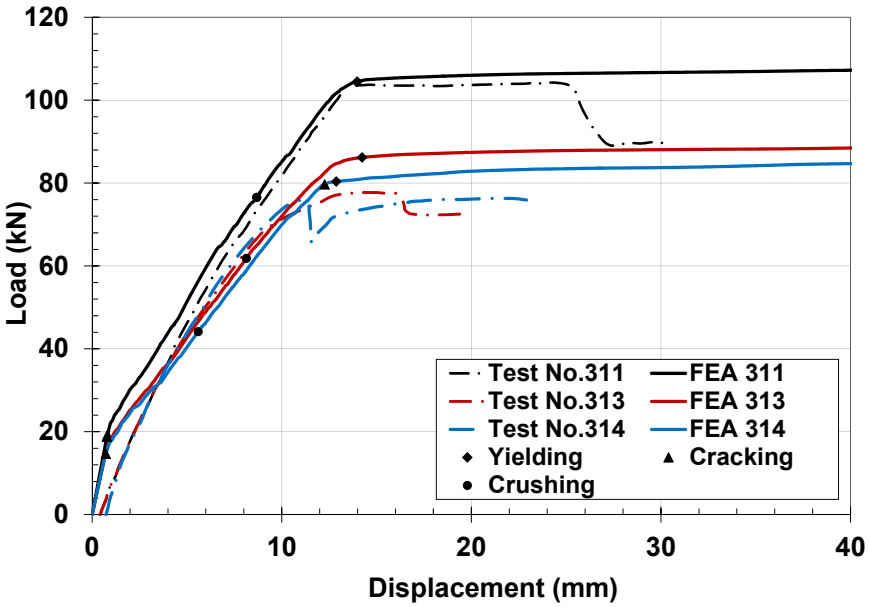

Figure 3-9. Comparison of experimental and FE results for Type 31 beams

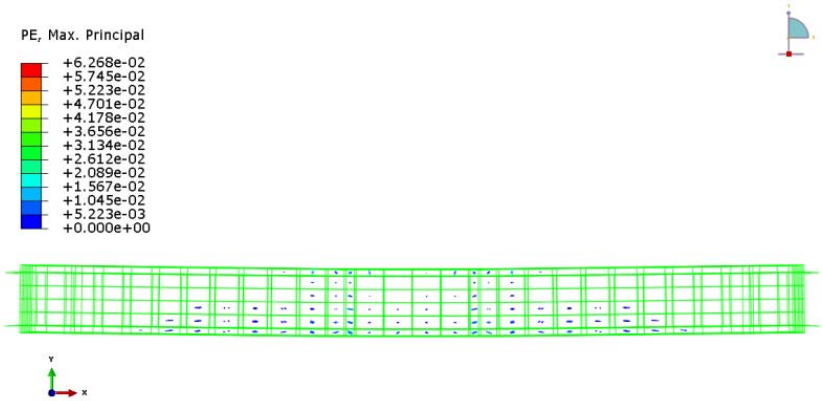

Figure 3-10. Crack pattern of Beam 311 (Pristine)

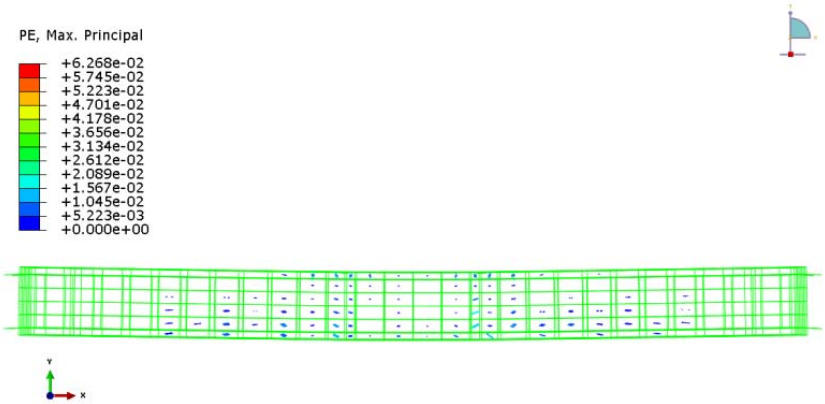

Figure 3-11. Crack pattern of Beam 313 (Low corrosion)

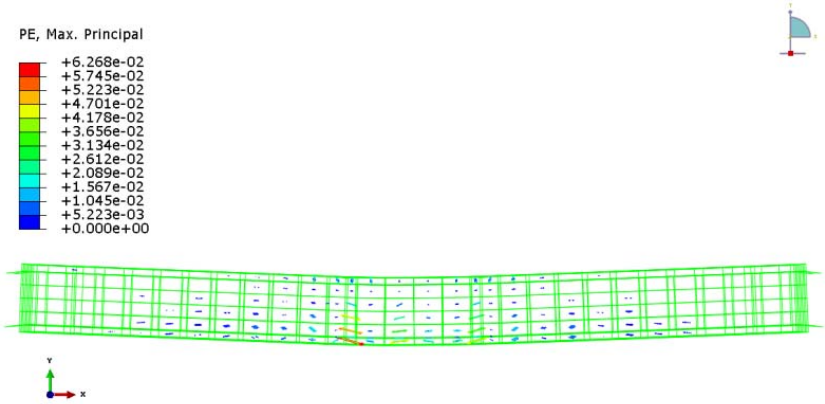

Figure 3-12. Crack pattern of Beam 314 (Medium corrosion)

CHAPTER 4. SEISMIC PERFORMANCE OF REINFORCED CONCRETE STRUCTURAL COMPONENTS IN CORROSIVE ENVIRONMENTS

A paper submitted to the journal of *Structural Engineering (ASCE)*

Zhen Cui, Alice Alipour

4.1 Abstract

Degradation induced by corrosive mechanisms is one of the major issues with the serviceability and strength of the reinforced concrete (RC) structural components. In addition to degrading effects of the corrosion, most of the structures are exposed to one or multiple hazards such as seismic events. This paper studies the structural response of RC columns under earthquake hazards while they are constantly exposed to chloride attack. Chloride-induced corrosion results in a series of degrading mechanisms such as reduction of cross sectional area of steel, reduction of strength and ductility of steel, degradation of concrete material properties, and deterioration of bond. A three dimensional (3D) nonlinear finite element (FE) model is presented to account for all of the degradation mechanisms. The results from a set of experimental tests are used to validate and verify the results from the FE models. Then the extent of structural degradation and its effect on the characteristics of the RC components has been calculated over the entire life of the structure. Two approaches of seismic analysis: equivalent static analysis and nonlinear time history analysis have been conducted to evaluate the seismic performance of corroded columns at multiple time periods during their lifecycle. The location, type, and extent of damage in the columns have been identified under various hazard levels. Furthermore, two different case studies are presented to investigate the seismic performance when different regions of one structural component are subjected to different

corrosion mechanisms due to specific exposure conditions. The results show that corrosion can significantly reduce the seismic capacity of RC members, underlining the necessity of considering it in the design procedure. The outcome of this research will help engineers and inspectors improve their designs, identify necessary test regions and define comprehensive inspection plans, as well as optimize rehabilitation strategies for RC structures under multi-threat areas.

Keywords: seismic performance, corrosion, reinforced concrete, finite element analysis

4.2 Introduction

Reinforced concrete structures are subjected to various natural hazards and environmental stressors during their lifetime. Earthquakes are one of the major natural hazards that impact civil structures, leading to enormous economic loss. Simultaneously, structures are continuously aging and rapidly deteriorating in their lifecycle, becoming increasingly vulnerable to catastrophic failure during probable hazards. The corrosion of reinforcement has been identified as one of the main causes of deterioration for RC structures and could adversely affect the capacity and serviceability of RC structures. Neglecting corrosion effects may significantly overestimate seismic performance of structures in corrosive environments. Therefore, in real conditions, simultaneous effects of both earthquake and corrosion must be taken into account to obtain a more accurate and reliable prediction of the lifetime performance of RC structures.

Significant efforts have been made by researchers to assess seismic structural performance and improve seismic design (Dhakal and Maekawa 2002, Moyer and Kowalsky 2003, Lehman et al. 2004, Spiliopoulos and Lykidis 2006, Duan and Hueste 2012, Baran et al. 2014). Alipour and colleagues have conducted extensive research on corrosion initiation and propagation in RC members and the extent of capacity loss with different corrosion levels (Alipour *et al.* 2012, 2013a and b, Shafei *et al.* 2012 and 2013, Cui and Alipour 2014, Furtado and Alipour 2014, Shafei and Alipour 2015a and b, Klinga and Alipour 2015, Alipour and Shafei 2016a and b, Alipour 2016 and 2017). Other studies have focused on chloride-induced corrosion effects due to reinforcement corrosion in RC structures (Xia *et al.* 2015, Ou *et al.* 2016, Zhang *et al.* 2016). There have been a number of experimental studies focused on cyclic performance of corroded RC members (Ma *et al.* 2012, Ou *et al.* 2012, Meda *et al.* 2014, Guo

et al. 2015) and some research efforts concentrated on assessment of corroded structures under earthquake events. Akiyama *et al.* (2011) investigated displacement ductility capacity and reliability of corroded RC piers under earthquakes using a single degree of freedom pier model and considering only rebar buckling for estimating failure probability. However, due to the limitations of the simplified model, the true demand on bridge pier was not captured. Ou *et al.* (2013) conducted a static analysis to evaluate the seismic capacity of corroded RC bridges assuming that corrosion is only located at column ends. Biondni *et al.* (2015) studied seismic resilience of corroded RC structures using a static analysis. All these studies were conducted using simplified numerical models to obtain overall behaviors, mainly residual capacity (load versus lateral displacement curves), but were not able to capture the details of local damages and energy dissipation. Ghosh *et al.* (2011) estimated seismic loss for corroded RC bridges using a 3D finite element (FE) model but only considered corrosion effects in the forms of steel area loss in columns and degradation in bridge bearings. Inci *et al.* (2013) conducted nonlinear pushover and time history analyses on a corroded RC frame building to assess the seismic performance by updating the damage level using concrete and steel strains. Yalciner *et al.* (2015) assessed the seismic response of a corroded 50-year-old RC building by incremental dynamic analysis only considering two corrosion effects (steel area loss and bond-slip relationship) varying with time. Although these studies were focused on seismic performance of RC structures subjected to chloride-induced corrosion, none of them included all the major deteriorating effects due to reinforcement corrosion or updated all the nonlinear time-dependent parameters with time during the corrosion process. The number of studies that looked into corrosion-induced structural degradation effects from a perspective of analytical or numerical evaluation is very limited (Alipour 2010, Alipour and Shafei 2011 and 2014).

Kashani *et al.* (2014) proposed a fiber-based model to simulate the cyclic behavior of corroded RC columns. However, the model was more focused on the global behavior of the column, such as hysteretic loops and pushover analysis, rather than the local damage extent due to corrosion, such as the extent of concrete local crushing and cover cracking. Furthermore, the study did not consider the effects of corrosion-induced bond deterioration due to the limitations in the developed model.

This paper aims to fill in the gap through development of a detailed 3D nonlinear finite element framework that is able to capture all the chloride-induced corrosion effects, such as reduction of steel cross sectional area, reduction of steel strength and ductility, degradation of concrete properties, and deterioration of bond between concrete and steel. The extent of structural degradation is updated as a function of the age of the structure and is based on realistic estimations of corrosion processes. Moreover, the proposed framework is capable of providing the full details of the region and extent of damage, such as concrete crushing and crack propagation, steel yielding and local bond failure. The percentages of concrete and steel damages are presented based on the FE results and previous standards. The developed FE models have been validated by the previously available experimental test. Both equivalent static analysis and nonlinear time history analysis are performed and the seismic performance of corroded RC structures under different hazard levels at various time periods during their lifecycle are obtained. Furthermore, the variability on the extent of corrosion as it is observed in real life structures is implemented in the model. Two different case studies are presented in this paper to investigate this effect. This study provides a detailed and comprehensive approach to evaluate the seismic performance of corroded RC structures that would increase the

reliability of lifetime performance of the structures to help decision makers prioritize maintenance and rehabilitation strategies for RC structures in the regions with multiple threats.

The paper consists of the following sections: i) corrosion initiation and propagation, ii) effect of corrosion on structural degradation, iii) FE models and model validation, iv) seismic performance of corroded bridge columns using equivalent static and nonlinear time history analyses, and v) two case studies of considering nonuniform levels of corrosion in the structural components.

4.3 Corrosion initiation and propagation

The corrosion of reinforcement is one of the main causes of deterioration of RC structures (Cairns et al. 2005, Val and Chernin 2009, Apostolopoulos et al. 2013). In coastal areas with airborne sea salt particles or in regions with harsh winters and high exposure to deicing salts, chloride-induced corrosion is the dominant mechanism of deterioration. The chloride-induced corrosion is an electrochemical process. The alkaline environment of concrete surrounding reinforcing steel results in the formation of a passive film of iron oxides at the steel surface, which can protect the steel from corrosion. When chloride ions penetrate into the concrete, and reach a threshold concentration value, the PH value changes and the protective film on the reinforcing steel is depassivated and corrosion initiates. After corrosion initiation, steel is consumed and corrosion products (rust) are formed at the interfacial transition zone (ITZ) between the concrete and steel. The expansive rust will gradually fill the ITZ around the steel and then pressurize the surrounding concrete, causing initiation of concrete cracks. After crack initiation, the volume expansion of rust leads to crack propagation and eventually spalling of concrete cover indicating the service failure of structures. In some cases this service failure is also associated with extreme capacity loss and limit state failure. The extent of structural

deterioration caused by chloride-induced corrosion during its lifecycle can be calculated based on the mass loss of steel over time, which is quantified using Faraday's Law. Faraday's Law relates the mass of steel consumed in the corrosion process to the amount of current flow during the electrochemical reaction and has been used extensively in the literature to estimate the steel mass loss over time (Pantazopoulou and Papoulia 2001, EI Maaddawy and Soudki 2007, Lu *et al.* 2011).

$$M_{st}(\mathrm{t}) = \frac{mIt}{zF} \tag{4-1}$$

where m is the atomic mass of iron (56g for Fe), F is Faraday's constant, which is 96500 A·s, z is the ionic charge (for instance, 2 for $Fe \rightarrow Fe^{2+}+2e^{-}$), t is the time after corrosion initiation (s), and I is the current ($I = a_s i_{corr}$ (A), a_s is the surface area of the steel bar, i_{corr} is the current density (A/cm^2)). For a unit length of a rebar, $a_s = \pi d$. Thus, the mass loss of steel per unit length of a rebar for a time step after corrosion initiation, Δt (s), is calculated as:

$$M_{st}(\mathrm{t}) = \frac{m\pi d^r(t)}{zF} i_{corr}\Delta t = 2.894 \times 10^{-4} i_{corr}\pi d^r(t)\Delta t \tag{4-2}$$

where d^r is the residual rebar diameter. In this study, the corrosion rate, i_{corr}, is assumed to be 2 μA/cm^2, which is within the normal range of corrosion rate (Jamali *et al.* 2013). The density of steel is taken as 7.8g/cm^3. Hence, the volume change of consumed steel per unit length can be calculated as follows:

$$A_{st}(\mathrm{t}) = \frac{M_{st}(t)}{\rho_{st}} = 3.709 \times 10^{-10}\pi d^r(t)\Delta t \tag{4-3}$$

The residual diameter of rebar after each time step can be calculated as

$$d^r(t) = \sqrt{d^2 - \frac{4A_{st}(t)}{\pi}} \tag{4-4}$$

Substituting Equation (4-3) to Equation (4-4), the residual rebar diameter at a certain time step can be determined. Thus, the mass loss of steel over time due to corrosion can be determined based on Equation (4-2).

4.4 Effect of corrosion on structural degradation

The effect of chloride-induced corrosion on steel reinforcement can be accounted for by i) reducing the cross sectional area, ii) decreasing yield and ultimate strengths, and iii) enforcing a lower ultimate strain in the constitutive model. Figure1 details out the considered degradation mechanisms and governing numerical equations to calculate them.

The cross sectional area reduction of the steel bar can be calculated using the equation shown in Figure 4-1. In the figure, A^{r}_{st} is the residual cross sectional area of a steel bar, d is the initial diameter of the bar, x_b is the corrosion depth or radius reduction of the bar, and λ_b takes into account the possibility of a one-sided or two-sided corrosion attack penetration since corrosion can occurs in two forms: uniform and pitting corrosion. For uniform corrosion, λ_b is equal to one (Berto *et al.* 2008).

The yield strength and uniform elongation of steel is progressively impaired after corrosion initiation (Apostolopoulos *et al.* 2013). In high levels of corrosion, steel becomes very brittle which can result in sudden rupture of reinforcement and ultimately the structural failure. The residual yield and ultimate strengths, as well as the ultimate strain of corroded reinforcement can be estimated using the empirical formulas in Figure 4-1 (Cairns *et al.* 2005). Here, f_y^r and f_u^r are the residual yield and ultimate strengths of corroded reinforcement, respectively, f_y^0 and f_u^0 are the yield and ultimate strengths of original reinforcement, respectively, ε^r_{su} is the ultimate strain of corroded reinforcement, ε^0_{su} is the ultimate strain of original reinforcement, and η_{100} is the percentage of steel mass loss, calculated from the

consumed steel mass per unit length divided by the initial steel mass per unit length ($\eta_{100}=M_{st}/M_0\times100$). The above formulas were derived based on available experimental data (Du *et al.* 2005a and b), and are consistent with the more recent experimental tests (Kashani *et al.* 2013).

The expansion of rust around the steel rebar exerts internal pressure to the surrounding concrete during the corrosion process and eventually results in cover cracking, spalling or delamination. Although, most corrosion processes start with pitting corrosion, they then develop into uniform corrosion as the corrosion process progresses. Uniform corrosion is known to be the major cause of most of concrete cover spalling compared to pitting corrosion (Berto *et al.* 2008). The corrosion effect on concrete can be considered by the formation of cracks and degradation of compressive strength in concrete cover, as well as a brittle post-peak behavior in the compressive constitutive model of the concrete (Coronelli and Gambarova 2004). The reduced compressive strength of concrete can be calculated using the equations in Figure 1, where ε_c is concrete strain at the compressive strength, f'_c, ε_a is the average tensile strain in cracked concrete perpendicular to the direction of the applied compression, R is a coefficient related to the roughness and diameter of reinforcement (R = 0.1 (Coronelli and Gambarova 2004)), b_0 is the original width of the cross section, b_1 is the increased width due to corrosion cracks, n is the total number of reinforcement in the top layer, w is the total crack width (Molina *et al.* 1993), w_i is the width of each single crack, and λ is the volumetric ratio, which varies depending on the composition of corrosion products. Recent research (Lu *et al.* 2011) shows that the value of the volumetric ratio is around 3.0.

The bond-slip relationship between concrete and steel can be characterized by different stages based on *fib* 2010 (Figure 4-1). At the first stage, there is a nonlinear increase of bond

stress up to the maximum bond strength, $\tau_{b,max}$. Then the decreasing slope indicates the degradation of stiffness which is an indicator of damage progress. Normally under confined conditions, the bond stress remains constant for a certain range of slip. After that, the bond stress will decrease to a much smaller constant level, τ_f. This curve indicates a typical mechanism for pull-out failure (solid line). However, if there is a lack of confinement or a progress in corrosion, the horizontal stage will become inclined with a negative slope representing a splitting failure rather than a pull-out failure (dashed line). The behavior and the mathematical model detailing this is shown in Figure 4-1, where τ_b is bond stress, S is slip, $\tau_{b,max}$ is maximum bond stress, τ_f is the bond stress at the lower constant level (40% of $\tau_{b,max}$), α and S_1~S_3 are the parameters of the model.

Experimental studies of corrosion effects on bond strength of RC members show that reinforcement corrosion has a large impact on the bond strength. At the initial stage of corrosion, the growth of expansive rust increases the roughness of interface between concrete and steel resulting in increased bond strength. As the rust volume further increases with corrosion progress, cracking of surrounding concrete initiates and the bond between steel and concrete deteriorates. However, even at very high levels of corrosion, there is still some residual bond strength remaining. Based on experimental observations, the bond model must be modified accordingly to incorporate the corrosion effects (*fib* 2000). Many researchers have studied the residual bond strength variation with corrosion levels (Val and Chernin 2009, Coronelli and Gambarova 2004, Rodriguez *et al.* 1994). In this study, the bond deterioration model provided by Val and Chernin (2009) has been used (Figure 1). $\tau'_{b,max}$ is the residual bond strength (MPa), $\tau'_{b,max}/\tau_{b,max}$ is the normalized bond strength (the ratio of the residual bond strength of the corroded rebar to that of the pristine rebar), x_{cr} is the corrosion penetration

corresponding to crack initiation in the concrete cover, K_1 is the initial increase of bond strength after corrosion initiation, depending on the confinement level provided by concrete cover and stirrups, K_2 is the rate of bond strength degradation after crack formation, f'_t is the tensile strength of concrete, c/d is concrete cover to bar diameter ratio, a_1 - a_3 are coefficients, obtained by the regression analysis (μm), and ρ is the total area of stirrups within the development length to that of longitudinal reinforcement enclosed by the stirrups.

4.5 Finite element models and model validation

Finite element analysis is used to investigate the seismic response of RC columns under earthquake motions. The results from an experimental test by Ma et al. (2012) have been used to validate the generated FE model results. In the experiment, a total of 13 RC circular columns with different corrosion levels were tested under combined cyclic lateral loadings and constant axial loadings to investigate the behavior of corroded RC columns. The results from the pristine column in the experimental test are used as the baseline to validate the developed FE models of the pristine column. Each column is 260mm in diameter and 1000mm in height with a 1300mm×360mm×400mm stub (Figure 4-2). The clear concrete cover to the spiral stirrups is 30mm. The 28-day compressive strength of the concrete is 32.4MPa. The longitudinal reinforcement in both column and stub is 16mm in diameter. The spirals are 8mm in diameter with a spacing of 100mm. An axial load of 258.03kN is applied on the column. The cyclic loading portfolio applied on the column is provided in Figure 2b. The proposed three dimensional FE model is capable of considering the nonlinearity of both material and geometric properties. It utilizes 3D eight node solid elements for the column concrete and 3D two node truss elements for the reinforcement. The bond-slip interaction between concrete and

steel is modeled via nonlinear spring elements at the interface of solid and truss elements (Cui and Alipour 2016 and 2017). The generated FE model of the column is shown in Figure 4-3.

Damaged plasticity model is selected to model the concrete material. This model considers the degradation of the elastic stiffness induced by plastic straining both in tension and compression, and allows for the control of stiffness recovery effects during cyclic load reversals (ABAQUS 2012). The nonlinear tension stiffening effect after concrete starts cracking can also be included. The reduction of the elastic modulus is expressed in terms of the scalar degradation variable, d_1 (d_c or d_t).

$$E = (1 - d_1)E_0 \tag{4-5}$$

where E_0 is the initial modulus of the concrete and d_1 is the damage variable which could be set as d_c or d_t. d_c and d_t are damage variables for concrete in compression and tension, respectively. When the load changes from tension to compression, tensile cracks tend to close which lets compression stiffness to recover. On the other hand, tension stiffness may not be expected to recover when the load changes from compression to tension once crushing micro-cracks have developed. Compression and tension recovery factors, w_c and w_t, are used to characterize the compression and tension stiffness recovery, respectively (Figure 4-4a). For instance, w_c = 1 and w_t = 0 indicate that concrete regains full compression stiffness but no tension stiffness is recovered. The values of w_c and w_t need to be calibrated during the modeling process to accurately describe the behavior of concrete. Bilinear hardening model is selected for the steel reinforcement. Kinematic hardening, which is capable of simulating the inelastic behavior of steel under cyclic loading is chosen for the FE models (Figure 4-4b).

By using the concrete damaged plasticity model, the number and location of cracked and crushed elements, as well as the extent of tensile and compressive damage can be obtained.

The damage parameters, d_t and d_c, ranges from zero to one. A higher damage (tensile damage, d_t, or compressive damage, d_c) corresponds to a lower stress after concrete reaches tensile or compressive strength and a larger concrete strain. If concrete is still in the elastic range, the damage is equal to zero. If the damage is equal to one, the element experiences complete failure. A cracked element in the rest of this paper refers to an element of which both the maximum principle plastic strain and the tensile equivalent plastic strain are greater than zero, which equivalently means $d_t > 0$.

The cyclic behavior of the FE model of the baseline column is in good agreement with that of the experiment (Figure 4-5). It is observed in the FE model that cracks first occur in the transverse direction in the plastic hinge region (the base of the column) and then continue to propagate as the lateral displacement increases, which is then followed by the crushing of concrete indicating the failure of the column. The observed performance is in full agreement with those reported by Ma *et al.* (2012).

4.6 Performance assessment of corroded bridge columns

After validating the FE model with the experimental tests, nonlinear time history analysis is performed to study the seismic performance of the bridge columns while they are experiencing the degradation from chloride-induced corrosion. The bridge superstructure is modeled with a lumped mass on top of the column. As described in the previous sections, the properties of the bridge columns, such as steel cross sectional area, steel and concrete material properties, and bond-slip relationship degrade since corrosion initiates. The extent of the degradation is calculated according to the equations provided in Figure 4-1 and is calculated based on the steel mass loss over time, which is updated as a function of time according to the procedure outlines in Section 4.2. The structural degradation due to corrosion is calculated at different

ages of the bridge. Three different ages: 0, 20 and 50 years, are selected to evaluate the seismic performance of the bridge columns. The mass losses of the columns at 20 and 50 years are 11.0% and 25.3%, respectively. Pushover analysis has been conducted on the columns at the three ages (Figure 4-6). It can be seen that the capacity and stiffness of the column decrease with the age of the column, i.e. the level of corrosion. The base shear capacity of the pristine column is 50.4kN, and degrades by 20.2% and 42.1% as the column ages to 20 and 50 years, respectively.

Three approaches are recommended in AASHTO LRFD for seismic design of bridges: Equivalent Static Analysis (ESA), Elastic Dynamic Analysis (EDA) and Nonlinear Time History Method (NTHA) (AASHTO 2011). Equivalent Static Analysis and linear Elastic Dynamic Analysis are appropriate for estimating the displacement demands for normal bridges and their individual components. The ESA is the simplest method among the three methods, which reduces computational cost and is easy for engineers to apply to practice. It is suitable for short to medium span bridges with regular configuration. For bridges where ESA does not provide an adequate level of sophistication to estimate the dynamic behavior, EDA should be used. However, EDA does not represent the inelastic behavior of earthquake resisting elements under strong ground motions. NTHA is the most comprehensive analysis method among the three methods since the effect of inelastic behavior is included. It is used for critical and essential bridges or normal bridges with SDC D (the Seismic Design Category D).

To give a comprehensive analysis for the bridge components located in high seismic areas, both the simplest and the most comprehensive methods: ESA and NTHA are selected in this study to investigate the seismic performance of the intact and corroded bridge columns. The variation of the structural responses under different ground motions and the comparison

of the results between ESA and Nonlinear Time History Analysis are also presented in this study.

In ESA, a uniform lateral load is used to approximate the effect of seismic loads and the displacement demands. For this case, a lateral load (equivalent static load) is applied to the top of the column to simulate the effects of seismic loads. Figure 4-7 shows the procedure of calculating the lateral load according to AASHTO. Three earthquake hazard levels 2% and 10% probability of exceedance (PE) in 50 years (Named as EQ 2% and EQ 10% hereafter), and 7% in 75 years (Named EQ 7%), which is the design earthquake in the current AASHTO specifications (AASHTO 2011), are considered in this study. With EQ 2% in 50 years, the equivalent static load is 50.6kN and the lateral displacement at the top of the pristine column is 30.2mm. With EQ 10% in 50 years, the equivalent static load is 39.7kN and the lateral displacement at the top of the pristine column is 7.6mm. With EQ 7% in 75 years, the equivalent static load is 46.4kN and the lateral displacement at the top of the pristine column is 12.8mm.

To perform nonlinear time history analysis, three earthquake ground motions with probability of exceedance of 2% and 10% in 50 years, and 7% in 75 years are selected from the ground motions that are originally recorded for Los Angeles area (Somerville *et al.* 1997) (Figure 4-8a). The selected three earthquakes have the annual probability of exceedance of 4.0×10^{-4}, 2.1×10^{-3} and 9.7×10^{-4}, respectively. The peak ground accelerations (PGAs) of the ground motions are 0.7g, 0.4g, and 0.5g, respectively. Nonlinear time history analysis is performed for the column at 0, 20 and 50 years under the three hazard levels EQ 2%, 7% and 10%, respectively, to study the seismic performance of the bridge columns under different levels of corrosion. The maximum relative lateral displacement of the pristine column under

EQ 2% is 32.0mm, which is similar to the lateral displacement of 30.2mm under the equivalent static load of 50.6kN. The maximum relative lateral displacement of the pristine column under EQ 7% is 13.1mm. The maximum relative lateral displacement of the pristine column under EQ 10% is 6.4mm.

Figure 4-9 presents the hysteresis loops developed at the column base. It can be observed that while the pristine column stays in the elastic range for the EQ 10%, the formation of corrosion degradation under the same earthquake results in a slight plasticity at the base. Comparing this with the EQ 2% that represents a major hazard level, more energy dissipation is observed at the base of the pristine column. Additionally with the increase in the level of corrosion-induced degradation, large permanent displacement could be observed that push the column into a new balance point. The energy dissipated during EQ 2% for the column at 0, 20 and 50 years are calculated using a user defined code in MATLAB (2014), and are 14099J, 11734J and 11716J, respectively. As one can see, the energy absorbed by the structure in the 20 years and 50 years is similar however, due to the impact of corrosion, large damage to the concrete and the steel rebar are expected in the 50 year old column that can result in the larger permanent deformations. A similar trend could be observed for the column EQ 7% where the energy dissipated for the 20 and 50 year columns are similar but the extra flexibility in the older column result in larger displacement, pinching in the hysteresis loop, and also lower base shear capacity.

The uncertainty associated with the variation of ground motion is taken into account analyzing the aged structural components under a suite of different ground motions representing the hazard of 7% in 75 years. Ground motions were selected from the PEER database to match the target spectrum. Figure 4-10 shows the spectral acceleration of the

selected ground motions. The variation on the maximum relative lateral displacements at the top of the column at different ages and under the set of ground motions are shown in Figure 4-11. The lateral displacements at 0, 20 and 50 years follow lognormal distributions, respectively, with a standard deviation of 5.7mm, 6.6mm and 14.5mm. The standard deviation increases with the age of the column, indicating with the higher corrosion levels, the displacements are more scattered. This is due to the uncertainty associated with the parameters of the corroded columns.

The type and extent of damage can be obtained by the FE analysis using the concrete damage plasticity model and bilinear hardening steel model. The type of damage in the column includes the cracking and crushing of concrete and the yielding of steel reinforcement. It is observed in the FE models that cracks first occur in the transverse direction at the bottom of the column then continue to propagate towards the upper portions of the column. Figure 12 illustrates the crack propagation process of the column at 0 and 20 years under EQ 10%. Different time steps t = 10, 13.5, 17, 30 and 79.98 seconds are considered based on the major changes observed in the time history of the ground motion as shown by the time stickers on Figure 8a. It can be seen that the cracks first occur transversely at the bottom of the column (t=10s), then start to propagate towards the top (t=13.5s). After the peak accelerations, much more cracks are observed in the column (t=17s). Comparing the crack propagation pattern of the column at 0 year with the column at 20 years under EQ 10% more severe concrete tensile damage is observable. The crushed concrete elements also first appear at the bottom of the column. Yielded steel elements are mainly observed at the bottom where the plastic hinge forms and the highest plastic strain is observed in the longitudinal reinforcement at the plastic hinge (Figure 4-12).

To elaborate on the mechanisms that result in propagation of cracks in concrete and the yielding of steel, Figure 4-13 shows the percentage of damaged concrete elements and number of yielded steel elements in the columns with three different ages. The tensile or compressive damage in the concrete elements are estimated by tracking d_t and d_c (concrete is damaged when $d_t > 0$ or $d_c > 0$) and the number of yielded steel elements is estimated by tracking the plastic strain. It can be seen that under the severe earthquake EQ 2%, with the increase of the corrosion level, the concrete damage decreases and the steel damage increases. The reason is that when the column is corroded, both the strength and ductility of the steel are decreased and the steel section area is significantly reduced (by 11.0% and 25.3% in 20 and 50 years, respectively). The heavily corroded column has very low amount of degraded reinforcement causing a large amount of steel yields fast at the column base with less warning of concrete cracks propagating towards the top. It is observed that in the corroded columns, most of the steel at the bottom region yield with severe concrete damage concentrated at the base but with less cracks propagating towards the top. The column may result in a more brittle failure.

Under the design earthquake EQ 7%, similarly, the percentage of concrete damage decreases and the percentage of steel damage increases when the level of corrosion increases. But both of the concrete and steel damage percentages are reduced compared to those under EQ 2%, since the severity of the earthquake is reduced. Under the least severe earthquake EQ 10%, the percentage of the damaged concrete elements increases from 0 year to 20 years but decreases from 20 years to 50 years. Only four steel elements are yielded in the pristine column. The pristine column is almost still in the elastic range. This explains the reason for increase in number of damaged concrete elements from 0 to 20 years. The percentages of yielded steel elements are 4.5% and 8.3% for the column at 20 and 50 years, respectively. More yielded

steel elements and less cracked and crushed concrete elements in the column at 50 years indicates the more brittle behavior of the column with 50 years exposure to corrosive environment.

4.7 Case studies representing non uniform corrosion

Some RC columns are located in more aggressive areas, such as highway bridge columns right next to the road shoulders or those at the basement of a building. Often time these columns are exposed to an uneven amount of intrusive chemicals that can accelerate the corrosion. For example, for the bridge columns right next to the highway shoulders, more exposure to deicing ice is expected as they are closer to the splash zone of the traffic zone and more likely to get in touch with the salt-laden snow that snowplows pile next to them. In such situations, the bottom region of the column is exposed to a more surface chloride content and is more likely to have corrosion initiated faster and propagate in a higher speed. A similar situation could be observed in the columns at the basement of a building, such as at the parking garage, where there is a higher likelihood of salty water exposure. On the other hand in a seismic regions, these columns are expected to undergo large earthquake induced demand and the additional corrosion created at the bottom region –where most of the time the plastic hinges are exposed to form- will jeopardize the seismic performance of the columns and the structure as a whole. To investigate the behavior of the column when it experiences inconsistent levels of corrosion throughout its cross section and length. Two case study columns that represent the above situations are presented in this section.

Case I is when both sides of the lower one third of the column height at 20 years is exposed to more chloride and hence experiences a higher corrosion rate (Case I-1: $i = 5\mu A/cm^2$ and Case I-2: $i = 10\mu A/cm^2$) and the rest of the column is subjected to a corrosion rate of

$2\mu A/cm^2$. Case II is when only one side of the lower one third of the column height at 20 years experiences a higher corrosion rate: (Case II-1: $i = 5\mu A/cm^2$ and Case II-2: $i = 10\mu A/cm^2$). The rest of the column is subjected to a corrosion rate of $2\mu A/cm^2$ (Figure 4-14). Nonlinear time history analysis is performed for these four cases and the results compared with the column at 0, 20 and 50 years are shown in Figures 4-15-16.

Under EQ 2%, in Case I-1- 20 years when both sides of the column lower section are under a higher corrosion rate of $5\mu A/cm^2$, the capacity of the column is reduced to 76.2% of the column capacity at 20 years with uniform corrosion and the maximum relative lateral displacement is 2.1 times as large as that of the column at 20 years with uniform exposure. If comparing the seismic response of the column in Case I-1 and at 50 years, it can be seen that the capacity in Case I-1 is similar to that in 50 years and the maximum relative lateral displacement in Case I-1 reaches 92.3% of that at 50 years. Therefore, it can be known that when the critical lower section of the column experiences a higher corrosion rate, the seismic capacity of the column is significantly reduced and the column undergoes a much greater maximum lateral displacement indicating higher extent of plasticity and damage. A similar trend is observed in Case I -2 when the critical lower section experiences a much higher corrosion rate of $10\mu A/cm^2$ at 20 years. The capacity of this 20 year old column in Case I - 2 is lower than that of the column at 50 years. This may alert designers, inspectors and maintenance teams to pay special attention to the regions of the structural components that are expected to perform during a seismic event requiring certain protection measures or special designs for these locations.

It can be known from Case II that when only one side of the column lower section experiences a higher corrosion rate, the seismic capacity of the column is decreased and the

greater maximum relative displacement indicates higher extent of plasticity and damage compared to the column at same age undergoing a consistent corrosion level, although the columns with both sides of the base are subjected to that higher corrosion rate perform even worse. The reason is that under both EQ 10% and 2%, in Case I-2 and II-2, many of longitudinal steel elements at the base already reach their ultimate strains (observed from FE results), the longitudinal reinforcement of the columns are expected to rupture with large areas of concrete spalling at the base, resulting complete failure in those columns. Even for Case I-1 and Case II-1 under EQ 10% and 2%, the maximum normalized steel strains are very high (0.8-0.9). Some of longitudinal steel elements at column base experience such high strains. The longitudinal reinforcement of these columns are very likely to rupture. Simultaneously, noticed from FE results, the steel strains of the spirals at the column bases in the four cases are very high, compared to the columns experiencing the consistent corrosion rates at 20 and 50 years, particularly for Case I-2 and Case II-2 under EQ 10%, as well as all the four cases under EQ 2%. In Case I-2 and Case II-2 under both EQ 10% and 2%, some of the spiral steel elements at the base already reach their ultimate strains. The bottom region of the spirals will rupture, leading to failure of the confinement in plastic hinge zone of the column. In Case I-1 and II-1 under EQ 2%, some of the spiral elements at the base experience high strains. The maximum normalized steel strains of the spirals are 0.6 and 0.7, respectively. In Case I-1 and II-1 under EQ 10%, although the spiral strains at the bottom are lower than that under EQ 2%, they are still much higher compared to the column experiencing the uniform corrosion rate at 20 years or even 50 years. Therefore, it can be known that when the critical section of the column experiences a higher corrosion risk, the column tends to fail due to lack of confinement at the critical location caused by corrosion-induced reinforcement degradation. Such columns are in

a critical situation and special attention must be drawn to them to prevent failure during seismic events.

4.8 Conclusions

This paper provides a multi-threat approach that assesses the lifetime performance of RC columns under both earthquake and chloride-induced corrosion. The corrosion effects such as steel area, strength and ductility reduction, concrete degradation, and bond deterioration have been implemented into the developed 3D FE models and updated according to different ages of the RC column. The capacity and stiffness of the column at different ages are evaluated and found to be significantly reduced by the level of corrosion. The seismic performance of the columns at 0, 20 and 50 years under three different hazard levels is investigated. The type, location, and extent of damage in the column at different corrosion levels have been identified. Crack propagation patterns in the concrete cover are visualized. Furthermore, the seismic performance of the columns that experience a higher corrosion risk on one or both sides of the critical bottom region has also been studied. It can be concluded that a much higher corrosion risk at the critical lower section of the column can dramatically compromise the seismic performance of the column, leading to complete failure under severe earthquakes. The longitudinal reinforcement at the bottom of these columns is very likely to rupture together with very high strains in the spirals and large areas of concrete spalling at the bottom regions. Such columns tend to fail due to lack of confinement at the critical location caused by corrosion-induced reinforcement degradation. These columns could perform much worse than a column undergoing a uniform corrosion rate at a much older age and must be drawn special attention to in order to prevent failure during seismic events. The findings of this study highlight the necessity of studying the combined effects of earthquake and corrosion in seismic

prone regions. The proposed framework is capable of predicting the seismic performance of RC columns with different corrosion levels at any age during their lifecycles and providing the details of damage extent, type and region, therefore, will help engineers improve their designs, identify necessary test regions, and comprehensive test plans, and optimize the rehabilitation strategies for RC structures in multi-threat areas.

4.9 References

ABAQUS 6.12 Documentation. Dassault Systèmes Simulia Corp, 2012.

Akiyama, M., Frangopol, D., and Matsuzaki, H. Life-cycle reliability of RC bridge piers under seismic and airborne chloride hazards. *Journal of Earthquake Engineering and Structural Dynamics*, Vol. 40, 2011, pp. 1671-1687.

Alipour, A. Life-cycle performance assessment of highway bridges under multi-hazard conditions and environmental stressors. Ph.D. Dissertation, Department of Civil and Environmental Engineering, University of California, Irvine, CA, 2010.

Alipour, A. Post-Extreme Event Damage Assessment and Response for Highway Bridges. National Cooperative Highway Research Program (NCHRP) Synthesis, 2016.

Alipour, A. Enhancing Resilience of Bridges to Extreme Events by Rapid Damage Assessment and Response Strategies. *Transportation Research Board 96th Annual Meeting Transportation Research Board 2017*, Washington, D.C.

Alipour, A., and Shafei, B. Structural vulnerability measures for assessment of deteriorating bridges in seismic prone areas. *Maintenance and Safety of Aging Infrastructure*, edited by Dan Frangopol and Yiannis Tsompanakis, Chapter 3, CRC Press, 2014.

Alipour, A., and Shafei, B. (a) Seismic resilience of transportation networks with deteriorating components. *Journal of Structural Engineering*, Vol. 142, No. 8, 2016, C4015015.

Alipour, A., and Shafei, B. (b). Assessment of Postearthquake Losses in a Network of Aging Bridges. *Journal of Infrastructure Systems*, Vol. 22, No. 2, 2016, 04015023.

Alipour, A., Shafei, B., and Shinozuka, M. Performance evaluation of deteriorating highway bridges located in high seismic areas. *Journal of Bridge Engineering*, Vol. 16, No. 5, 2011, pp. 597-611.

Alipour, A., Shafei, B., and Shinozuka, M. A multi-hazard framework for optimum life-cycle cost design of reinforced concrete bridges. *Structural Seismic Design Optimization and Earthquake Engineering*, 2012, pp. 76-104.

Alipour, A., Shafei, B., and Shinozuka, M. (a) Capacity loss evaluation of reinforced concrete bridges located in extreme chloride-laden environments. *Journal of Structure and Infrastructure Engineering*, Vol. 9, No. 1, 2013, pp. 8-27.

Alipour, A., Shafei, B., and Shinozuka, M. (b). Reliability-based calibration of load and resistance factors for design of RC bridges under multiple extreme events: Scour and earthquake. *Journal of Bridge Engineering*, Vol. 18 No. 5, 2013, pp. 362-371.

American Association of State Highway and Transportation Officials. AASHTO Guide Specifications for LRFD Seismic Bridge Design, 2011.

Apostolopoulos, C. A., Demis, S., and Papadakis, V. G. Chloride-induced corrosion of steel reinforcement - Mechanical performance and pit depth analysis. *Journal of Construction and Building Materials*, Vol. 38, 2013, pp. 139-146.

Baran, E., Mertol, H., and Gunes, B. Damage in reinforced-concrete Buildings during the 2011 Van, Turkey, Earthquakes. *Journal of Engineering Failure Analysis*, Vol. 28, No. 3, 2014, pp. 466-479.

Biondni, F., Camnasio, E., and Titi, A. Seismic resilience of concrete structures under corrosion. *Journal of Earthquake Engineering and Structural Dynamics*, Vol 44, 2015, pp. 2445-2466.

Berto, L., Simioni, P., and Saetta, A. Numerical modeling of bond behavior in RC structures affected by reinforcement corrosion. *Journal of Engineering Structures*, Vol. 30, No. 5, 2008, pp. 1375-1385.

Cairns, J., Plizzari, G. A., Du, Y., Law, D. W., and Franzoni, C. Mechanical properties of corrosion-damaged reinforcement. *ACI Material Journal*, Vol. 102, No. 4, 2005, pp. 256-264.

Coronelli, D., and Gambarova, P. Structural assessment of corroded reinforced concrete beams: Modeling Guidelines. *Journal of Structural Engineering*, Vol. 130, No. 8, 2004, pp. 1214-1224.

Cui, Z., and Alipour, A. A detailed finite-element approach for performance assessment of corroded reinforced concrete beams. *ASCE Structures Congress 2014*, Boston, Massachusetts, April 3-5.

Cui, Z., and Alipour, A. Performance assessment of corroded highway bridge piers under cyclic loading. *Proceedings of Transportation Research Board (TRB) 95th Annual Meeting 2016*, Washington, D.C.

Cui, Z., and Alipour, A. Seismic Performance of Highway Bridge Columns in Corrosive Environments. *Proceedings of Transportation Research Board 96th Annual Meeting Transportation Research Board 2017*, Washington, D.C.

Dhakal, R. P., and Maekawa, K. Reinforcement stability and fracture of cover concrete in reinforced concrete members. *Journal of Structural Engineering*, Vol. 128, No. 10, 2002, pp. 1253-1262.

Du, Y.G., Clark, L.A., and Chan, A.H.C. (a). Residual capacity of corroded reinforcing bars. *Magazine of Concrete Research*, Vol. 57, No. 3, 2005, pp. 135-147.

Du, Y.G., Clark, L.A., and Chan, A.H.C. (b). Effect of corrosion on ductility of reinforcing bars. *Magazine of Concrete Research*, Vol. 57, No. 7, 2005, pp. 407-419.

Duan, H., and Hueste, M. Seismic performance of a reinforced concrete frame building in China. *Journal of Engineering Structures*, Vol. 41, 2012, pp. 77-89.

El Maaddawy, T., and Soudki, K. A model for prediction of time from corrosion initiation to corrosion cracking. *Journal of Cement and Concrete Composites*, Vol. 29, No. 3, 2007, pp. 168-175.

fib (2000). *Bond of reinforcement in concrete*. State-of-art report, fib Bulletin No. 10.

fib. *Model Code*. International Federation for Structural Concrete, Switzerland, 2010.

Furtado, M.N., and Alipour, A. Estimation of direct and indirect losses in transportation networks due to seismic events. *Transportation Research Board 93rd Annual Meeting 2014*, Washington, D.C.

Ghosh, J., and Padgett, J. Probabilistic seismic loss assessment of aging bridges using a component-level cost estimation approach. *Journal of Earthquake Engineering and Structural Dynamics*, Vol. 40, 2011, pp. 1743-1761.

Guo, A., Li, H., Ba, X., Guan, X., and Li, H. Experimental investigation on the cyclic performance of reinforced concrete piers with chloride-induced corrosion in marine environment. *Journal of Engineering Structures*, Vol. 105, 2015, pp. 1-11.

Inci, P., Goksu, C., Llki, A., and Kumbasar, N. Effects of reinforcement corrosion on the performance of RC frame buildings subjected to seismic actions. *Journal of Performance of Constructed Facilities*, Vol. 27, No. 6, 2013, pp. 683-696.

Jamali, A., Angst, U., Adey, B., and Elsener, B. Modeling of corrosion-induced concrete cover cracking: A critical analysis. *Journal of Construction and Building Materials*, Vol 42, 2013, pp. 225-237.

Klinga, J. V., Alipour, A. Assessment of structural integrity of bridges under extreme scour conditions. *Engineering Structures*, Vol. 82, 2015, pp. 55-71.

Kashani, M. M., Crewe, A. J., and Alexander, N. A. Nonlinear stress–strain behaviour of corrosion-damaged reinforcing bars including inelastic buckling. *Journal of Engineering Structures*, Vol. 48, 2013, pp. 417-429.

Kashani, M., Crewe, A., Alexander, N., and Lowes, L. Modeling nonlinear behavior of corrosion damaged RC bridges piers subject to cyclic loading. *Life-Cycle of Structural Systems: Design, Assessment, Maintenance and Management*. Taylor and Francis Group, London, 2014.

Lehman, D., Moehle, J., Mahin, S., Calderone, A., and Henry, L. Experimental evaluation of the seismic performance of reinforced concrete bridge columns. *Journal of Structural Engineering*, Vol. 130, No. 6, 2004, pp. 869-879.

Lu, C., Jin, W., and Liu R. Reinforcement corrosion-induced cover cracking and its time prediction for reinforced concrete structures. *Journal of Corrosion Science*, Vol. 53, No. 4, 2011, pp. 1337-1347.

Ma, Y., Che, Y., and Gong, J. X. Behavior of corrosion damaged circular reinforced concrete columns under cyclic loading. *Journal of Construction and Building Materials*, Vol. 29, 2012, pp. 548-556.

MATLAB R2014b. The MathWorks, Inc., 2014.

Meda, A., Mostosi, S., Rinaldi, Z., and Riva, P. Experimental evaluation of the corrosion influence on the cyclic behaviour of RC columns. *Journal of Engineering Structures*, Vol. 76, 2014, pp. 112-123.

Molina, F.J., Alonso, C., and Andrade, C. Cover cracking as a function of rebar corrosion: Part 2 - numerical model. *Journal of Materials and Structures*, Vol. 26, 1993, pp. 532-548.

Moyer, M. J., and Kowalsky, M. J. Influence of tension strain on buckling of reinforcement in concrete columns. *ACI Structural Journal*, Vol. 100, No. 1, 2003, pp. 75-85.

Rodriguez, J., Ortega, L., and Garcia, A. Corrosion of reinforcing bars and service life of reinforced concrete structures: Corrosion and bond deterioration. *In: Proceedings, International Conference on Concrete across Borders*, Vol. 2, 1994, pp. 315-326.

Shafei, B., Alipour, A., and Shinozuka, M. Prediction of corrosion initiation in reinforced concrete members subjected to environmental stressors: A finite-element framework. *Journal of Cement and Concrete Research*, Vol. 42, No. 2, 2012, pp. 365-376.

Shafei, B., Alipour, A., and Shinozuka, M. A stochastic computational framework to investigate the initial stage of corrosion in reinforced concrete superstructures. *Journal of Computer-Aided Civil and Infrastructure Engineering*, Vol. 28, No. 7, 2013, pp. 482-494.

Shafei, B., and Alipour, A. (a). Estimation of Corrosion Initiation Time in Reinforced Concrete Bridge Columns: How to Incorporate Spatial and Temporal Uncertainties. *Journal of Engineering Mechanics*, 2015.

Shafei, B., and Alipour, A. (b). Application of large-scale non-Gaussian stochastic fields for the study of corrosion-induced structural deterioration. *Journal of Engineering Structures*, Vol. 88, 2015, pp. 262-276.

Somerville, P., Smith, N., Punyamurthula, S., and Sun, J. Development of ground motion time histories for Phase 2 of the FEMA/SAC steel project. SAC/BD-97/04, FEMA/SAC, 1997, Sacramento, CA.

Spiliopoulos, K., and Lykidis, G. An efficient three-dimensional solid finite element dynamic analysis of reinforced concrete structures. *Journal of Earthquake Engineering and Structural Dynamics*, Vol. 35, 2006, pp. 137-157.

Ou, Y., Tsai, L., and Chen, H. Cyclic performance of large-scale corroded reinforced concrete beams. *Journal of Earthquake Engineering and Structural Dynamics*, Vol. 41, 2012, pp. 593-604.

Ou, Y., Fan, H., and Nguyen, N. Long-term seismic performance of reinforced concrete bridges under steel reinforcement corrosion due to chloride attack. *Journal of Earthquake Engineering and Structural Dynamics*, Vol. 42, 2013, pp. 2113-2127.

Ou, Y., Susanto, Y., Roh, H. Tensile behavior of naturally and artificially corroded steel bars. *Journal of Construction and Building Materials*, Vol. 103, 2016, pp. 93-104.

Pantazopoulou, S. J., and Papoulia, K. D. Modeling cover cracking due to reinforcement corrosion in RC structures. *Journal of Engineering Mechanics*, Vol. 127, No. 4, 2001, pp. 342-351.

Val, D., and Chernin, L. Serviceability reliability of reinforced concrete beams with corroded reinforcement. *Journal of Structural Engineering*, Vol. 135, No. 8, 2009, pp. 896-905.

Xia, J., Jin, W., and Li, L. Performance of corroded reinforced concrete columns under the action of eccentric loads. *Journal of Materials in Civil Engineering*, Vol. 28, No. 1, 2015.

Yalciner, H., Sensoy, S., and Eren, O. Seismic performance assessment of a corroded 50-year-old reinforce concrete building. *Journal of Structural Engineering*, Vol. 27, No. 6, 2015, pp. 683-696.

Zhang, X., Wang, L., Zhang, J., and Liu, Y. Bond degradation–induced incompatible strain between steel bars and concrete in corroded RC beams. *Journal of Performance of Constructed Facilities*, 2016.

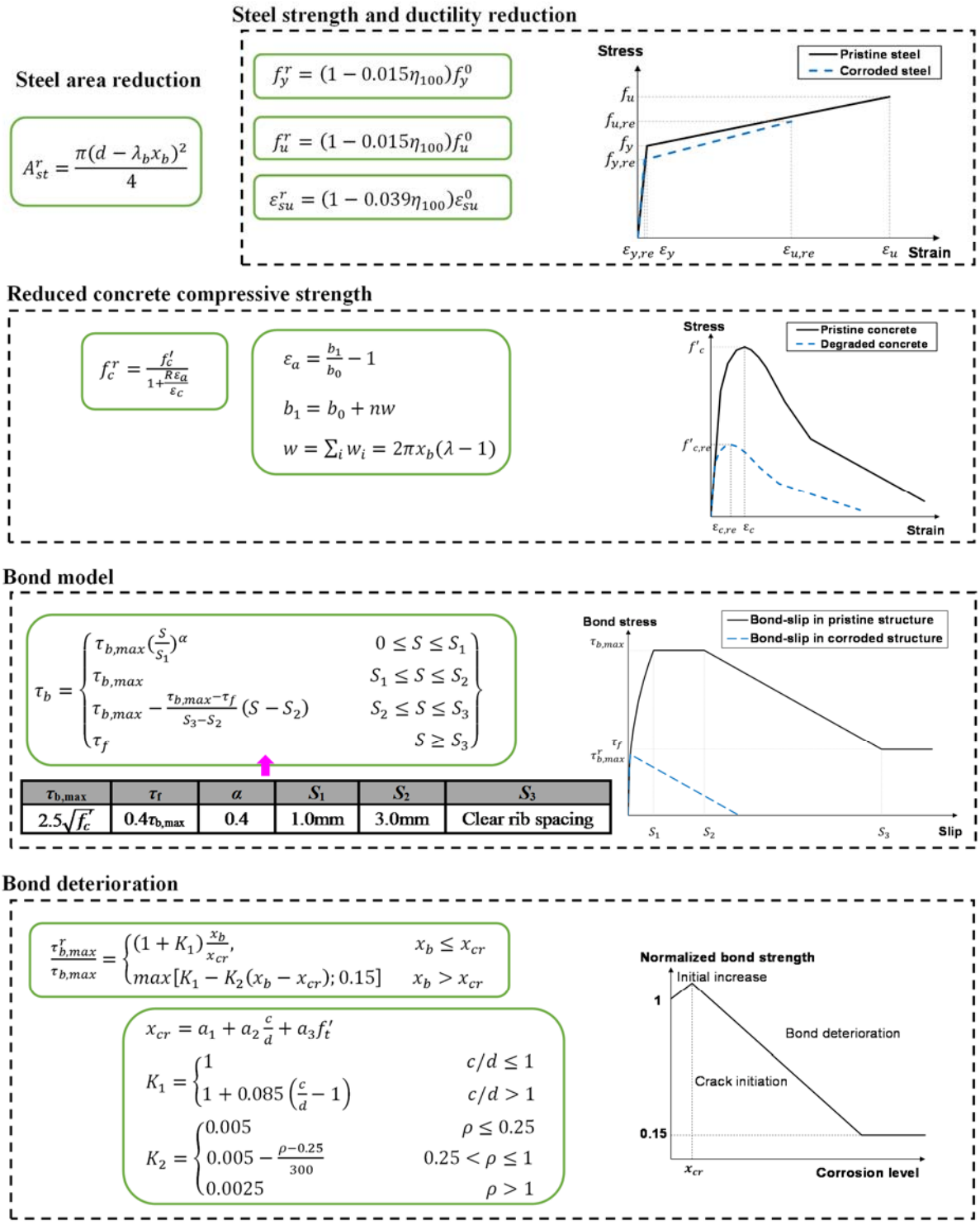

$\tau_{b,max}$	τ_f	α	S_1	S_2	S_3
$2.5\sqrt{f_c^r}$	$0.4\tau_{b,max}$	0.4	1.0mm	3.0mm	Clear rib spacing

Figure 4-1. Procedure to estimating the deteriorating effects of different mechanisms.

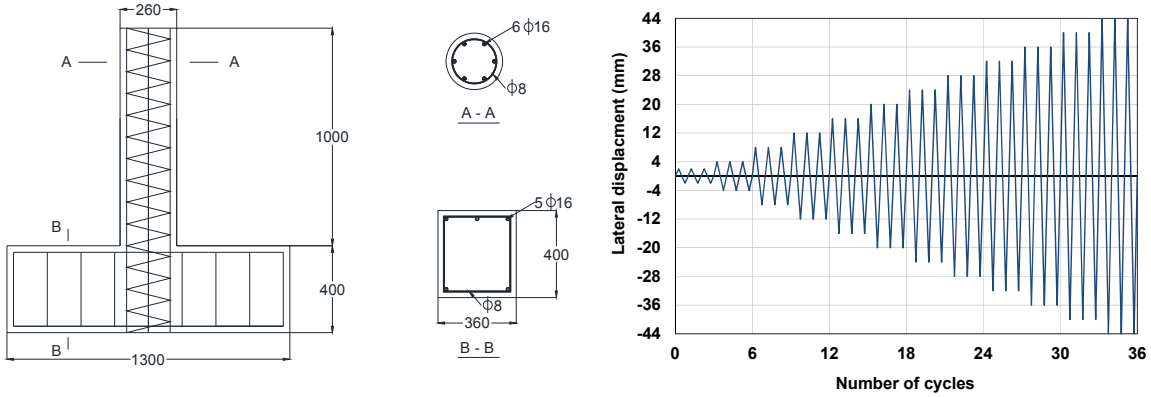

(a) **(b)**

Steel properties	Longitudinal reinforcement	Transverse reinforcement
Diameter (mm)	16	8
Yield strength (MPa)	373.2	327
Ultimate strength (MPa)	572.3	510.7

(c)

Figure 4-2. (a) Structural details of the column from the experiment (all dimensions in mm); (b) cyclic loading portfolio; (c) reinforced properties of the column.

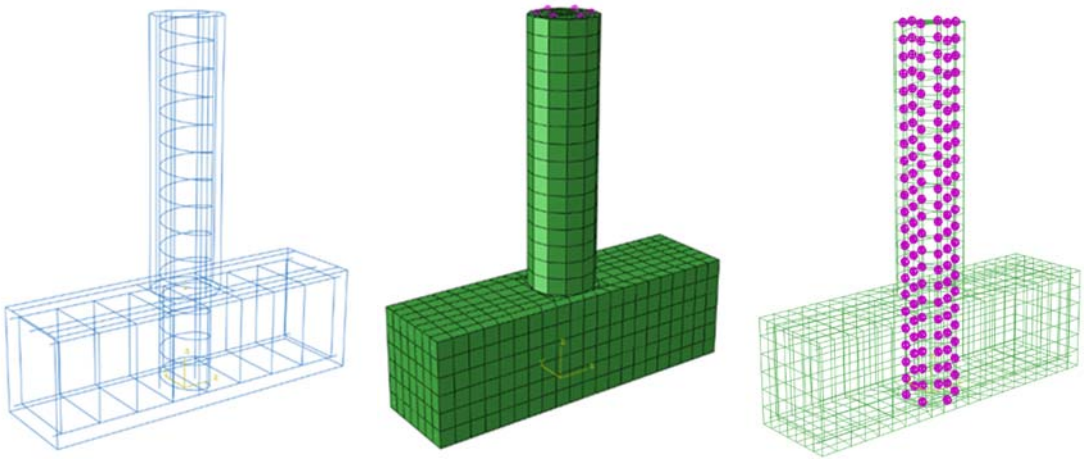

Figure 4-3. FE model generated based on characteristics of the column in the experiment.

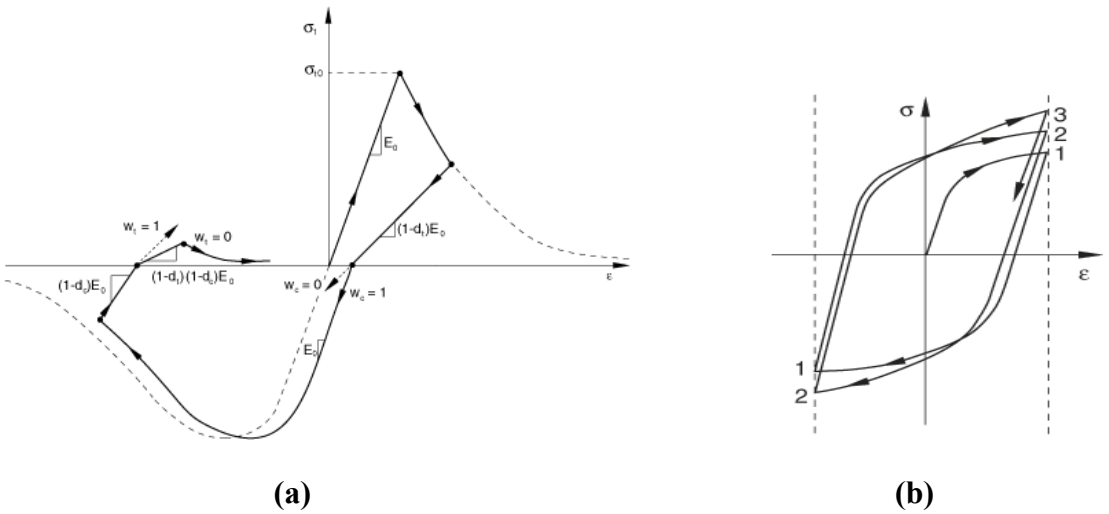

(a) (b)

Figure 4-4. Cyclic behaviors of (a) concrete and (b) steel (ABAQUS 2012).

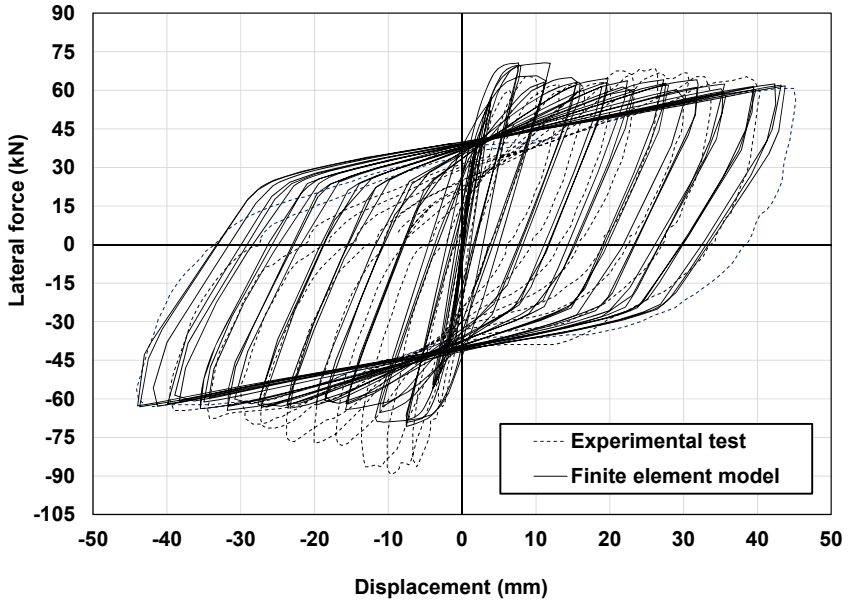

Figure 4-5. Comparison of hysteresis loops developed in experiment and 3D finite element model for the baseline column.

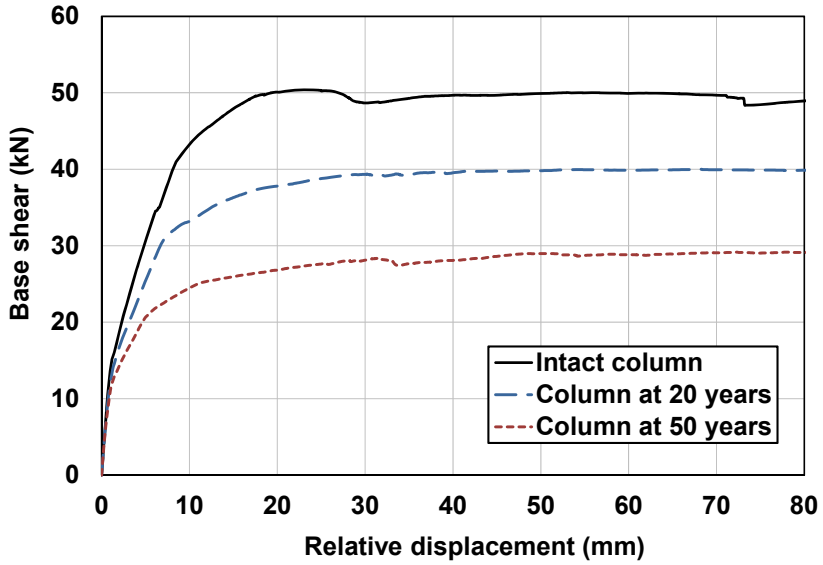

Figure 4-6. Pushover analysis of the bridge columns at 0, 20 and 50 years.

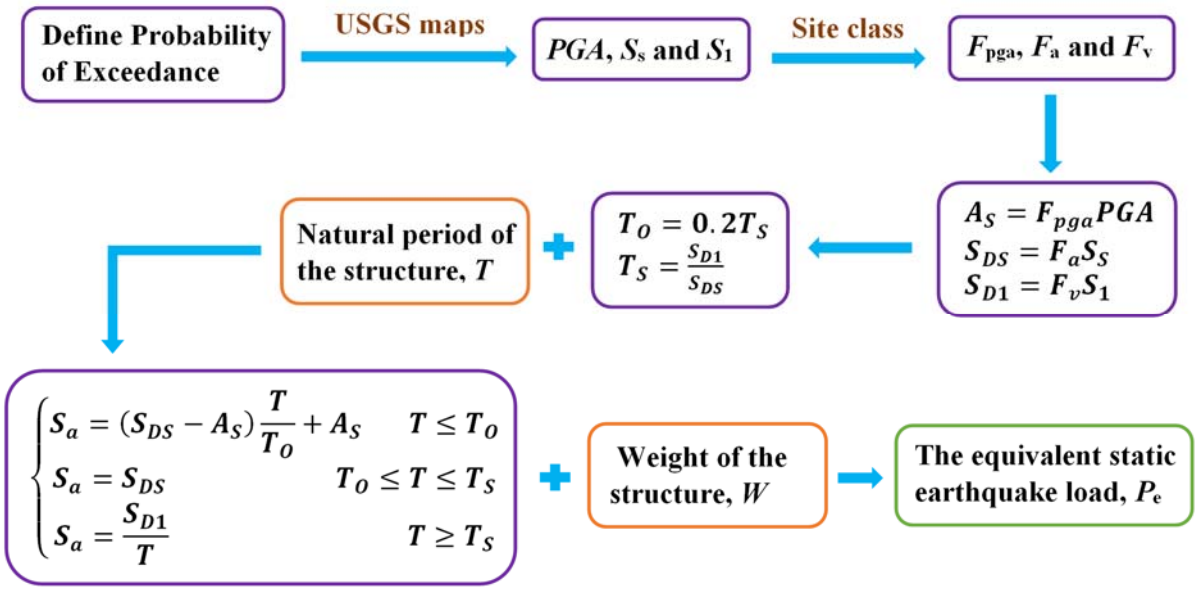

Figure 4-7. Procedures for the Equivalent Static Analysis (ESA).

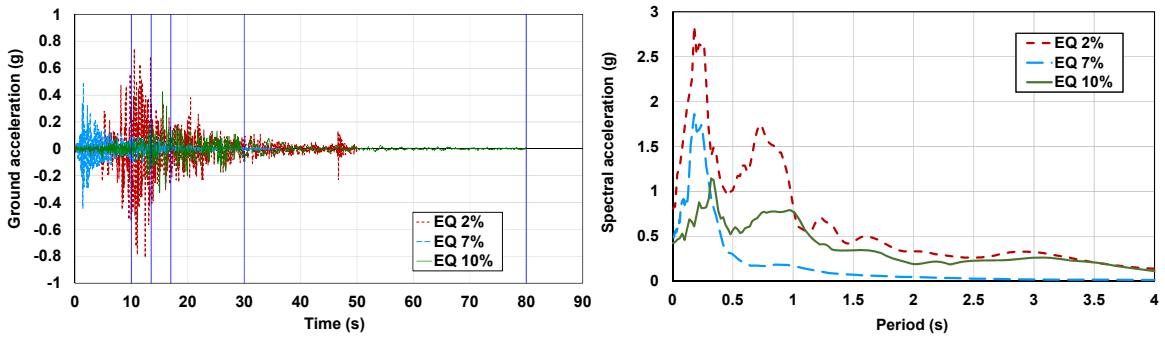

(a) **(b)**

Figure 4-8. (a) Time history and (b) Spectral acceleration of ground motions with 2% and 10% probability of exceedance in 50 years and 7% probability of exceedance in 75 years.

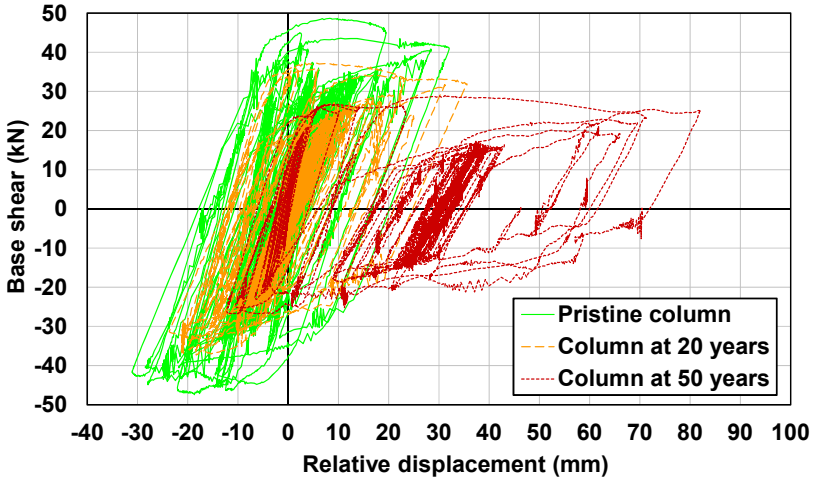

(a)

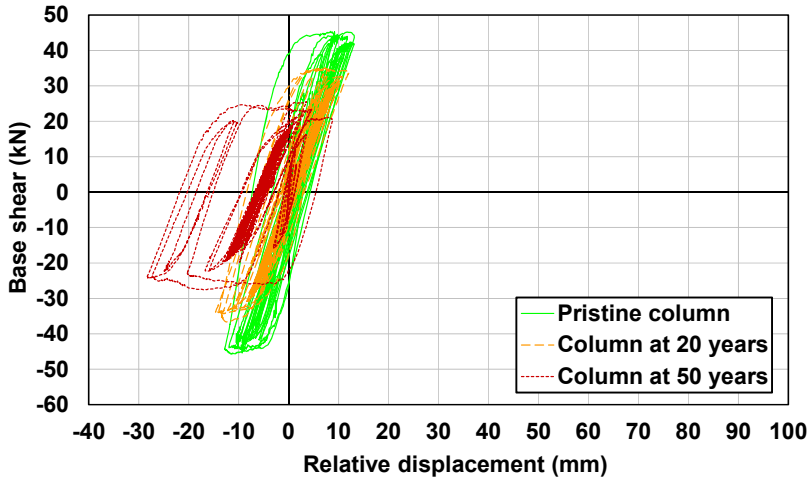

(b)

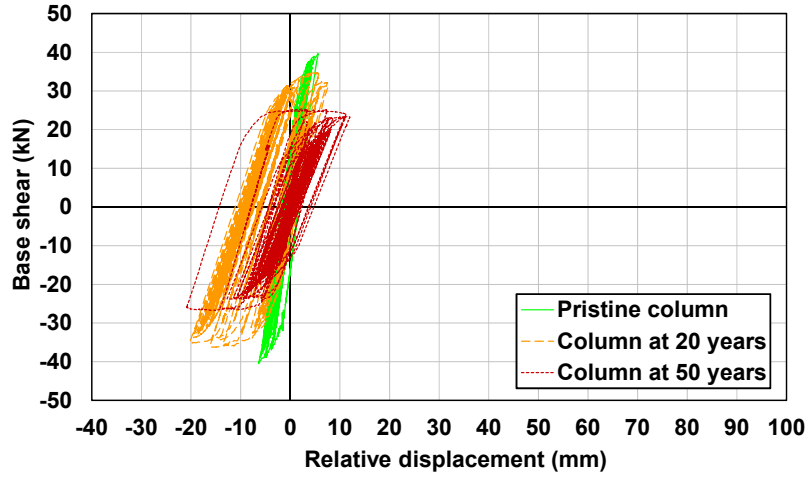

(c)

Figure 4-9. Base shear vs. displacement hysteresis loops of columns under: ground motions with (a) 2% PE in 50 years; (b) 7% PE in 75 years and (c) 10% PE in 50 years.

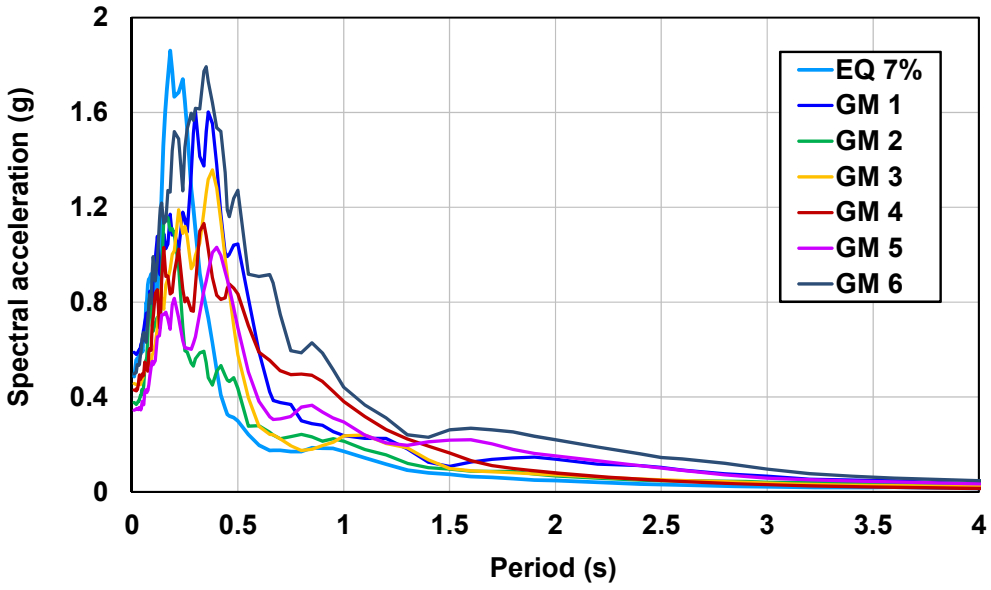

Figure 4-10. Spectral acceleration of a suite of ground motions with 7% probability of exceedance in 75 years.

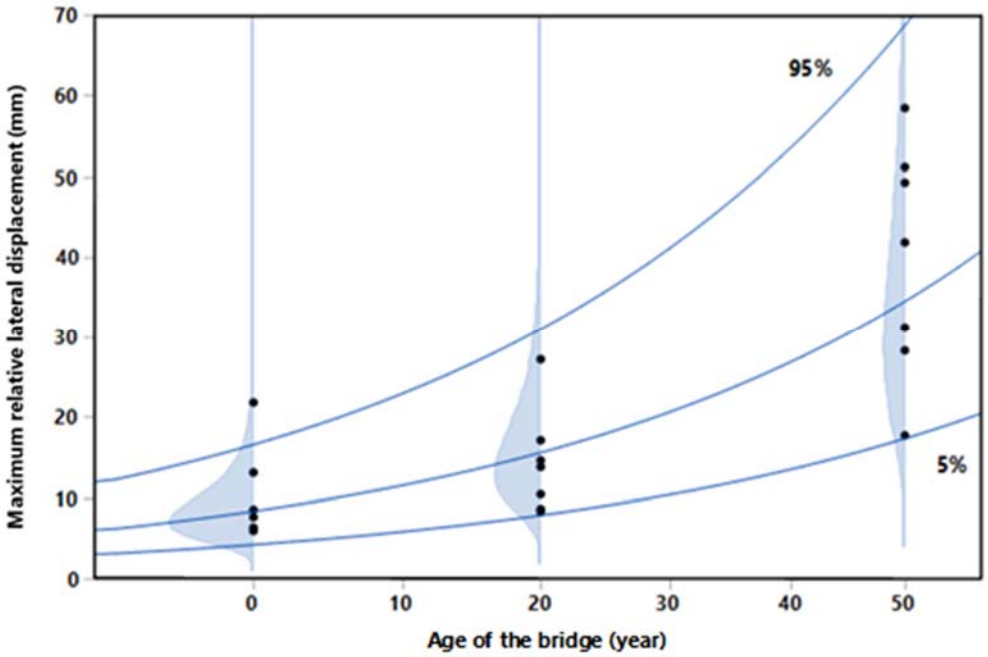

Figure 4-11. Maximum relative lateral displacements of the column under the ground motions with 7% PE in 75 years.

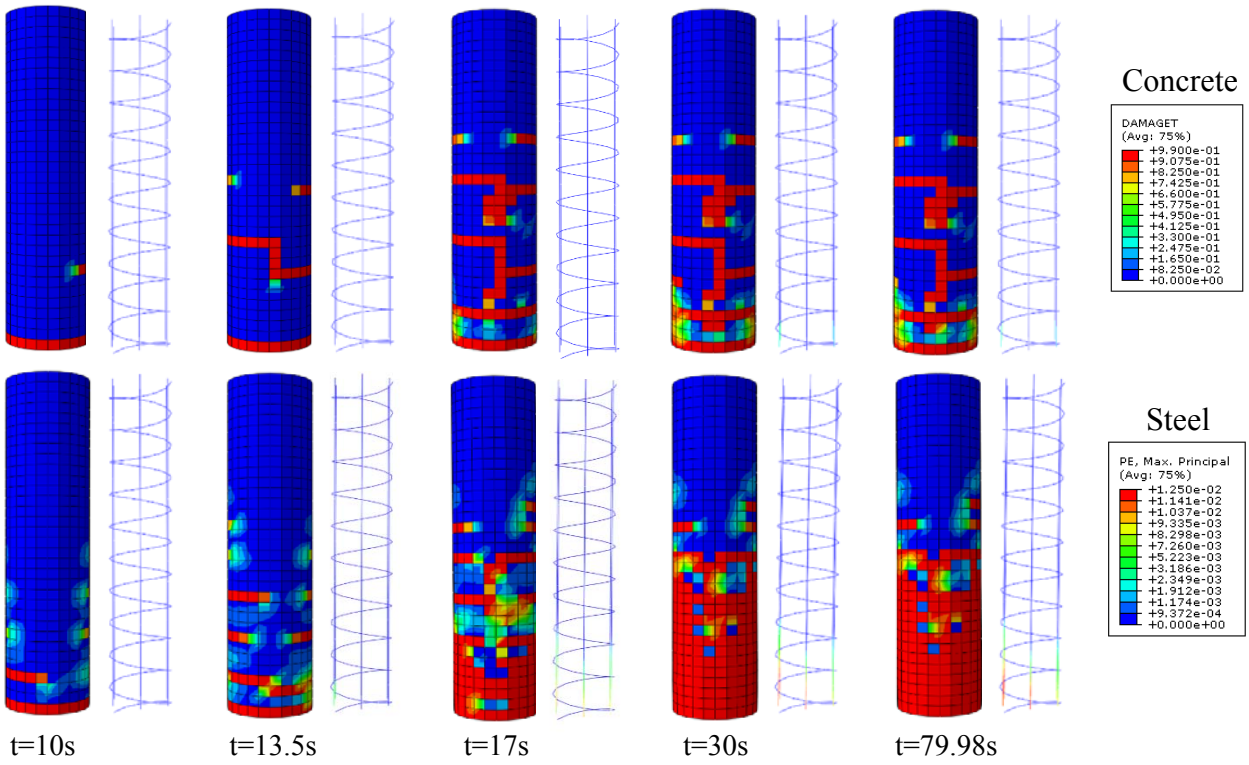

Figure 4-12. Crack propagation patterns and steel plastic strains of the column at (top) 0 year and (bottom) 20 years under EQ 10%.

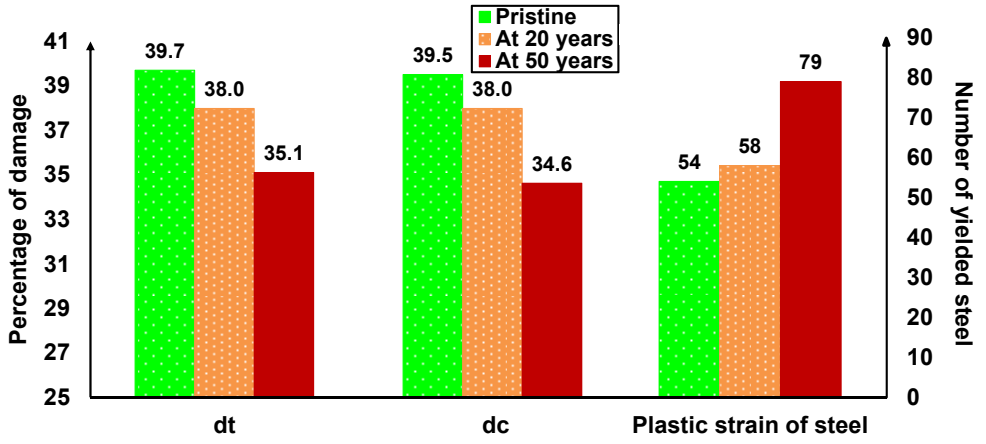

(a)

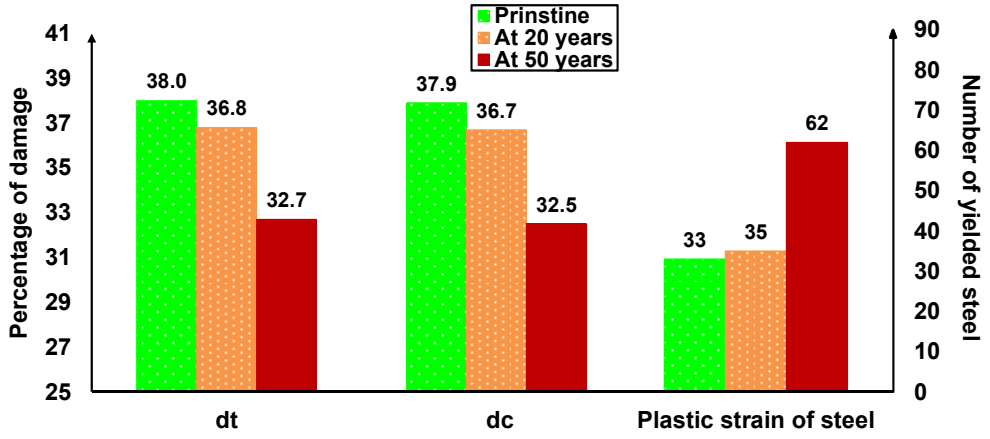

(b)

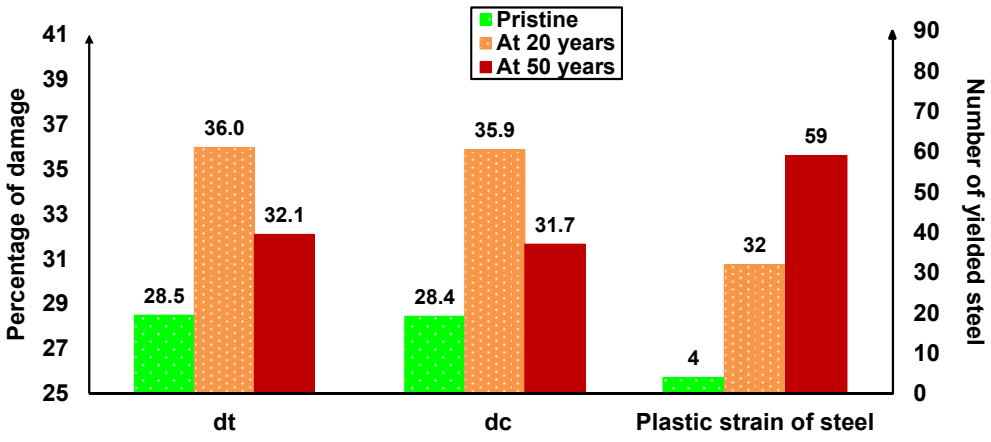

(c)

Figure 4-13. Extent of damage of the columns under: (a) EQ 2%; (b) EQ 7%; (c) EQ 10%.

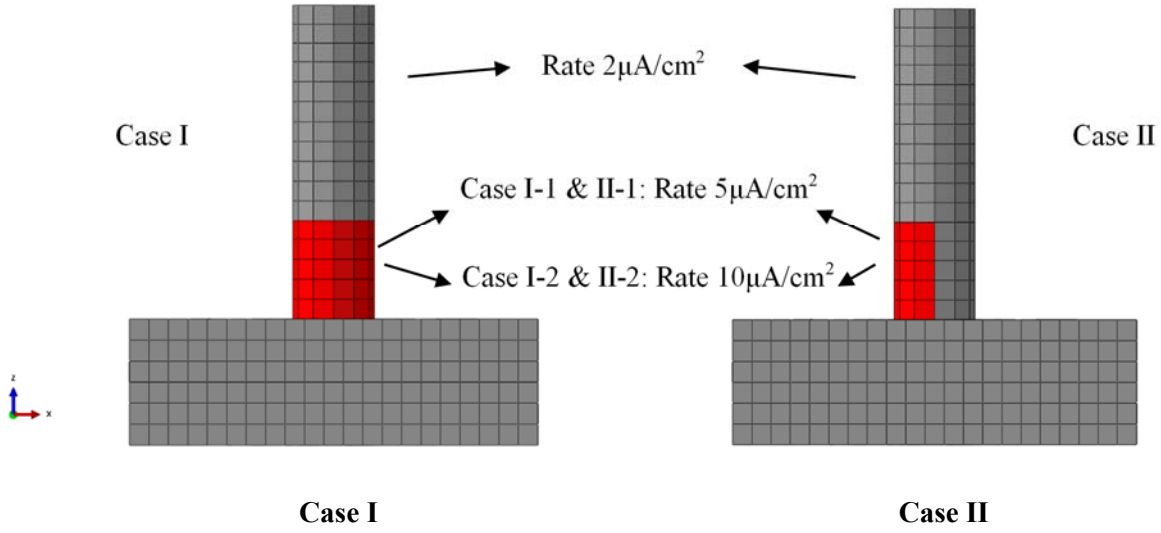

Figure 4-14. Schematic representation of two case study columns with non-uniform corrosion.

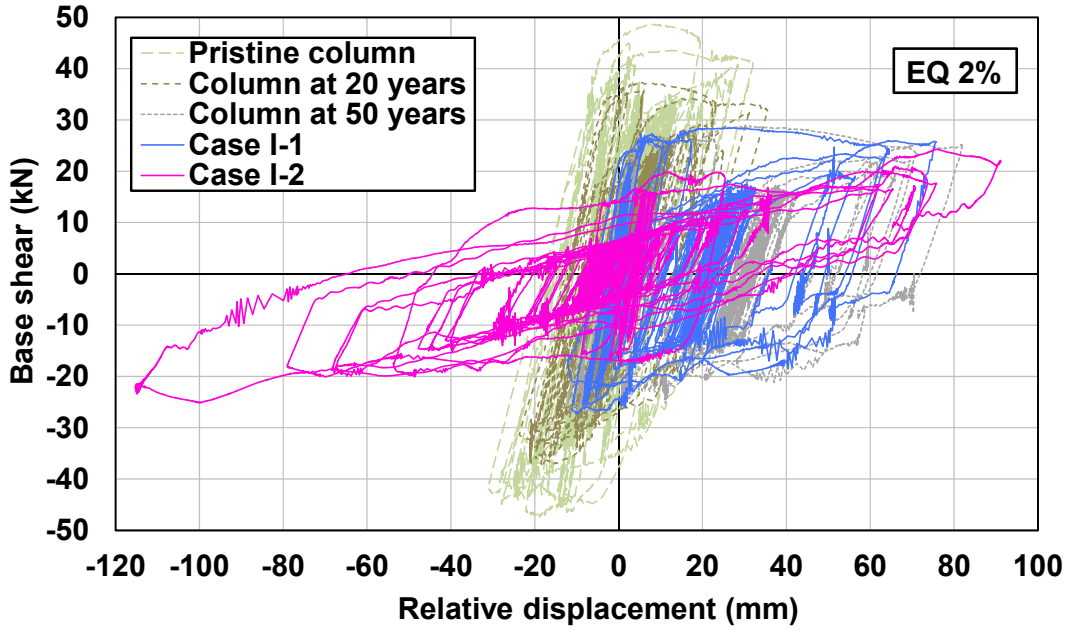

(a) Case I

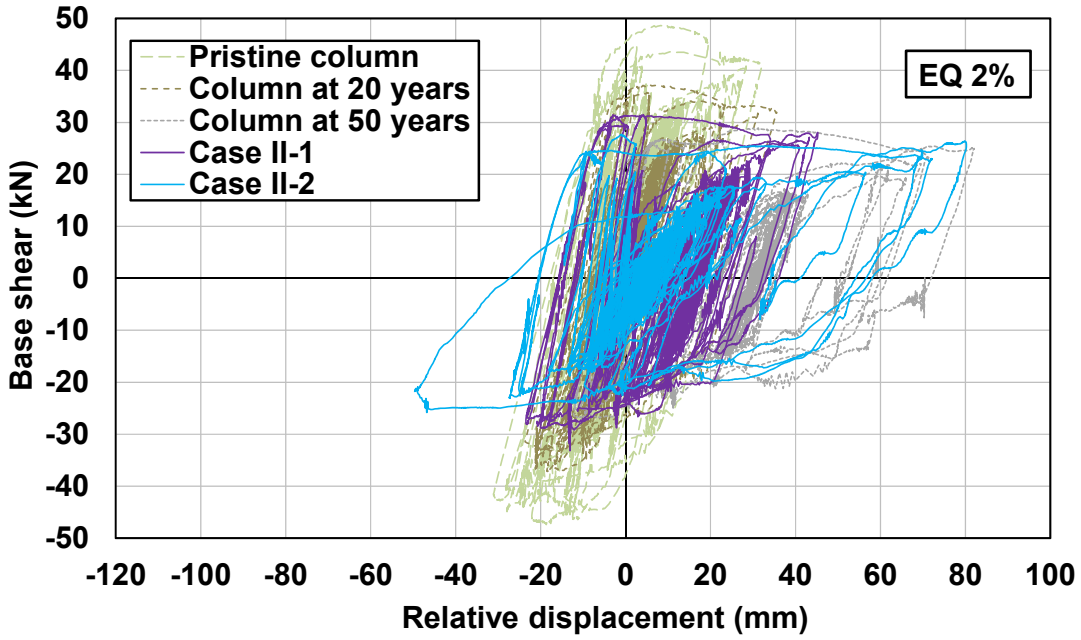

(b) Case II

Figure 4-15. Base shear versus displacement hysteresis loops of columns under EQ 2% for the two case study columns with non-uniform corrosion.

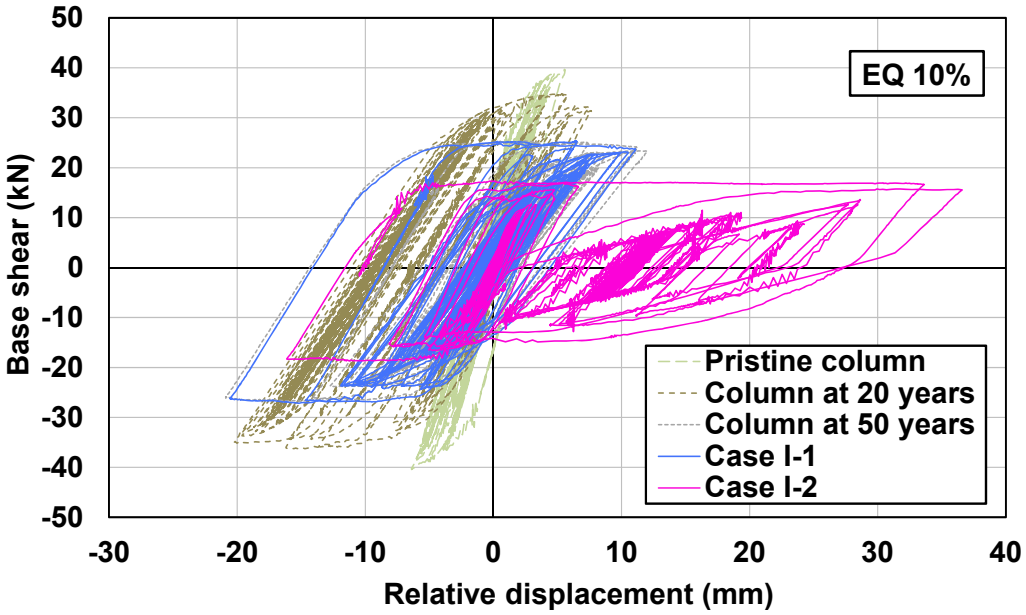

(a) Case I

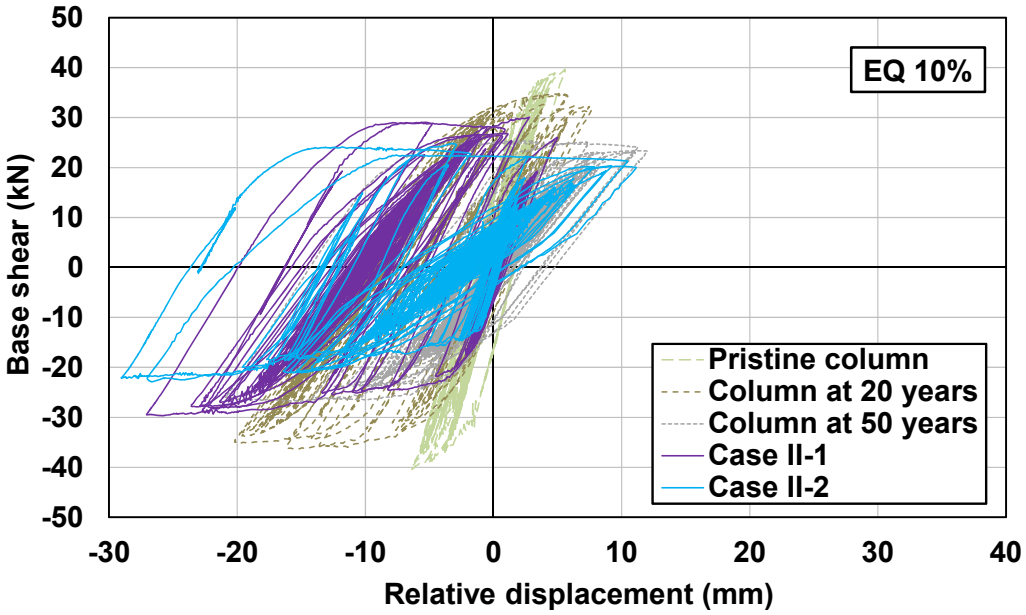

(b) Case II

Figure 4-16. Base shear versus displacement hysteresis loops of columns under EQ 10% for the two case study columns with non-uniform corrosion.

CHAPTER 5. STRUCTURAL PERFORMANCE OF DETERIORATING REINFORCED CONCRETE COLUMNS UNDER MULTIPLE EARTHQUAKE EVENTS

A paper submitted to the journal of *Bridge Engineering (ASCE)*

Zhen Cui, Alice Alipour and Behrouz Shafei

5.1 Abstract

This paper studies the life cycle performance of reinforced concrete (RC) columns that are subjected to multiple seismic events at different time periods while they are continuously subjected to chloride-induced corrosion. The adverse effects of corrosion have been implemented into the proposed three dimensional nonlinear finite element (FE) model and the extent of structural degradation is updated based on the age of the column. A set of case scenarios have been developed to investigate the extent of damage when the column experiences two earthquake events with different levels at various time periods during its lifetime. The impact of the first earthquake-induced damage on the corrosion process has been taken into account. The increased corrosion rate after the first earthquake is used to predict the degradation of the damaged RC column under future corrosion and more realistic predictions for the performance of the column after the future earthquake are obtained. The developed framework is able to quantify the effect of corrosion on the seismic capacity of RC structures and the extent of damage after each earthquake when the structures experience multiple seismic events.

Keywords: multiple seismic events, chloride-induced corrosion, reinforced concrete, finite element analysis, multi-hazard

5.2 Introduction

Reinforced concrete (RC) structures are usually subjected to various environmental stressors and natural hazards during their life cycle. Structures are aging and deteriorating under environmental stressors, such as the corrosion induced by airborne sea salt or deicing salt, which may significantly reduce the capacity and durability of RC structures. In addition to the deterioration, structures may be exposed to one or more natural hazards depending on their locations. For instance, in high seismic risk areas, structures may undergo different levels of earthquakes during their life cycle. This will create a condition where some of the remaining damage from the previous minor earthquakes in addition to weakening the structure, can create a pathway for the chloride ions to intrude even faster and result in more deterioration by the time the next earthquake occurs.

Extensive research has been conducted for the corrosion induced by chloride ions (Cheung et al. 2009, Shafei et al. 2012, O'Connor and Kenshel 2013, Shafei and Alipour 2015, Hu et al. 2016), as well as the corrosion effects on structural performance (Rodriguez et al. 1997, Coronelli and Gambarova 2004, Cui and Alipour 2014). There have been a number of experimental studies focused on seismic behaviors of corroded members (Ou et al. 2012, Meda et al. 2014, Guo et al. 2015). Numerical studies on seismic response of corroded structures includes Alipour (2010), Alipour et al. (2011), Ou et al. (2013), Alipour and Shafei (2014), Yalciner et al. (2015). Although the research has captured the residual capacity of the corroded structures under the earthquakes, all of them were focused on the behaviors of the structures experiencing one earthquake at a time without considering the impact of the earthquake-induced damage on the progress of the corrosion in future or its performance under other future earthquakes. This is a likely scenario in seismic prone regions that requires attention. This

paper aims to study the seismic performance of corroded RC columns subjected to multiple seismic events that occur at different stages. A set of case scenarios including two earthquakes with different hazard levels, variant corrosion rates due to previous earthquake-induced damage, as well as multiple column ages are developed and applied to the generated 3D nonlinear FE model. This FE model is validated by the pervious experimental tests and is capable of including the corrosion effects and updating the corresponding structural degradation as a function of the column age. Moreover, the region and type of damage are identified, and the extent of damage are quantified. The residual damage from the first earthquake is considered as a new state condition for the structure that carries over throughout the life cycle of the structure until the second earthquake occurs. The details of local damages as well as frequencies of the column before and after each earthquake are obtained.

This study provides a comprehensive approach to evaluate the lifetime performance of corroded RC members under multiple seismic events. The details of damage before and after each seismic event can be captured. The outcome of this research will help engineers and designers predict the performance of the structures in multiple earthquake events, as well as help inspectors identify damage regions, make necessary test plans, and optimize rehabilitation strategies for RC structures.

The remainder of the paper is structured as follows: i) chloride-induced corrosion initiation and propagation, ii) effects of corrosion, iii) effect of earthquake-induced damage on corrosion rate, iv) FE models and case study scenarios, v) life cycle performance of corroded RC columns subjected to two earthquake events, and vi) conclusions.

5.3 Chloride-induced corrosion initiation and propagation

The corrosion of reinforcement is one of the main causes of deterioration of RC structures (Cairns et al. 2005, Val and Chernin 2009, Apostolopoulos et al. 2013). In coastal areas with airborne sea salt particles or harsh winter regions with high exposure to deicing salts, chloride-induced corrosion is the dominant mechanism. Chloride ions gradually diffuse through concrete towards reinforcing steel. When chloride concentration at the steel surface reaches its critical level, corrosion initiates. Then the steel is consumed and rust is produced at the interface of steel and concrete. Since the volume of the produced rust is higher than the consumed steel in the process, internal pressure is induced on the surrounding concrete, causing formation of concrete cracks and finally leading to spalling of concrete cover (Figure 5-1).

The extent of structural degradation due to chloride-induced corrosion during its lifecycle can be calculated using Faraday's Law, which relates steel mass loss over time to current density.

$$M_{st}(\mathrm{t}) = \frac{mIt}{zF} \quad (5\text{-}1)$$

where m is the atomic mass of iron (56g for Fe), F is Faraday's constant, which is 96500 A·s, z is the ionic charge (for instance, 2 for $Fe \rightarrow Fe^{2+}+2e^{-}$), t is the time after corrosion initiation (s), and I is the current ($I = a_s i_{corr}$ (A), a_s is the surface area of the steel bar, i_{corr} is the current density (A/cm^2)). For a unit length of a rebar, $a_s = \pi d$. Thus, the mass loss of steel per unit length of a rebar for a time step after corrosion initiation, Δt (s), is calculated as:

$$M_{st}(\mathrm{t}) = \frac{m\pi d^r(t)}{zF} i_{corr} \Delta t = 2.894 \times 10^{-4} i_{corr} \pi d^r(t) \Delta t \quad (5\text{-}2)$$

where d^r is the residual rebar diameter (cm). The density of steel is taken as 7.8g/cm^3. Hence, the volume change of consumed steel per unit length can be calculated as follows:

$$A_{st}(\mathrm{t}) = \frac{M_{st}(t)}{\rho_{st}} = 3.709 \times 10^{-5} i_{corr} \pi d^r(t) \Delta t \quad (5\text{-}3)$$

The residual diameter of rebar after each time step can be determined as

$$d^r(t) = \sqrt{d^2 - \frac{4A_{st}(t)}{\pi}} \quad (5\text{-}4)$$

Therefore, the residual rebar diameter at a certain time step can be calculated using the last two above equations once the corrosion rate is determined. The mass loss of steel due to corrosion can be updated over time.

5.4 Effects of corrosion

The effects of corrosion on steel reinforcement includes reduction of steel cross sectional area, reduction of steel yield and ultimate strengths, as well as reduction of steel ultimate strain. The cross sectional area reduction of the steel bar can be calculated as follows (Berto et al. 2008):

$$A_{st}^r = \frac{\pi(d - \lambda_b x_b)^2}{4} \quad (5\text{-}5)$$

where A^r_{st} is the residual cross sectional area of a steel bar, d is the original diameter of a steel bar, x_b is the radius reduction of the bar, and λ_b takes into account the possibility of a one-side or two-side corrosion attack penetration (For uniform corrosion, λ_b=1).

The residual yield and ultimate strengths of corroded reinforcement can be estimated using the following empirical formulas that are based on experimental data (Cairns et al. 2005):

$$f_y^r = (1 - 0.015\eta_{100}) f_y^0 \quad (5\text{-}6)$$

$$f_u^r = (1 - 0.015\eta_{100}) f_u^0 \quad (5\text{-}7)$$

where f_y^r and f_u^r are the residual yield and ultimate strengths of corroded reinforcement, respectively, f_y^0 and f_u^0 are the yield and ultimate strengths of original reinforcement,

respectively, and η_{100} is the percentage of steel mass loss, calculated from the consumed steel mass per unit length divided by the initial steel mass per unit length ($\eta_{100}=M_{st}/M_0\times100$).

The ultimate strain of corroded reinforcement is calculated empirically as follows:

$$\varepsilon_{su}^{r} = (1 - 0.039\eta_{100})\varepsilon_{su}^{0} \quad (5\text{-}8)$$

where ε^{r}_{su} is the ultimate strain of corroded reinforcement and ε^{0}_{su} is the ultimate strain of original reinforcement. The above formulas are consistent with the findings from more recent experimental tests (Kashani et al. 2013). Figure 5-2(a) illustrates the constitutive models of pristine and corroded steel.

The corrosion effect on concrete can be considered by the formation of cracks and degradation of compressive strength in concrete cover, as well as using a brittle post-peak behavior in the compressive constitutive model of concrete (Coronelli and Gambarova 2004). The reduced compressive strength of concrete can be calculated using the following equations:

$$f_c^r = \frac{f_c'}{1+\frac{R\varepsilon_a}{\varepsilon_c}} \quad \text{and} \quad \varepsilon_a = \frac{b_1}{b_0} - 1, \quad b_1 = b_0 + nw \quad (5\text{-}9)$$

where ε_c is concrete strain at the compressive strength, f'_c, ε_a is the average tensile strain in cracked concrete perpendicular to the direction of the applied compression, R is a coefficient related to the roughness and diameter of reinforcement ($R = 0.1$), b_0 is the original width of the cross section, b_1 is the increased width due to corrosion cracks, n is the total number of reinforcement in the top layer, and w is the total crack width which can be calculated as follows (Molina et al. 1993):

$$w = \sum_i w_i = 2\pi x_b(\lambda - 1) \quad (5\text{-}10)$$

where w_i is each single crack width and λ is the volumetric ratio, which varies depending on the composition of corrosion products. Figure 5-2(b) shows the constitute models of pristine and degraded concrete.

5.5 Crack width and effect of earthquake-induced damage on corrosion rate

Corrosion of reinforcement leads to steel section loss and rust production, which induces cracking of the concrete cover. The crack widening and propagation in the concrete cover will facilitate the intrusion of chloride ions into concrete. Several research projects have been conducted on the relations between the corrosion-induced crack width and the corrosion degree which is often expressed in terms of steel mass loss per unit length or corrosion penetration (rebar radius reduction) (Vidal et al. 2004, Val et al. 2009, Andrade et al. 2010, Zhang et al. 2010, Xia and Jin 2014). It has been concluded that the average crack widths due to corrosion increase with the steel cross sectional loss. Andrade et al. (2010) have developed equations for calculating corrosion-induced crack widths of the concrete cover in natural environments based on experimental test results:

$$w = k(\frac{x_b}{r}) \tag{5-11}$$

where w is the crack width, r is the original radius of the reinforcement, x_b is the corrosion penetration, i.e., radius reduction, and k is the factor, the value of which is derived from experimental results, taken as 35.5. The time-dependent corrosion penetration at time t (years) after corrosion initiation can be calculated as (DuraCrete 2000):

$$x_b = 0.0115 i_{corr} t \tag{5-12}$$

where i_{corr} is the corrosion rate ($\mu A/cm^2$). Substituting Equation 5-12 into Equation 5-11, the time-dependent crack width can be related to the corrosion rate and calculated as:

$$w = \frac{0.0115 k i_{corr}}{r} t \tag{5-13}$$

After earthquake occurs, the reinforced concrete columns may experience certain damage due to seismic loadings, such as the cracking of concrete cover. The earthquake-

induced cracks will lead to the increase of corrosion rate. Otieno et al. (2016b) proposed a predictive model for chloride-induced corrosion rate that takes into account the effect of crack width based on a series of experimental test results (Otieno et al. 2016a). The derived predictive models of corrosion rate are:

$$i_{corr} = 5.18e^{0.01D_c\times10^{10}}\left(\frac{c}{w}\right)^{-0.96(D_c\times10^{10})^{-0.35}} \quad \text{for lab specimens} \tag{5-14}$$

$$i_{corr} = 0.64e^{0.06D_c\times10^{10}}\left(\frac{c}{w}\right)^{-0.21e^{0.02D_c\times10^{10}}} \quad \text{for field specimens} \tag{5-15}$$

where D_c is the chloride diffusion coefficient and c is the concrete cover thickness.

5.6 FE modeling and case study scenarios

Finite element analysis is conducted to investigate the structural performance of RC columns. Laboratory data from the tests that Ma et al. (2012) conducted have been used to validate the results generated by the FE models. In these tests, RC circular columns with different extents of corrosion were tested under combined cyclic lateral loadings and constant axial loading. Each column is 260mm in diameter and 1000mm in height with a 1300mm×360mm×400mm stub (Figure 5-3a). The clear concrete cover to the spiral stirrups is 30mm. The longitudinal reinforcement in both column and stub is 16mm in diameter. The spirals are 8mm in diameter with a spacing of 100mm and the stirrups in the stub are 8mm in diameter. The 28-day compressive strength of concrete is 32.4MPa. The yield and ultimate strengths of longitudinal reinforcement are 373.2 and 572.3MPa, respectively. The yield and ultimate strengths of transverse reinforcement in the column and stub are 327 and 510.7MPa, respectively.

The generated FE model is shown in Figure 5-3(b). 3D eight node solid elements are used to model the column concrete and 3D two node truss elements are used to model the steel reinforcement. Damaged plasticity model is selected to model the concrete properties. This model assumes that the main failure mechanisms are tensile cracking and compressive

crushing. It takes into account the degradation of the elastic stiffness induced by plastic straining both in tension and compression (ABAQUS 2012). The reduction of the elastic modulus is expressed in terms of the degradation variable, d_1 (d_c or d_t).

$$E = (1 - d_1)E_0 \tag{5-16}$$

where E_0 is the initial modulus of concrete and d_1 is the damage variable. d_c and d_t are the damage variables of concrete in compression and tension, respectively. Bilinear kinematic hardening model is selected for the steel reinforcement. Great agreement is observed between experimental and numerical results (Figure 5-3c). More details on comparing the results could be found in Cui and Alipour (2016).

With the results of the FE model validated, similar approach is used to generate the FE models of the full scale RC columns in this paper. The columns here are a part of the RC bridges located in the Los Angeles area and satisfy the current seismic design requirements. The bridges have two equal spans of 30m. The total concrete cross-section of deck is approximately 12m^2. The bridges have only one interior bent with two identical circular columns. Each column is 1.6m in diameter with a concrete cover of 50mm and 10m in height with a 3m×3m×2m foundation. The compressive strength of concrete is 32.4MPa. The diameter of longitudinal reinforcement in the column is 62mm. The stirrups of the column are 19mm in diameter with a spacing of 100mm. Square hoops in both directions of the foundation are 57mm in diameter with a spacing of 150mm. The yield and ultimate strengths of steel reinforcement are 475MPa and 655MPa, respectively. The mass of bridge superstructure above the column is simplified as lumped on top of the column. The top of column has only one degree of freedom in the horizontal direction to represent the interaction between the column and the superstructure of the bridge (Figure 5-4).

The corrosion rate of 5.0μA/cm^2, which is within the normal range of corrosion rate (Jamali et al. 2013), is considered in this study. The properties of the columns, such as steel cross sectional area, steel and concrete material properties, and bond-slip relationship degrade after corrosion initiation. The extent of the corrosion-induced degradation is calculated according to the equations provided in the effects of corrosion section and is calculated based on the steel mass loss over time, which is updated as a function of time according to the chloride-induced corrosion initiation and propagation section. The structural degradation due to corrosion is calculated at 10 year time intervals. Table 5-1 shows the steel mass loss in 10 year time intervals within the design life of the RC column. The level of deterioration increases with time. The degraded properties of the column are updated accordingly. Pushover analysis is conducted for the columns at 0, 10, 20, 30, 40, 50, 60 and 70 years (Figure 5-5). As corrosion level increases with the age of the column, both capacity and stiffness of the column will reduce. The maximum base shear capacities of the columns from 10 to 70 years reduces by 7.9% to 31.5% respectively.

In order to study the seismic performance of corroded columns under multiple earthquake events, a set of case study scenarios are defined. In each case scenario, the column experiences two earthquakes at two different stages of its life cycle. At the first stage, the column experiences the first earthquake. The region, type and extent of damage in the column are recorded after this first stage. Then the residual damage including plastic strain and deformation, as well as concrete cracking and crushing from the first analysis is used to estimate the new corrosion risk to the column. The extra cracks introduced by the first earthquake will make the column more vulnerable to the intrusion of chloride ions, increasing the rate of corrosion. The cumulative damage from the first earthquake and the faster corrosion

process are used as an initial condition for the column undergoing the second earthquake event. The structural degradation of the column under the increased corrosion rate will be updated as a function of the column age when it experiences the second earthquake. The damage after the second earthquake will then be recorded. Figure 6 details the procedure for this analysis.

There are three different approaches for seismic design of bridges: Equivalent Static Analysis (ESA), Elastic Dynamic Analysis (EDA) and Nonlinear Time History Method (AASHTO-LRFD 2012). Equivalent Static Analysis and linear Elastic Dynamic Analysis are appropriate for estimating the displacement demands for normal bridges and their individual components. The ESA can be used for short to medium span bridges with regular configuration. For long bridges or where ESA does not provide an adequate level of sophistication to estimate the dynamic behavior, EDA should be used. Nonlinear Time History Method is the most comprehensive but the most complex analysis method among the three methods. It is best used for bridges with SDC D (the Seismic Design Category D) or seismically isolated bridges with long periods or large damping ratios. Since the bridge used in this study is a typical bridge with short spans and regular configuration that represents many bridges constructed in the United States, Equivalent Static Analysis will be used to investigate the seismic performance of the intact and corroded bridge columns. This method also reduces computational cost and is easier for engineers to apply in practice. The ESA utilizes a uniform lateral load to approximate the effect of seismic loads. In this study, a lateral load (equivalent static load) is applied to the top of the column to simulate the effect of seismic loads. Figure 5-5 shows the procedure to calculate the equivalent static load for different earthquake levels.

Two earthquake hazard levels, 2% and 10% probability of exceedance (PE) in 50 years, are considered in this study. The annual probabilities of exceedance of the earthquakes with

PE of 2% and 10% in 50 years are 4.0×10^{-4} and 2.1×10^{-3}, respectively. Eight column ages of 0, 10, 20, 30, 40, 50, 60 and 70 years are considered in this study and they are symbolized as Y0, Y10, Y20, Y30, Y40, Y50, Y60 and Y70, respectively. As shown in Figure 5-7, the column in the corrosive environment is continuously subjected to chloride-induced corrosion with a corrosion rate of 5.0μA/cm^2 ($i_{corr,1}$). At the time when the first earthquake (EQ 1) occurs, the crack width of the column due to corrosion (w_1) can be calculated using Equation 5-13. The first earthquake causes certain damage including cracks in the concrete cover, the width of which can be obtained by the FE results using the maximum principle strain of the column. Then the total crack width (w_2) after the first earthquake can be estimated by adding the earthquake-induced crack width to the corrosion-induced crack width at the time when the first earthquake occurs. Based on Otieno et al. (2016b), the increased crack width (w_2) will lead to faster corrosion progress. The increased corrosion rate ($i_{corr,2}$) due to the first earthquake-induced damage can be calculated using Equation 5-15. Then the damaged column that carries the residual damage from the first earthquake will continue deteriorating under the increased corrosion rate ($i_{corr,2}$) until the second earthquake (EQ 2) occurs. The time-dependent degradation of the damaged column is calculated based on the increased corrosion rate ($i_{corr,2}$).

Three specific case scenarios are studied here to illustrate the application of the developed FE framework and to investigate the lifetime performance of the RC column under multiple seismic events while the columns are continuously subjected to chloride-induced corrosion. The three cases are 0Y30Y (E10Y0E2Y30), 20Y50Y (E10Y20E2Y50) and 40Y70Y (E10Y40E2Y70). For all the three cases, the column will first experience a less severe earthquake E10 that results in minor damage. Minor damage here follows the definition by HAZUS-MH (2012) where it is defined as: minor cracking or spalling, damage requires no

more than cosmetic repair. Then the column will experience a more severe earthquake E2. The case 20Y50Y (E10Y20E2Y50) represents that the column is under corrosion for 20 years with a corrosion rate of 5.0μA/cm^2 ($i_{corr,1}$). Then the first earthquake E10 occurs. After that, the column deteriorates under an increased corrosion rate of 7.3μA/cm^2 until the second earthquake occurs at 50 years. The corrosion-induced crack width (w_1) of the column at 20 years before the first earthquake is 0.7mm and the total crack width (w_2) including earthquake impact after the first earthquake is 1.6mm. The increased corrosion rate after the first earthquake is 7.3μA/cm^2 ($i_{corr,2}$). For the case 40Y70Y (E10Y40E2Y70), the column is under corrosion for 40 years with a corrosion rate of 5.0μA/cm^2 ($i_{corr,1}$) until the first earthquake E10 occurs. The corrosion-induced crack width (w_1) of the column at 40 years before the first earthquake is 1.4mm and the total crack width (w_2) including earthquake impact after the first earthquake is 2.5mm. Then the column deteriorates under an increased corrosion rate of 8.0μA/cm^2 ($i_{corr,2}$) until the second earthquake occurs at 70 years.

5.7 Performance of RC columns under the threat scenarios

The performance of the columns under the three different threat scenarios are presented in this section. Figure 5-8 shows the extent of damage for all of the three cases. In order to investigate the impact of the damage from the first earthquake on the corrosion progress afterwards, as well as the impact of the increased corrosion rate on the damage after the second earthquake, the results from another set of the three cases with constant corrosion rate before and after the first earthquake also presents in Figure 5-8. The types of damage in the column includes concrete and steel damage. The concrete damage contains the damage in tension (d_t) and in compression (d_c) (see Equation 5-16). The steel damage is expressed in terms of number of the elements that experience plastic strain. The percentage of damage in Figure 5-8 is the number

of the damaged concrete elements to the total number of the concrete elements. The number of yielded steel is the number of steel elements with a non-zero plastic strain. The pink regions of the bars show the damage extent after the first earthquake. The blue regions of the bars show the damage extent solely from the second earthquake. The labels above the bars show the total damage extent after the two earthquakes.

It can be seen from Figure 5-8 that under both constant corrosion rate and variant corrosion rate (considering the increase of corrosion rate after the first earthquake due to earthquake-induced damage), the total damage extent is increasing from the case 0Y30Y to 20Y50Y and from 20Y50Y to 40Y70Y, although the time interval between the first and second earthquakes for all of the cases is 30 years. This indicates the column experiences more damage if both the two earthquakes occurs later when the column suffers from higher level of corrosion. After the first earthquake, the percentages of concrete damage for all the three cases are relatively low, ranging from 14.5% to 35.1% of tensile damage and 10.3% to 32.3% of compressive damage, and no steel yielding occurs in the column. The column only experiences minor damage after the first earthquake for all the cases and no repair is required. However, after the second more severe earthquake, both concrete and steel damage is significantly increased. With the variant corrosion rate, the total percentages of concrete tensile damage after two earthquakes increase by 2.2% and 70.6%, compared to the ones with the constant corrosion rate for the case 20Y50Y and 40Y70Y, respectively. The total percentages of steel damage after two earthquakes under the variant corrosion rate are 2.7% and 17.6% for the cases 20Y50Y and 40Y70Y, respectively, whereas under the constant corrosion rate, the total percentages of steel damage are 1.1% and 3.4% for the cases 20Y50Y and 40Y70Y, respectively. It is noticed that for the case 40Y70Y, both concrete and steel damage

dramatically increased after the second earthquake under the variant corrosion rate case. The column experiences complete failure. But under the constant corrosion rate case without considering the faster corrosion process due to the cracks induced by the first earthquake, the column experiences extensive damage rather than complete failure. Therefore, it can be known that taking into account the effect of the first earthquake-induced damage on the corrosion process, the damage extent of the column will increase, particularly for the column under a higher corrosion level. Ignoring the impact of the damage caused by the minor previous earthquakes on the corrosion progress may significantly underestimate the damage extent under the future earthquake, thus gives unrealistic predictions for the performance of the column.

The corrosion level expressed in terms of the steel mass loss percentage under both constant and variant corrosion rates are shown in Figure 5-9. It can be seen that consdering the increase of corrosion rate due to the previous earthquake-induced damage will increase the corrosion level by 21.7% for the case 20Y50Y, and 14.9% for the case 40Y70Y. Figure 5-9 shows that the increase in corrosion rate will slow down as the mass loss percentage increases. This could be attributed to the fact that the corrosion process slows down as rust layer thickens which will increase the difussion distance of ionic iron.

Figure 5-10 shows the natural frequency of the column before and after each earthquake for both constant and variant corrosion rates. It can be seen that the frequencies of the intact and corroded columns before experiencing the first earthquake are relatively similar. However, the frequencies of the columns drop significantly after the first earthquake and are further reduced after the second earthquake. Under the variant corrosion rate, the frequencies of the columns after the second earthquake drop more than those under the constant corrosion rate

(4.7% more for the case Y20Y50 and 10.7% more for the case Y40Y70), indicating a higher extent of damage of the column due to considering the impact of the first earthquake. This also highlights the importance of including the impact of the previous earthquake-induced damage on the corrosion process for providing realistic predictions of the column performance under future earthquakes.

5.8 Conclusions

This paper studies the lifecycle performance of deteriorating RC columns subjected to multiple seismic events. The effects of chloride-induced corrosion including steel area reduction, steel and concrete property degradation has been analyzed and incorporated into a three dimensional nonlinear finite element framework. The extent of structural degradation has been updated as a function of the age of the structural components and is based on a more realistic estimation of corrosion process. The FE modeling technique has been validated through previous experimental tests. Real scale FE models of the columns from 0 to 70 years have been generated. The capacities of the columns have been evaluated through nonlinear pushover analysis and found to be greatly influenced by the age of the column, i.e. the level of corrosion. The strength and stiffness drop significantly as corrosion level increases. A set of case study scenarios containing two earthquakes with different PEs in 50 years occurring at different ages of the column have been developed to investigate the lifetime performance of the columns under both corrosion and multiple earthquakes. The effect of the first earthquake-induced damage on the corrosion progress has been taken into consideration. The increased corrosion rate after the first earthquake is utilized to predict the further degradation of the damaged column under future corrosion mechanisms and more realistic predictions for the performance of the columns after the future earthquake are obtained. The extent of both concrete and steel

damage of the column from each earthquake and the extent of the total damage after the two earthquakes have been quantified. The frequencies of the column before the first earthquake and the reduced frequencies after each earthquake have also been obtained. It is found in this study that taking into account the impact of the previous earthquake-induced damage on the corrosion process, the column damage extent after future earthuqakes will increase, particularly for the columns under high corrosion levels. Ignoring the influence of the damage caused from the previous earthquake on the corrosion progress may significantly underestimate the damage extent under future earthquakes, giving unrealistic predictions for the lifetime performance of the columns. The results of this study emphasize the necessity of considering the combined effects of earthquake and corrosion to predict the structural performance under multiple seismic events. The developed framework is capable of predicting the damage extent after each earthquake when multiple earthquakes occur at any time periods during the service life of the structures. The outcome of the research will help engineers improve their design under multiple earthquakes and multi-hazards, help inspectors identify damage extent and make comprehensive test plans, as well as help decision makers optimize rehabilitation strategies for RC structures in multi-hazard areas.

5.9 References

ABAQUS 6.12 Documentation. (2012). Dassault Systèmes Simulia Corp.

Alipour, A. (2010). "Life-cycle performance assessment of highway bridges under multi-hazard conditions and environmental stressors." *Ph.D. Dissertation*, Department of Civil and Environmental Engineering, University of California, Irvine.

Alipour, A., and Shafei, B. (2014). "Structural vulnerability measures for assessment of deteriorating bridges in seismic prone areas." *Maintenance and Safety of Aging Infrastructure*, edited by Dan Frangopol and Yiannis Tsompanakis, Chapter 3, CRC Press.

Alipour, A., Shafei, B., and Shinozuka, M. (2011). "Performance evaluation of deteriorating highway bridges located in high seismic areas." *Journal of Bridge Engineering*, 16(5), 597-611.

Alipour, A., Shafei, B., and Shinozuka, M. (2013). "Capacity loss evaluation of reinforced concrete bridges located in extreme chloride-laden environments." *Journal of Structure and Infrastructure Engineering*, 9(1), 8-27.

American Association of State Highway and Transportation Officials. (2011). AASHTO Guide Specifications for LRFD Seismic Bridge Design.

Andrade, C., Muñoz, A., and Torres-Acosta, A. (2010). "Relation between crack width and corrosion degree in corroding elements exposed to the natural atmosphere." *Proceedings, Fracture Mechanics of Concrete and concrete structures*, Seoul, Korea.

Apostolopoulos, C. A., Demis, S. and Papadakis, V. G. (2013). "Chloride-induced corrosion of steel reinforcement - Mechanical performance and pit depth analysis." *Journal of Construction and Building Materials*, 38, 139-146.

Berto, L., Simioni, P. and Saetta, A. (2008). "Numerical modeling of bond behavior in RC structures affected by reinforcement corrosion." *Journal of Engineering Structures*, 30(5), 1375-1385.

Cairns, J., Plizzari, G. A., Du, Y., Law, D. W., and Franzoni, C. (2005). "Mechanical properties of corrosion-damaged reinforcement." *ACI Material Journal*, 102(4), 256-264.

Cheung, M., Zhao, J., and Chan, Y. (2009). "Service Life Prediction of RC Bridge Structures Exposed to Chloride Environments." *Journal of Bridge Engineering*, 14(3), 164-178.

Coronelli, D. and Gambarova, P. (2004). "Structural assessment of corroded reinforced concrete beams: Modeling Guidelines." *Journal of Structural Engineering*, 130(8), 1214-1224.

Cui, Z., and Alipour, A. (2014). "A detailed finite-element approach for performance assessment of corroded reinforced concrete beams." *Proceedings, ASCE Structures Congress*, Boston, Massachusetts, 2002-2013.

Cui, Z., and Alipour, A. (2016). "Performance assessment of corroded highway bridge piers under cyclic loading." *Proceedings, Transportation Research Board (TRB) 95th Annual Meeting*, Washington, D.C.

DuraCrete (2000). "Probabilistic performance based durability design of concrete structures." The European Union-Brite EuRam III.

FEMA. HAZUS-MH MR4 Technical Manual, 2012, Washington, DC.

Guo, A., Li, H., Ba, X., Guan, X., and Li, H. (2015). "Experimental investigation on the cyclic performance of reinforced concrete piers with chloride-induced corrosion in marine environment." *Journal of Engineering Structures*, 105, 1-11.

Hu, N., Burgueño, R., Haider, S., and Sun, Y. (2016). "Framework for estimating bridge-deck chloride-induced degradation from local modeling to global asset assessment." *Journal of Bridge Engineering*, 21(9), 06016005-1-06016005-7.

Jamali, A., Angst, U., Adey, B., and Elsener, B. (2013). "Modeling of corrosion-induced concrete cover cracking: A critical analysis." *Journal of Construction and Building Materials*, 42, 225-237.

Kashani, M. M., Crewe, A. J., and Alexander, N. A. (2013). "Nonlinear stress–strain behaviour of corrosion-damaged reinforcing bars including inelastic buckling." *Journal of Engineering Structures*, 48, 417-429.

Ma, Y., Che, Y., and Gong, J. X. (2012). "Behavior of corrosion damaged circular reinforced concrete columns under cyclic loading." *Journal of Construction and Building Materials*, 29, 548-556.

Meda, A., Mostosi, S., Rinaldi, Z., and Riva, P. (2014). "Experimental evaluation of the corrosion influence on the cyclic behaviour of RC columns." *Journal of Engineering Structures*, 76, 112-123.

Molina, F.J., Alonso, C. and Andrade, C. (1993). "Cover cracking as a function of rebar corrosion: Part 2 - numerical model." *Journal of Materials and Structures*, 26, 532-548.

O'Connor, A., and Kenshel, O. (2013). "Experimental evaluation of the scale of fluctuation for spatial variability modeling of chloride-Induced reinforced concrete corrosion." *Journal of Bridge Engineering*, 18(1), 3-14.

Otieno, M., Beushausen, H., and Alexander, M. (2016a). "Chloride-induced corrosion of steel in cracked concrete – Part I: Experimental studies under accelerated and natural marine environments." *Journal of Cement and Concrete Research*, 79, 373-385.

Otieno, M., Beushausen, H., and Alexander, M. (2016b). "Chloride-induced corrosion of steel in cracked concrete—Part II: Corrosion rate prediction models." *Journal of Cement and Concrete Research*, 79, 386-394.

Ou, Y., Tsai, L., and Chen, H. (2012). "Cyclic performance of large-scale corroded reinforced concrete beams." *Journal of Earthquake Engineering and Structural Dynamics*, 41, 593-604.

Rodriguez, J., Ortega, L., and Casal, J. (1997). "Load carrying capacity of concrete structures with corroded reinforcement." *Journal of Construction and Building Materials*, 11(4), 239-248.

Shafei, B., and Alipour, A. (2015). "Application of large-scale non-Gaussian stochastic fields for the study of corrosion-induced structural deterioration." *Journal of Engineering Structures*, 88, 262-276.

Shafei, B., Alipour, A., and Shinozuka, M. (2012). "Prediction of corrosion initiation in reinforced concrete members subjected to environmental stressors: A finite-element framework." *Journal of Cement and Concrete Research*, 42(2), 365-376.

Val, D. and Chernin, L. (2009). "Serviceability reliability of reinforced concrete beams with corroded reinforcement." *Journal of Structural Engineering*, 135(8), 896-905.

Val, D., Chernin, L., and Stewart, M. (2009). "Experimental and Numerical Investigation of Corrosion-Induced Cover Cracking in Reinforced Concrete Structures." *Journal of Structural Engineering*, 135 (4), 376-385.

Vidal, T., Castel, A., and François, R. (2004). "Analyzing crack width to predict corrosion in reinforced concrete." *Journal of Cement and Concrete Research*, 34(1), 165-174.

Xia, J., and Jin, W. (2014). "Prediction of Corrosion-Induced Crack Width of Corroded Reinforced Concrete Structures." Proceedings, 4th International Conference on the Durability of Concrete Structures, West Lafayette, IN.

Yalciner, H., Sensoy, S., and Eren, O. (2015). "Seismic performance assessment of a corroded 50-year-old reinforce concrete building." *Journal of Structural Engineering*, 27(6), 683-696.

Zhang, R., Castel, A., and François, R. (2010). "Concrete cover cracking with reinforcement corrosion of RC beam during chloride-induced corrosion process." *Journal of Cement and Concrete Research*, 40(3), 415-425.

Table 5-1. Steel mass loss of bridge columns at 10 year time intervals (i_{corr}=5μA/cm^2)

t (year)	0	10	20	30	40	50	60	70
Steel mass loss	0	4.0%	7.8%	11.5%	15.0%	18.4%	21.7%	24.8%

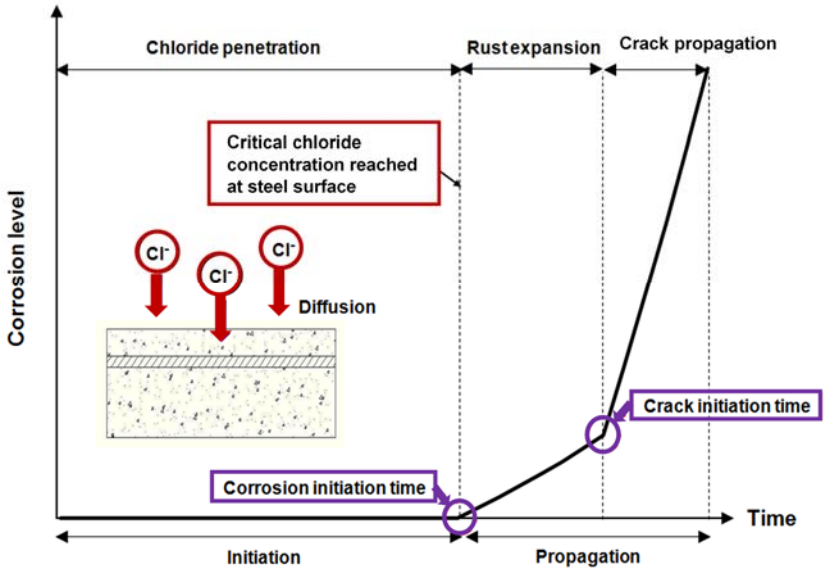

Figure 5-1. Chloride-induced corrosion process (Alipour et al 2013)

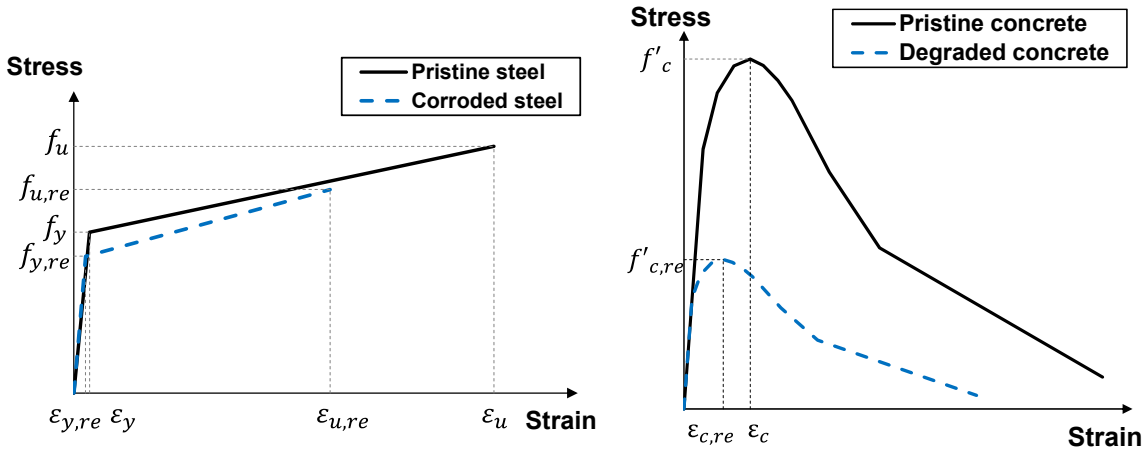

(a) (b)

Figure 5-2. Constitutive models of (a) steel and (b) concrete in pristine and corroded conditions

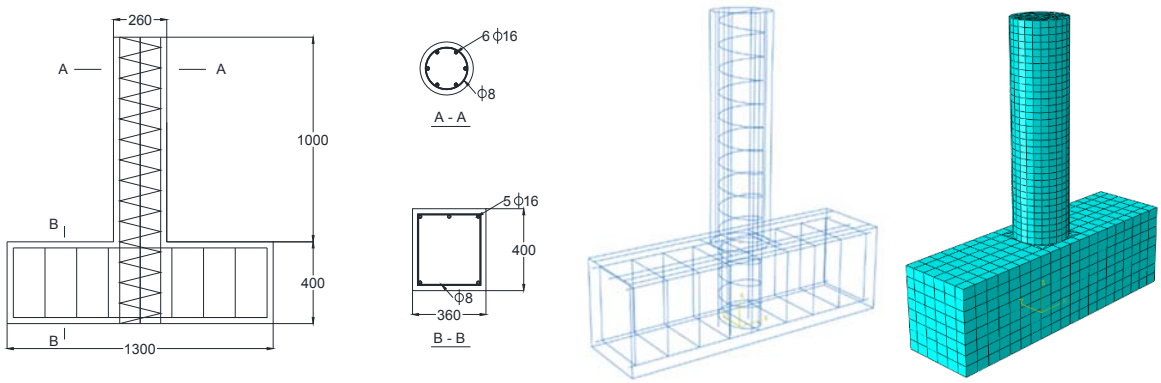

(a) (b)

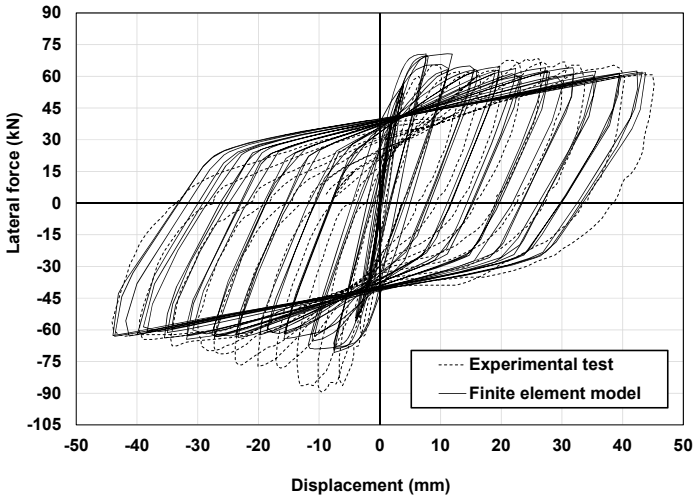

(c)

Figure 5-3. (a) Details of geometry (in mm); (b) FE models; (c) Comparison between the test and FE results

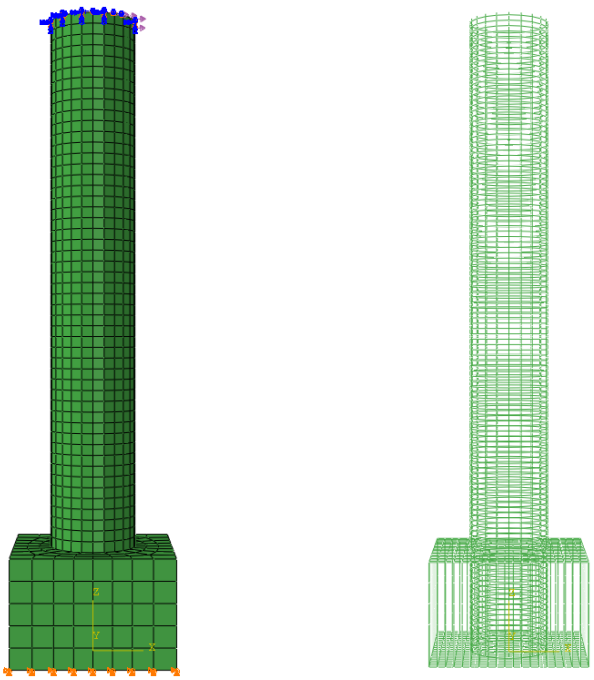

(a) (b)

Figure 5-4. FE model of (a) the real scale bridge column; and (b) its steel cage

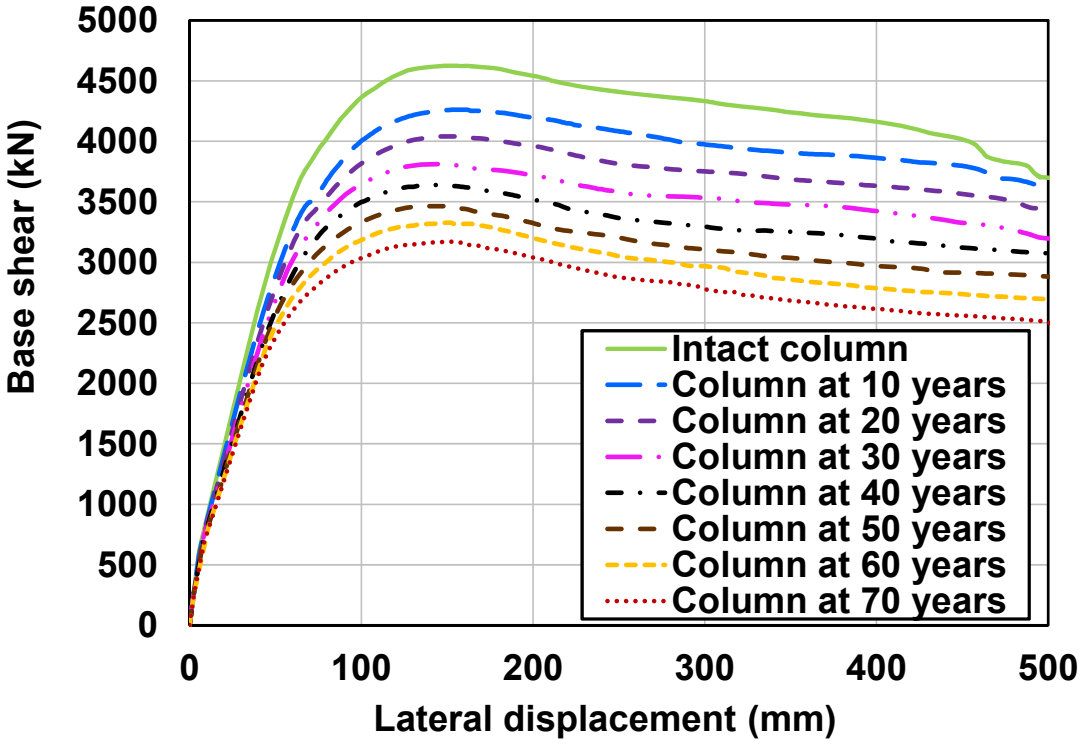

Figure 5-5. Results of pushover analysis for columns from 0 to 70 years

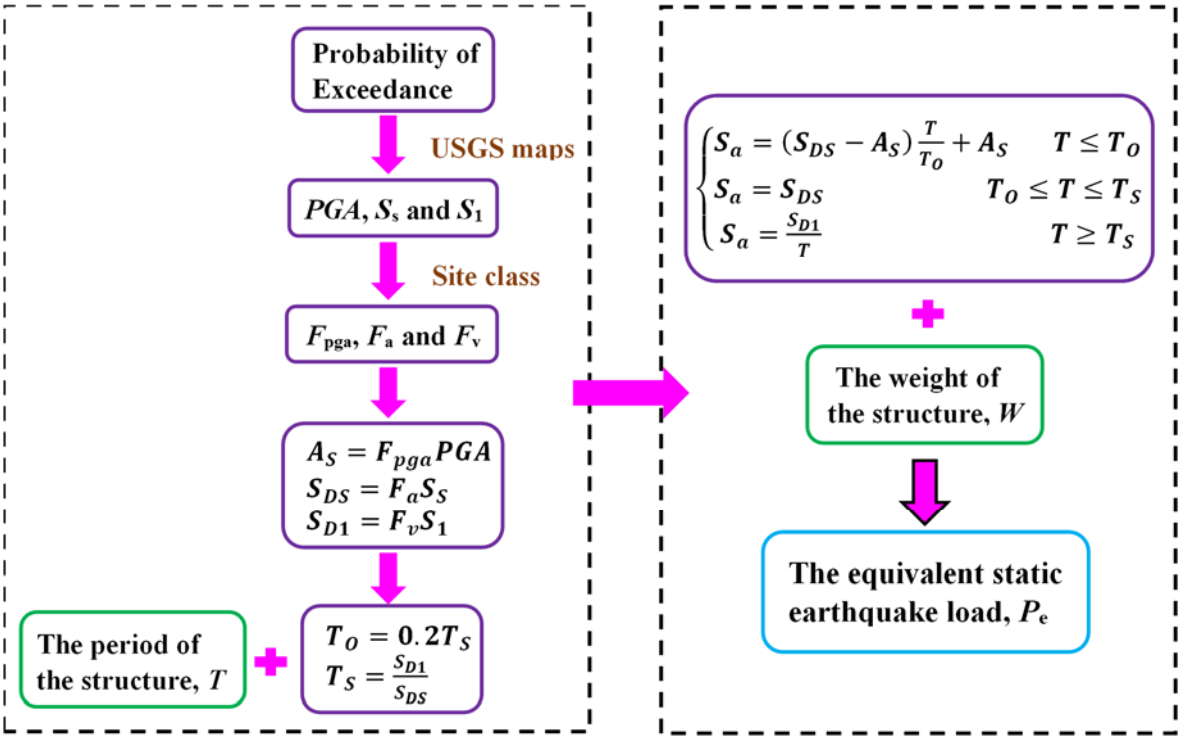

Figure 5-6. Calculation procedure of equivalent static load

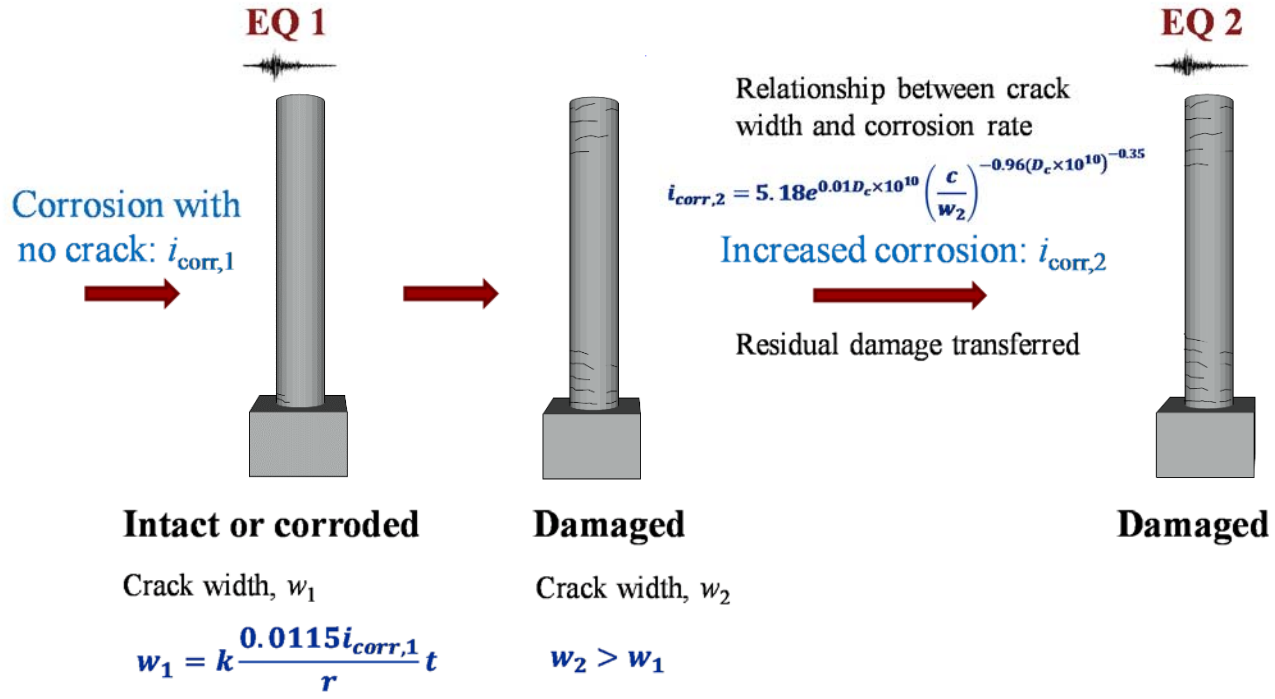

Figure 5-7. Case scenarios considered in this study

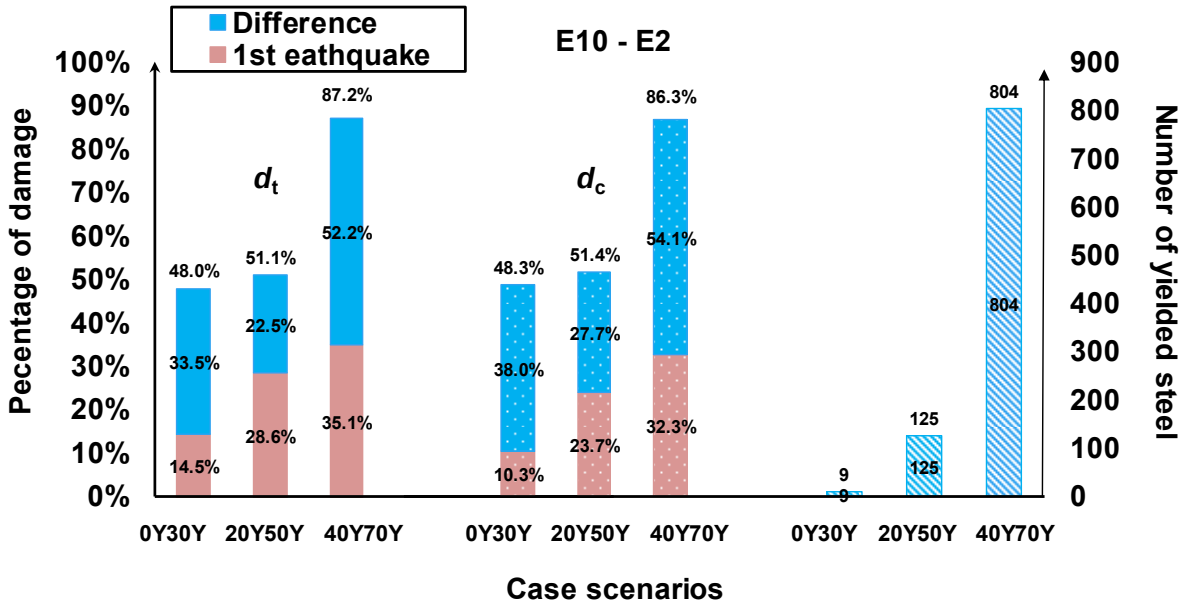

(a)

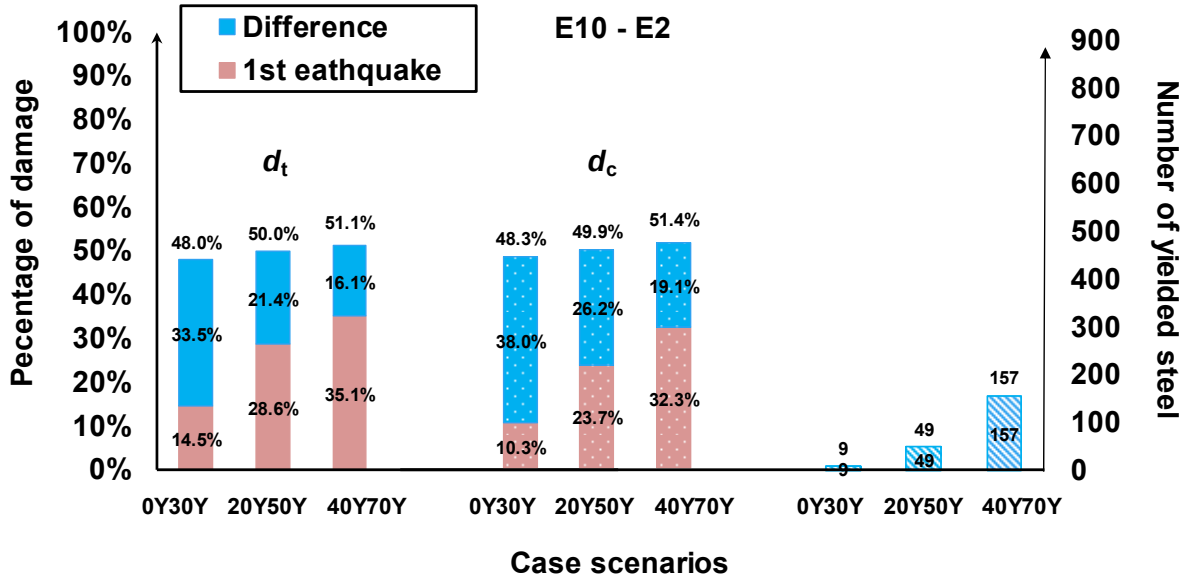

(b)

Figure 5-8. Damage extent of the column under the case scenarios: (a) Variant corrosion rate; (b) Constant corrosion rate

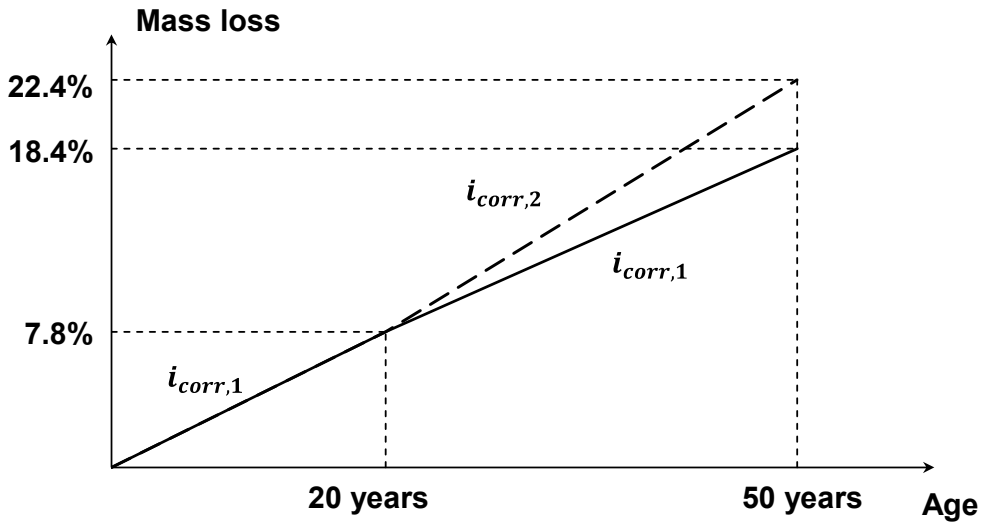

(a)

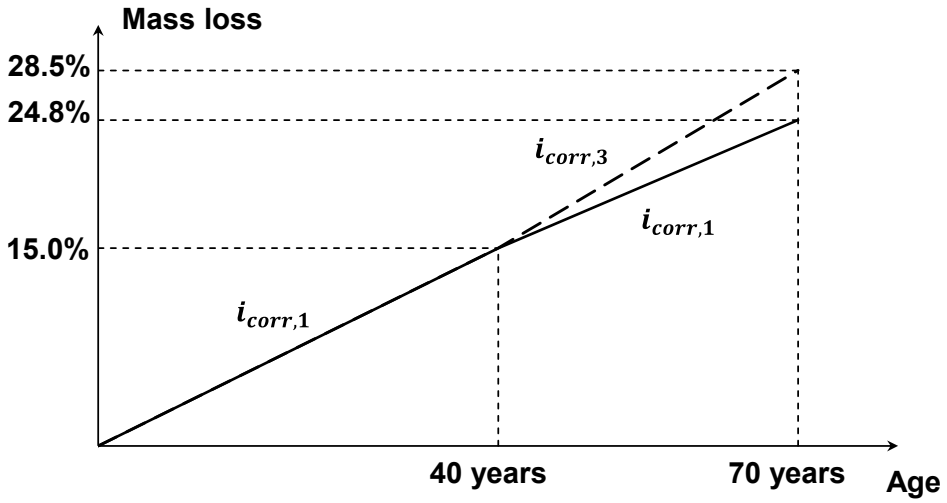

(b)

Figure 5-9. Comparison of steel mass loss percentage for constant and variant corrosion rates: (a) The case 20Y50Y; (b) The case 40Y70Y

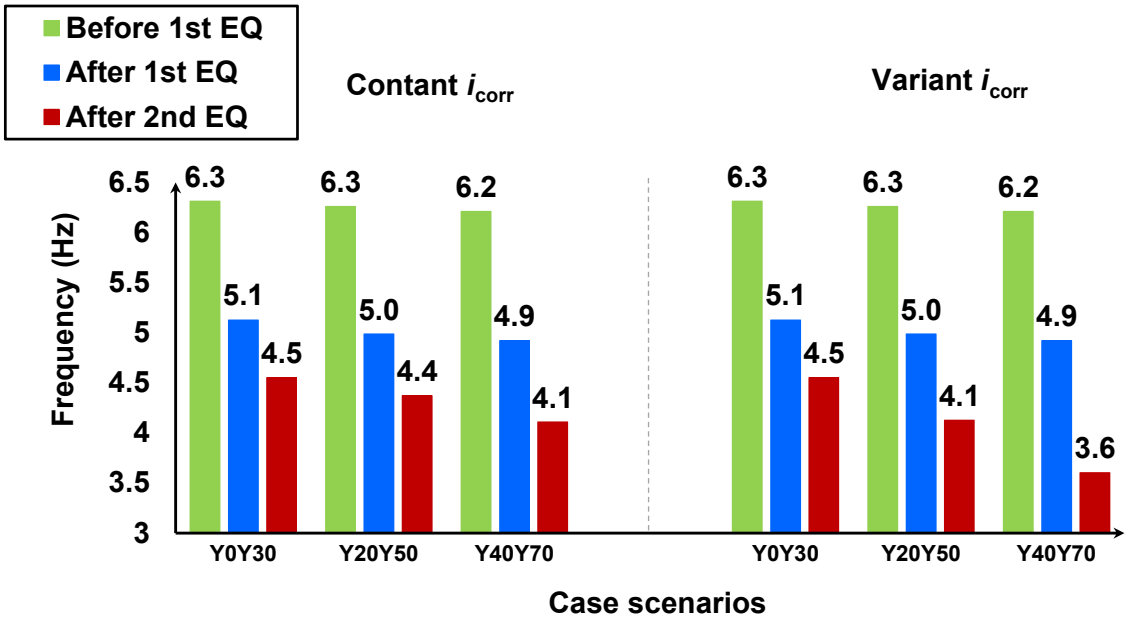

Figure 5-10. Frequencies of the column before and after the first and second earthquakes

CHAPTER 6. CONCLUSIONS AND CONTRIBUTIONS

This study has focused on the chloride-induced concrete crack initiation and propagation in reinforced concrete structures, as well as the lifetime performance of RC structures under the environmental stressors (i.e., corrosion) and natural hazard (earthquakes).

Important analytical models for corrosion-induced crack initiation of concrete cover under both uniform and pitting corrosion have been critically reviewed. For the purpose of comparing predictive models, the crack initiation time is calculated using three selected analytical models for five experimental tests. The predicted crack initiation time is then compared with their corresponding experimental observed time to crack initiation, resulting in a conclusion that predictive models are developed based on the results from a particular experimental test and normally provide more reasonable results for the situation that is similar to the test conditions. The value of the predicted time is highly dependent on the value of the input parameters, such as types of corrosion products and the thickness of ITZ. 3D FE models have been proposed and validated to study the effect of different parameters on crack initiation time. It can be concluded that the composition of corrosion products and corrosion mechanism (uniform or pitting corrosion) can significantly affect the crack initiation time. The crack initiation time varies dramatically with the thickness of ITZ, and the corrosion rate. Other factors which can also influence the crack initiation time are the geometrical parameters: concrete cover depth, rebar diameter and spacing, as well as material properties of concrete. An effective approach to increase the crack initiation time is to increase the depth of concrete cover. In order to study the effect of different parameters on the crack propagation pattern throughout concrete cover, a sensitivity analysis is conducted using the FE analysis. The crack

propagation patterns for different cover depths in different time periods, as well as the crack patterns for different cover depth to bar diameter ratios have been analyzed.

The adverse effects of corrosion in reinforcement on structural behavior of RC beams includes reduction of steel cross sectional area, change of steel and concrete properties, as well as deterioration of bond. All the corrosion effects have been studied with a particular attention drawn to bond loss. The bond strength increases initially with the increase of corrosion under low level of corrosion and decrease consistently with further increase of corrosion. Models for residual bond strength in corroded RC beams have been presented and compared. In order to obtain the structural behavior of corroded RC beams, nonlinear FE models which are able to take into account all the corrosion effects are developed and verified with the available experiment data. The FE models adopted damaged plasticity model for concrete elements and utilize nonlinear spring elements to simulate the bond behavior between steel and concrete. The results from the FE analysis clearly show that corrosion influences the strength and ductility of a structure at ultimate condition. For instance, the load carrying capacity of Type 11 beams was reduced by 21.4% - 35.3%, depending on the corrosion levels. The corrosion may also cause excessive cracking and deflection, which lead to serviceability failure. The FE models provide a good prediction of the damage process of reinforced concrete structures subjected to corrosion.

The lifetime performance of RC columns under both earthquake and chloride-induced corrosion has also been studied. All the degrading effect of corrosion have been implemented into the developed 3D FE models and updated according to different ages of the column. The capacity and stiffness of the column at different ages are evaluated and found to be significantly reduced by the age of the column, i.e., the level of corrosion. Nonlinear time history analysis

has been performed for the column at three different ages: 0, 20 and 50 years. The seismic performance of the pristine and corroded columns under three different hazard levels has been investigated. The type, region and extent of damage in the column at different corrosion levels have been identified. Crack propagation patterns in the concrete cover can be visualized. The amount of both concrete and steel damage is quantified. It is noted that under the severe earthquake, extensive corrosion may result in a brittle failure of the column without the development of concrete cracks. The frequency of the column drops significantly after the earthquakes and decreases with the increase of corrosion levels. Damage states have been defined in terms of the maximum normalized steel strain providing more structural details at each state. The seismic performance of the columns that experience a higher corrosion risk on one or both sides of the critical bottom region has also been investigated. It can be concluded that a much higher corrosion risk at the critical lower section of the column can dramatically compromise the seismic performance of the column, leading to complete failure under severe earthquakes. The longitudinal reinforcement at the bottom of these columns is very likely to rupture together with very high strains in the spirals and large areas of concrete spalling at the bottom regions. Such columns tend to fail due to lack of confinement at the critical location caused by corrosion-induced reinforcement degradation. These columns could perform much worse than a column undergoing a consistent corrosion rate at a much older age and must be drawn special attention to in order to prevent failure during seismic events. Thus, the damage states in the current study categorize them into Complete damage state, so that designers, inspectors or maintenance teams can be altered to the vulnerability of such columns to earthquake events and certain protections or special designs could be done to prevent catastrophic failures during seismic events. The findings of the study highlight the necessity of

studying the combined effects of earthquake and corrosion in seismic prone areas. The proposed framework is capable of predicting the seismic performance of RC columns with different corrosion levels at any age during their lifecycles and providing the details of damage extent, type and region, therefore, will provide a power tool to help improving design and optimizing rehabilitation strategies for RC structures.

Multiple seismic events occurring during the lifetime of the RC structures has also been considered in this study. A series of full-scale bridge columns from 0 to 70 years have been simulated through finite element modeling. The capacities of the columns have been evaluated through nonlinear pushover analysis and found to be greatly influenced by the age of the column, i.e. the level of corrosion. The strength and stiffness drop significantly as corrosion level increases. Equivalent static analysis has been conducted to analyze the structural behavior of the columns under two earthquakes occurring at different time periods in their lifetime. The developed framework has been successfully transferred the residual damage from the first earthquake to the second earthquake and simultaneously implementing the time-dependent structural degradation due to chloride-induced corrosion. The type and extent of damage from each earthquake as well as the total damage after the two earthquakes have been obtained. The developed framework can provide a reliable prediction for the performance of corroded RC structures under multiple seismic events, therefore, will help engineers improve their designs, identify necessary test regions and define comprehensive test plans, as well as optimize rehabilitation strategies for RC structures in multi-threat areas.